3-2021

Computational Electromagnetic Modeling of Metasurface Optical Devices with Defect Study

Carlos D. Diaz

COMPUTATIONAL ELECTROMAGNETIC MODELING OF METASURFACE OPTICAL DEVICES WITH DEFECT STUDY

DISSERTATION

Carlos D. Diaz, Captain, USAF

AFIT-ENP-DS-21-M-112

DEPARTMENT OF THE AIR FORCE
AIR UNIVERSITY

AIR FORCE INSTITUTE OF TECHNOLOGY

Wright-Patterson Air Force Base, Ohio

AFIT-ENP-DS-21-M-112

COMPUTATIONAL ELECTROMAGNETIC MODELING OF METASURFACE OPTICAL DEVICES WITH DEFECT STUDY

DISSERTATION

Presented to the Faculty

Department of Engineering Physics

Graduate School of Engineering and Management

Air Force Institute of Technology

Air University

Air Education and Training Command

In Partial Fulfillment of the Requirements for the

Degree of Doctorate of Philosophy in Applied Physics

Carlos D. Diaz, BS, MS

Captain, USAF

December 2020

DISTRIBUTION STATEMENT A.
APPROVED FOR PUBLIC RELEASE; DISTRIBUTION UNLIMITED.

AFIT-ENP-DS-21-M-112

COMPUTATIONAL ELECTROMAGNETIC MODELING OF METASURFACE OPTICAL DEVICES WITH DEFECT STUDY

Carlos D. Diaz, BS, MS

Captain, USAF

Committee Membership:

Dr. Michael A. Marciniak
Dissertation Advisor

Dr. Anthony L. Franz
Committee Member

Dr. Peter J. Collins
Committee Member

Dr. Augustine M. Urbas
Committee Member

ADEDEJI B. BADIRU, PhD
Dean, Graduate School of Engineering and Management

Abstract

Metasurface optical devices aim to replicate the performance of refractive optical devices but with much less material. A subset of these, plasmonic metasurfaces, employs charge oscillations on the surface of nanoantennas to achieve this desired effect, but the first fabricated of these devices were plagued by a fundamental limit on transmission (<25%). To improve upon this limitation of in-plane plasmonic metasurface devices, two distinct sets of Out-of-Plane (OOP, i.e. 3D-thin-film) metasurface plasmonic phase elements were designed for improved transmission (~60%) using genetic algorithm techniques to work in the infrared (IR). These were fabricated as beamsteerers using Membrane Projection Lithography (MPL) and characterized using a Complete Angle Scatter Instrument (CASI). The Bidirectional Transmittance Distribution Function (BTDF) of the beamsteerers was measured as a function of scatter angle for four different polarization configurations: co-polarization and cross-polarization for two orthogonal linear polarization states. Experimental data from the two beamsteerers was analyzed via computational simulations using a finite element method (FEM) solver to generate the near fields of each phase element of the device and a Stratton-Chu formulation to propagate these to the far field. The measurements showed the designed beamsteering from the devices, but also a strong zero-order diffraction not present in the simulations. This disagreement between models and measurements motivated this study to understand what was causing these differences. To that end, defect and adjusted FEM models of the beamsteerers were developed to examine methods that would account for fabricated device performance. The defect

models which addressed the specific defects observed in scanning electron microscope (SEM) images of the fabricated devices predicted their performance, while adjusted models that affected the coupling between adjacent phase elements of the device produced results that also well-predicted the measured data. These models then provided an understanding of the near-field effects that caused this behavior, such as phase-element-to-phase-element coupling. Evidence is strong that the amplitude and phase imparted by the fabricated phase elements must be significantly different than what was designed, either because their placement among other phase elements is different than what was designed or their design, itself, was slightly changed during fabrication. Future work will focus on further studying the impact of coupling on the performance of these devices and leveraging the lessons learned into future OOP design-fabrication-test iterations.

Acknowledgments

First and foremost, I would like to express my sincere gratitude to my advisor, Dr. Michael Marciniak. His countless hours spent reading drafts that were riddled with errors helped me learn a lot more about the craft of writing and communication. That coupled with his constant insights and suggestions has turned this document into something that I am proud of. I know it was not easy but I will forever be grateful for all of his help.

I would also like to thank Dr. Augustine Urbas, whose direction at a crucial moment in my PhD candidacy led to this project. It was his suggestion of studying defects that helped me find a new topic when my first prospectus was found to be wanting. That coupled with great insight and his willingness to help will always be appreciated.

I would also like to thank both Dr. Anthony Franz and Dr. Peter Collins. Dr. Franz was my MS Thesis advisor, and without his initial guidance I do not know where I would be, and Dr. Collins taught me the course on computational electromagnetics which would form the foundation for this project. I am grateful to my committee for all of their help.

Outside of my committee I would like to extend my thanks to my family. First to my loving wife, who helped me throughout this challenging period in my life, all while taking care of our beautiful daughter. To my mother who at a moment's notice would travel here if I ever needed an extra hand in my home. And to my aunt, who was also willing to come help at a moment's notice. She took care of me, my wife, and our daughter as if we were her own kids. I will forever be in her debt. And last but not least to my loyal companion and friend, my dog Kenzie.

There are countless others whom I have not mentioned for which I am grateful to. I would not be here without their help and I hope one day I am able to show my gratitude.

Carlos Diaz

Table of Contents

List of Figures

Page

List of Tables

Page

COMPUTATIONAL ELECTROMAGNETIC MODELING OF METASURFACE OPTICAL DEVICES WITH DEFECT STUDY

I. Introduction

1.1 Motivation for research

A natural evolution in the progression of technological instruments is to maintain or improve on their capabilities while minimizing the amount of space that said instruments occupy. This progression is apparent in many facets of technology, for example computing, where the first computer weighed around 18 tons and occupied a footprint of about 170 meters squared [1], compared to today's computers which occupy an area of a few millimeters squared [2]. One multifaceted area of research which tackles this issue of minimizing space while maintaining performance is optical metamaterials.

Metamaterials can be described as man-made structures that exhibit macroscopic parameters that are different than those of their constituent components and of other materials that are found in nature [3]. Although the notion of structured materials is one that has been around for about a century, the pursuit of 3D metamaterials accelerated around 20 years ago [4]. Optical metamaterials achieve unique properties by using building blocks that are on the scale size of microns or nanometers, in any case, less than the wavelength of light with which they interact. In 2008, a 3D optical negative index material was experimentally demonstrated by measuring the angle of refraction from a prism made of "fishnet" metamaterial, where the experimental results and numerical calculations gave

direct evidence of zero and negative phase index in the metamaterial [5]. This "fishnet" was fabricated as 21 alternating metal-dielectric films which were then focused ion-beam milled. At optical frequencies, however, losses in the metallic elements were a problem. Any promising potential applications would be hindered by those high losses and strong dispersion associated with these metallic films. A further challenge in metamaterials, in general, was the difficulty in the micro- and nano-fabrication of the 3D structure.

Therefore, attention for optical devices turned to metasurfaces, which are essentially the 2D equivalent of bulk 3D metamaterials, but virtually eliminate the dependence on any extended propagation effects [6]. In the field of optics, metasurfaces have found a multitude of applications, from flat metalenses [7-11], polarimeters [12 – 14], axicons [15, 16], polarization elements [17 – 21], holograms [22 – 24], optical image encoders [25, 26], tunable optical components [27 – 30], a retroreflector [31], and a light field camera with a micro lens array composed of achromatic metalenses [32]. Suffice to say, metasurfaces are a very active area of research and many different research groups are expending considerable effort in their study.

In the field of optics, the issue of minimization applied to a lens is hindered by a fundamental limit on how much material the lens needs in order to achieve control over light. In a conventional refractive lens, light is controlled by the gradual phase accumulation as the wave travels through the refractive material [33, 34]. This accumulation occurs over a path that is many times the wavelength long and this enforces a lower limit on the thickness of the lens. Flat metasurface lenses break this dependence on the gradual phase accumulation by introducing abrupt changes in the phase of light as it travels through the planar surface [6, 35-39].

One of the first designed infrared (IR) metasurfaces, the V-antenna metalenses [6, 39, 40], relied on plasmonic structures situated in a plane perpendicular to the direction of propagation in order to achieve control over the incoming light. This orientation with respect to the incoming EM wave is referred to as in-plane. It was found that these in-plane plasmonic structures had a maximum transmission efficiency of 25% [41]. With this in mind research at the Air Force Institute of Technology (AFIT) was conducted in the infrared (IR) by Maj Bryan Adomanis, PhD [42, 43], to design a plasmonic metasurface structure that placed the plasmonic structures in an out-of-plane (OOP) configuration in order to achieve a transmission higher than that of the in-plane structures. Using a genetic algorithm (GA), his work culminated in eight phase elements that covered the 0-to-2π phase range required for metalenses, with a mean transmission of $\langle T \rangle = 0.658$. These structures were subsequently fabricated at Sandia National Laboratory (SNL) using Membrane Projection Lithography (MPL) [44 – 47].

The Bidirectional Transmission Distribution Function (BTDF) of the fabricated device was then measured at AFIT using a Schmidt Measuring System (SMS) Complete Angle Scatter Instrument (CASI) [48 – 50]. Although the fabricated device did steer the beam as designed, it suffered from a large zero diffraction order peak that was not present in simulations, which represented a large discrepancy between measured and modeled performance. In his dissertation, Adomanis discussed several issues that might have led to the poor performance of the device, such as limitations of the design software, misalignments during measurement of the sample, Fabry-Perot resonances that might not have been accounted for, or issues with the design and fabrication of these lenses.

In order to attempt to improve over Adomanis' design, a team at Pennsylvania State University (PSU) designed new phase elements using a GA procedure similar to that which Adomanis had previously used. These new structures were fabricated using the same fabrication MPL technique, but the orientation of the successive elements was changed with respect to the incoming polarization. A discussion of the two placements will be expounded on in Chapter 2. This device was again measured using the CASI at AFIT to characterize it in terms of the BTDF; and this device, just like the one designed by Adomanis, steered the beam as designed, but also suffered from the larger-than-expected zero-order diffraction, which again disagreed with predictive simulations. After this second disagreement between measurement and model, the research conducted in this dissertation was initiated in an attempt to understand what is affecting the performance of these devices.

1.2 Significance for the USAF and DoD

This topic is of great interest to the needs of the Air Force. The Air Force Office of Scientific Research (AFOSR) stated in their "Fiscal Year (FY) 2021 Department of Defense Multidisciplinary Research Program of the University Research Initiative" [51] that the field of metasurface optics is a clear interest. The stated objective in this document reads,

> "The goal of this multi-university research initiative (MURI) is to combine recent advances of metasurfaces and optical nanoantennas with sensing, processing and information science to probe fundamental detection limits and reveal new information processing concepts… These metasurfaces should ultimately be able to achieve a variety of optical functions, including optical image and signal processing, filtering, sensing and photodetection functions across the spectrum (VIS, Near-IR/Mid-IR), extendable to more complex operations on the detected images. The research should address fundamental

questions and challenges related to the ability of achieving such complex functions in an extremely compact/flat form factor."

Furthermore, two of the stated research concentration areas are directly related to this research,

"… novel photodetection and hyperspectral imaging strategies across the spectrum (VIS, Near-IR/Mid-IR); … new computational and inverse design strategies for metasurfaces capable of performing novel detection and complex imaging functions;"

Specifically, the background of the topic, "Metasurface Edge Sensing, Processing and Computing" states,

"Advanced optical sensors and imaging systems that sense and process complex information encoded in the incident optical wavefront are essential tools used in the increasingly demanding missions of the DOD. Unfortunately, current technologies do not meet the size, weight, and energy efficiency requirements needed for new wearables and aerospace applications… New knowledge is also required, as the fundamental physics of photodetection in hybrid nanophotonic structures and analog computing metasurfaces are still poorly understood and many breakthroughs are expected."

This document also states that this project will be funded for five years, with an average of $1.5 M expenditure allotted per year. The metaoptic devices being investigated in this dissertation are designed to function in the IR, and this research effort was invested in computational strategies meant for better analyzing and designing new optical metasurfaces.

In a separate Broad Agency Announcement (BAA), also from AFOSR [52], one of the five areas of research interest under their "Optoelectronics and Photonics" research program is "Nanophotonics (including Plasmonics, Photonic Crystals, Metamaterials, Metaphotonics and Novel Sensing)". This basic research objective states,

"…The program is interested in the design, growth and fabrication of nanostructures that can serve as building blocks for nano-optical systems… Specific areas

of current interest include nanophotonics, use of nanotechnology in photonics, exploring light at the nanoscale, nonlinear nanophotonics, plasmonics…"

From these documents, it is clear to see that there is a stated interest and need from the USAF and DoD in pursuing research focused on metasurface optical devices. This dissertation addresses specific needs outlined in these documents. It looks to expand upon our knowledge of plasmonic metasurfaces to better understand how they behave, what affects their performance, and tries to find better ways of modeling and designing them.

Further, the partnership touched on in the previous section between PSU, SNL and AFIT is unique to the metasurface community due to the relationship between the design (PSU), fabrication (SNL), and characterization/analysis (AFIT) that is undertaken on these devices. AFIT provides unique characterization techniques that are not commonly used to study these devices, such as scatterometry, and also studies optical devices that are not normally fabricated, such as beamsteerers. This partnership presents us with a unique perspective that allows us both to be active contributors to this community and to learn of new developments.

1.3 Specific Research Issues

Section 1.1 identified the key problem of the two fabricated metasurface beamsteerers. Both devices steered the beam as designed, but both were plagued by a large 0-order diffraction peak that was not accounted for in simulations and that was larger than the designed diffraction peaks. This research focused mainly on Finite Element Method (FEM) [53 – 54] simulations as the main tool with which the metasurface elements were

studied in order to better understand the issues that could cause the discrepancies between modeling and measurement results.

Using FEM models as the tool to probe the inner workings of these fabricated devices, the questions addressed were:

- What modeling methods are useful in predicting the behavior of the fabricated devices and which are not?
- What insights do the useful modeling methods provide about the effects that degrade the fabricated devices performance?
- How can defects which have been identified in the fabricated device with a Scanning Electron Microscope (SEM) be modeled in an attempt to explain the behavior of the fabricated devices?
- Is there anything learned from the FEM modeling and the modeled defects that can lead to a new design space that would improve the performance of future fabricated devices?

1.4 Organization

The purpose of this document is to educate the reader about the topic at hand, introduce the issue that prompted the research, explain how the research was carried out, discuss the various results obtained, and detail what was learned about the devices studied. To that end the layout of this document is as follows.

Chapter II, Theory and Background, will provide the reader the relevant background that is necessary to understand the issues that are addressed by this research.

In that chapter the following topics are discussed: the generalized theory of refraction, flat metalens designs, plasmonic metalenses, the different configurations for the fabricated beamsteerers, and a description of the fabrication methodology, MPL. The GA, which was the method used to design the individual phase elements, will not be discussed, as I myself did not use it.

Chapter III, Research Methodology, will discuss the different techniques used to obtain the data presented in this document. There are two sources of data, experiment and modeling. The experimental data was obtained using the CASI, and its setup and operation will be discussed. The modeling data was obtained via a variety of methods which will be discussed, including the FEM software used, COMSOL® [55].

Chapter IV, Measurements, Ideal Models and Defect Study of the Blazed-Grating Device, will present comparisons between ideal models and the measured data for the blazed grating beamsteering device. It will present early efforts made to reconcile differences between measurement and modeling, and explain the issue this research tried to answer. It also presents research which addresses the question of how the defects observed in the fabricated device affect its performance. It presents defect models and how the results of those compare to the measured data.

Chapter V, Adjusted Models, moves away from modeling specific defects and attempts to replicate the behavior of the fabricated device via modeling techniques that do not alter the original phase elements but affect their coupling again for the blazed-grating device. The models that were attempted here were able to reconcile the measurement with the modeling results. The details of the coupling are discussed.

Chapter VI, Phased Array Device Beamsteerer, discusses the measurements, ideal model, and adjusted models that were accomplished for the phased-array beamsteering device. Here some of the previous techniques developed for the blazed-grating device were applied as a means of studying a different device in an effort to determine which ones were applicable and which ones were not.

Chapter VII concludes this document by presenting a summary of the work done, the research questions answered, and describing future work that extends naturally from this research.

II. Background and Theory

2.1 Introduction

This chapter is intended to provide enough background for the reader to understand the results that were obtained from the research. To that end there are discussions on the theory of generalized refraction and reflection, a generalized overview of metasurface optical devices, a discussion of plasmonic metasurface devices, an overview of the specific metasurface devices fabricated for this experiment, and finally an overview of the methodology employed to create the metasurface devices, which includes a discussion on some of the fabrication errors found in these devices.

2.2 Generalized Theory of Refraction and Reflection

A common refractive optic controls light by introducing a gradual phase shift that accumulates as light propagates along the optical path. The fact that this phase accumulation is gradual means that it requires a medium of thickness many times the length of the wavelength in order to have effective control over the light. A metasurface optic is different in the sense that it introduces an abrupt phase shift over a scale on the order of a wavelength along the optical path, as the light travels through the plane where the metasurface is located, and it does so with structures that are smaller than the size of the wavelength. In order to make sense of how a surface of thickness smaller than a wavelength imparts an abrupt phase shift, an extension to Snell's law is necessary, which is termed the

"generalized law of refraction and reflection" [6]. The generalized law explains how a material with an engineered abrupt phase shift behaves similarly to the gradual phase accumulation in a thick medium of one refractive index surrounded by another medium with a different refractive index.

To understand the generalized law of refraction, one needs to revisit Snell's law and apply Fermat's principle [6]. Considering an incident plane wave at an angle θ_i and looking at two incident light beams both which are infinitesimally close to the actual path, as in Figure 1, it can be seen that the phase difference between the two is zero,

$$[k_0 n_i \sin(\theta_i)\, dx + (\Phi + d\Phi)] - [k_0 n_t \sin(\theta_t)\, dx + \Phi] = 0, \quad (1)$$

where θ_t is the angle of refraction, Φ and $\Phi + d\Phi$ are the phase discontinuities at the locations where the two paths cross the interface, dx is the distance between the crossing points, n_i and n_t are the refractive indices of the two media, and $k_0 = 2\pi/\lambda_0$, where λ_0 is the vacuum wavelength. If the phase gradient along the interface is designed to be constant, the previous equation leads to the generalized Snell's law of refraction,

$$n_t \sin(\theta_t) - n_i \sin(\theta_i) = \frac{\lambda_0}{2\pi}\frac{d\Phi}{dx}. \quad (2)$$

Equation 2 implies that the refracted beam can have an arbitrary direction, provided that a suitable constant gradient of phase discontinuity along the interface (dΦ/dx) is introduced. It is noted that this does not only affect refraction, but reflection as well and that expression is given by,

$$\sin(\theta_r) - \sin(\theta_i) = \frac{\lambda_0}{2\pi n_i}\frac{d\Phi}{dx}, \tag{3}$$

which is commonly termed the generalized law of reflection.

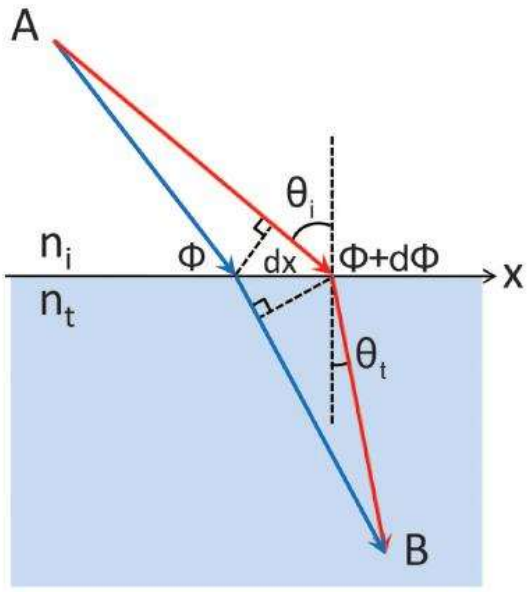

Figure 1. Schematic used to derive the generalized Snell's law of refraction. The interface between the two media is artificially structured in order to introduce an abrupt phase shift in the light path, which is a function of the position along the interface. Φ and Φ + dΦ are the two phase shifts where the two paths (blue and red) cross the boundary. Image taken from source with permission [6].

When looking at Figure 1, it is noted that only two dimensions are included, which are the vertical and the horizontal, but this phase shift can be dependent on the polarization and both the azimuthal and polar angles the light makes with respect to the plane of incidence as is shown in Figure 2. This leads to the generalized laws of refraction and reflection which take into account the azimuthal incidence angle φ,

$$n_t \sin(\theta_t) - n_i \sin(\theta_i) = \frac{\lambda_0}{2\pi}\frac{d\Phi}{dx}, \tag{4}$$

$$\cos(\theta_t)\sin(\varphi_t) = \frac{\lambda_0}{n_t 2\pi}\frac{d\Phi}{dy}, \tag{5}$$

$$\sin(\theta_r) - \sin(\theta_i) = \frac{\lambda_0}{n_i 2\pi}\frac{d\Phi}{dx}, \tag{6}$$

$$\cos(\theta_r)\sin(\varphi_r) = \frac{\lambda_0}{n_i 2\pi}\frac{d\Phi}{dy}, \tag{7}$$

where Equations (4) and (5) comprise the generalized laws of refraction, and Equations (6) and (7) comprise the generalized law of reflection [39].

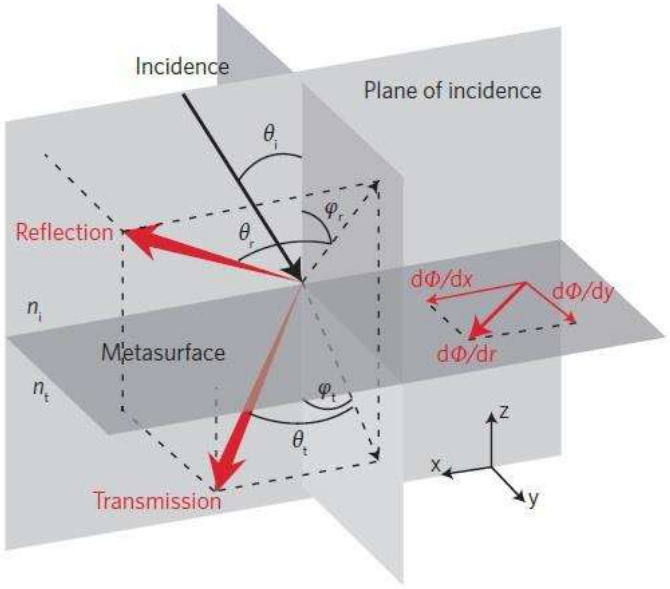

Figure 2. A gradient of interfacial phase jump dΦ/dr provides an effective wavevector along the interface that can bend transmitted and reflected light into arbitrary directions. In particular, the component dΦ/dy normal to the plane of incidence leads to out of plane refraction and reflection. Image taken from source with permission [39].

The generalized laws indicate that the transmitted and reflected light beams can be bent into arbitrary directions in their respective half space, depending on the direction and

magnitude of the interfacial phase gradient, as well as the refractive indices of the surrounding optical media.

2.3 Metasurface Optical Design

The previous section introduced the concept of the generalized laws of reflection and refraction, and with it introduced the notion of abrupt phase changes. Metasurface optics are designed with these abrupt phase changes to replicate the control over light that a refractive lens has without the burden of material that is many times thicker than a wavelength. But the designed abrupt phase shift is only one of many things that are needed when designing a metasurface that achieves the same optical function of a refractive lens. In order for the lensing condition to hold, and for the wave that travels through the metalens to focus at a distance f, the subwavelength structures or "phase elements" that compose the metalens need to meet the phase matching condition,

$$\Delta\Psi = \Psi_{i+1} - \Psi_i = \frac{2\pi}{N}, \tag{8}$$

where Ψ_i is the Fresnel lens phase formula,

$$\Psi_i(x,y) = \frac{2\pi}{\lambda_0}\left(\sqrt{x_i^2 + y_i^2 + f^2} - f\right) + \Psi_0, \tag{9}$$

here N is the number of these structures or "scatterers", i is the scatterer index of the range $\{1, N-1\}$, λ_0 is again the freespace wavelength, and Ψ_0 is the phase of the central scatterer [56]. For equally spaced elements of a constant phase gradient, this condition cannot be met and either the phase shift or the element spacing must be non-linear.

The first published IR metalenses made use of non-linear element spacing, and those elements were the plasmonic V-antenna [40]. Here discrete regions of constant phase were spaced non-uniformly to meet the phase matching condition. The V-antenna metalens achieved the abrupt phase shift by using plasmonic structures, in this case specifically oriented gold nanoantennas. The next section will delve into a more detailed description of these plasmonic scatterers.

2.4 Plasmonic Metasurfaces

Considering a plasmonic surface, when a beam of light impinges on a metallic optical antenna, the optical energy is coupled into surface electromagnetic waves propagating back and forth along its surface. These are accompanied by charge oscillations inside the antenna [39]. These coupled surface wave and charge oscillations are known as surface plasmons, hence the term "plasmonic". Abrupt phase changes over the scale of the free space wavelength in the direction of the incident light are the result of the strong interaction between light and the localized surface plasmons.

To the extent that the metallic nanostructure and the corresponding plasmons can be described by a single harmonic oscillator, the scattering phase shift cannot exceed π [57]. To explain why this is, a plasmon can be described using a simple model in which it

is represented by a charge q located in time and space at $x(t)$, with mass m on a spring, with spring constant k, driven by a harmonic incident field E_0, with frequency ω. This model accurately describes the near- and far-field spectral features of plasmonic resonance, including the phase response. Because of the ohmic losses, the charge experiences internal damping with damping coefficient γ,

$$\frac{d^2x}{dt^2} + \frac{\gamma}{m}\frac{dx}{dt} + \frac{k}{m}x = \frac{q}{m}E_0 e^{i\omega t} + \frac{q^2}{6\pi\varepsilon_0 mc^3}\frac{d^3x}{dt^3}, \tag{10}$$

where c is the speed of light in vacuum and ε_0 the permittivity of free space. By assuming harmonic motion $x(t) = x_0 e^{i\omega t}$, the steady state solution of Eq. (10) can be written as,

$$x(t) = \frac{AE_0}{(\omega_0^2 - \omega^2) + i(\omega\Gamma_a + \omega^3\Gamma_s)} e^{i\omega t}, \tag{11}$$

where the quantities q, k, m, and γ are replaced with more general oscillator parameters $A = \frac{q}{m}$, $\omega_0 = \sqrt{k/m}$, $\Gamma_a = \frac{\gamma}{m}$, and $\Gamma_s = \frac{2}{3}\frac{q^2}{mc^3}$, where Γ_a and Γ_s describe the non-radiative and radiative damping mechanisms, respectively. From Eq. (11) it is seen that the amplitude of oscillation is in phase with the incident field for $\omega \to 0$ and is phase delayed by π for $\omega \to \infty$, acquiring any intermediate value as the frequency of the signal is swept across the resonance and, in particular, a value of $\pi/2$ when $\omega = \omega_0$.

As mentioned previously the first realized flat metalenses used gold V-antennas with a design similar to the one shown in Figure 3 as the surface which would impart the abrupt phase change necessary to create a lensing effect.

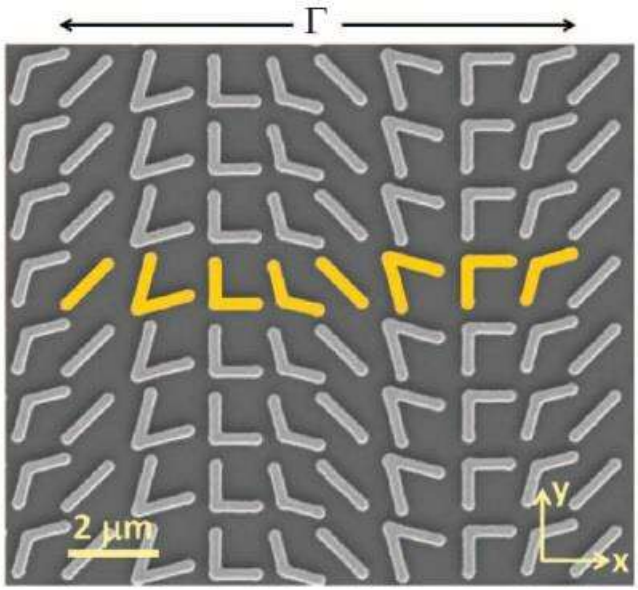

Figure 3. Scanning Electron Microscope (SEM) image of a representative antenna array fabricated on a silicon wafer. The unit cell of the plasmonic interface (yellow) comprises eight gold V-antennas of width ~220 nm and thickness ~50 nm, and it repeats with a periodicity of Γ = 11 μm in the x direction and 1.5 μm in the y direction. The V-antenna shown here are linearly spaced. Image taken from source with permission [6].

This metalens worked by utilizing the double-resonance properties of V-shaped antennas, which consist of two arms of equal length h connected at one end at an angle Δ, as is shown in Figure 4 [6]. Two unit vectors are defined to describe the orientation of a V-antenna: $\hat{s}$ along the symmetry axis of the antenna and $\hat{a}$ perpendicular to $\hat{s}$. V-antenna support "symmetric" and "anti-symmetric" modes, which are excited by electric field components along the $\hat{s}$ and $\hat{a}$ axes respectively. These modal properties of the V-antenna allow for the design of the amplitude, phase, and polarization state of the scattered light.

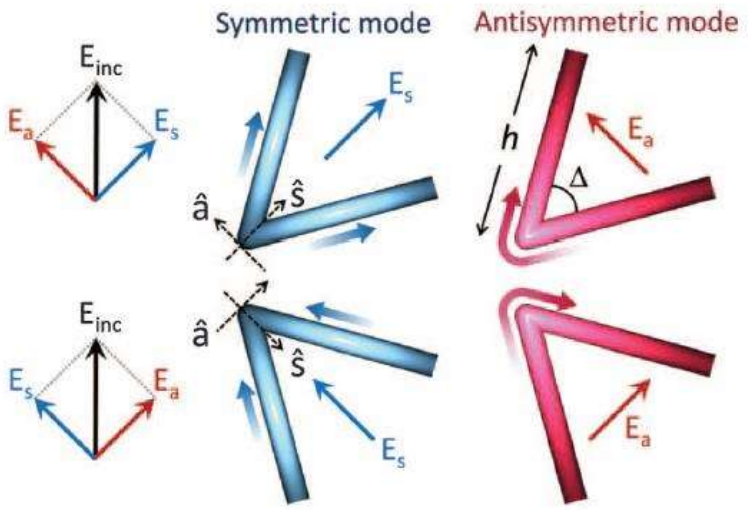

Figure 4. A V-antenna supports symmetric and antisymmetric modes, which are excited, respectively, by components of the incident field along $\hat{\boldsymbol{s}}$ and $\hat{\boldsymbol{a}}$ axis. The angle between the incident polarization and the antenna symmetry axis is 45º. The schematic current distribution is represented by colors on the antenna (blue for symmetric and red for antisymmetric mode), with brighter color representing larger currents. The direction of current flow is indicated by arrows with color gradient. Image taken from source with permission [6].

The gold V-antennas allow phase shifts that cover the 0-to-2π range, which is needed to provide full control of the wavefront. This is shown in Figure 5, which shows analytical calculations of the phase shift and amplitude of a wave scattered off of a gold V-antenna at a design wavelength $\lambda_0 = 8\,\mu m$ as a function of rod length and vertex angle. In Figure 5, there are four circles that correspond to the four values of rod length h and vertex angle Δ that were used in that specific experiment [6]. Between each of the circles there is an increment in phase of $\pi/4$ from left to right for the cross-polarized scattered light. By simply taking the mirror structure of a specific design, a new antenna was created that had an additional π phase shift. This allowed the four chosen antenna designs to create a metasurface lens that covered the entirety of the 0-to-2π range. The left graph of Figure 5

also shows that the chosen designs ensured that the scattered amplitude of all the antennas would be nearly equal.

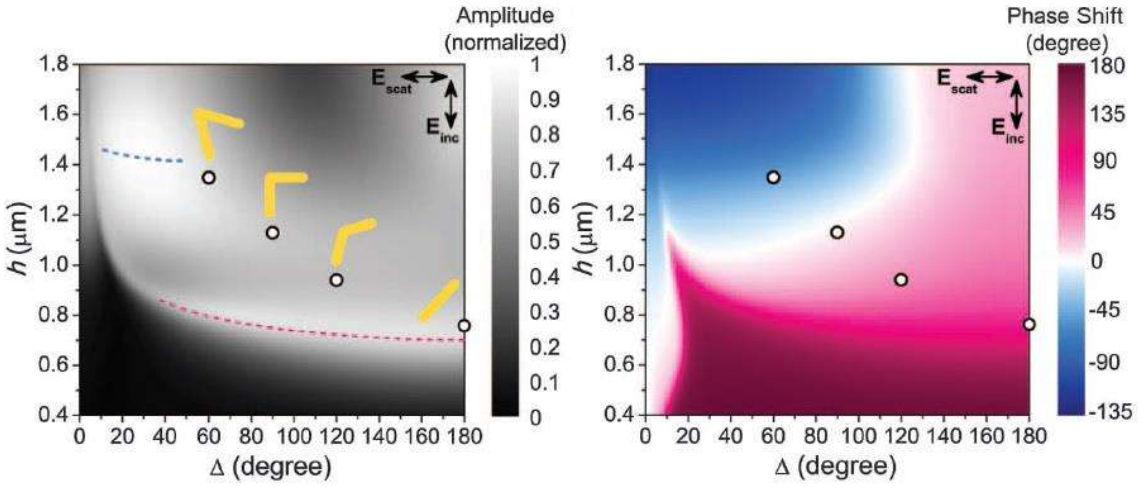

Figure 5. Analytically calculated amplitude and phase shift of the cross-polarized scattered light for V-antennas consisting of gold rods with a circular cross-section and with various lengths h and angle between the rods Δ at $\lambda_o = 8$ μm. The four circles indicate the values of h and Δ used in the experiment [33]. The blue and red dashed curves correspond to the resonance peaks of the symmetric and anti-symmetric modes. Image taken from source with permission [6].

The first fabricated V-antennas were designed to operate at telecom wavelengths, $\lambda_0 = 1.55\ \mu m$. Aieta used the same methodology laid out previously for the design of his metalenses and used the repeating eight pattern V-antenna design that is shown in Figure 3 [40]. Although the V-antennas that Aieta built were successful, they were very inefficient, only achieving a focusing efficiency that was approximately 1%. Further study of Aieta's structure revealed that the maximum cross-polarized transmission that his lenses would be able to achieve was 25% [41], and this limit was applicable to any in-plane plasmonic metasurface.

2.5 Out-of-Plane Plasmonic Metalenses

The fundamental 25% transmission limit motivated Adomanis' study to design his own plasmonic metalenses [42]. These metalenses were based around plasmonic scatterers that were situated in a plane aligned with the direction of propagation, or out of plane (OOP) of the fabrication substrate, which improved the transmission efficiency to greater than 50%.

The main reason why the in-plane architecture is unable to achieve a greater than 25% transmittance is because there is no control over the magnetic response of the material, which is required for effective wavefront manipulation from a planar surface [58, 59]. Without control over the magnetic response of the material, the impedance cannot be tuned for efficient coupling into the surface, and this leads to high insertion loss, primarily due to reflection, and no suppression of backward propagating modes. In order to design for this there are three methods that can be employed which are the stacked-layer approach [60, 61], the guided-wave approach [59], and the lumped circuit element (LCE) approach [62].

Adomanis chose the LCE approach to design his metalenses, which can generate the electric and magnetic responses independently. Many of these designs consist of a capacitively loaded dipole-like element aligned to the incident E-field and an inductively loaded loop-like element aligned OOP for coupling of the H-field. Pfeiffer & Garbic [60] presented a thorough analysis of these structures, tuning the structures to behave as Huygen's sources with extremely low backscatter, and showed a peak transmission efficiency of 86% into the desired diffraction mode. Huygen's principle states that every

point along a wave's phase front acts as a new source of waves that expand spherically such that the phasefront at some later time is the envelope of these wavelets. The Huygens-Fresnel principle introduces the concept of interference and states that the amplitude of the optical field at any point beyond is the superposition of all these wavelets, and that these wavelets add in the direction of propagation. In this sense a metamaterial Huygen's source is one in which the transmission of the metamaterial is mainly along the direction of propagation [63].

A Huygen's source can be formulated by defining a domain that is split into two regions by a surface S at $z = 0$, with propagating free space plane wave sourced at $z = -\infty$ with amplitude E_0, wavenumber $k_0 = 2\pi/\lambda_0$ and in free space impedance Z_0, where the incident fields are [64],

$$\begin{Bmatrix} \bar{E}^i \\ \bar{H}^i \end{Bmatrix} = \begin{Bmatrix} \hat{x} E_0 e^{-ik_0 z} \\ \hat{y} \frac{E_0}{Z_0} e^{-ik_0 z} \end{Bmatrix}, \tag{12}$$

where the incident electric field $\bar{E}^i$ oscillates along the $\hat{x}$ direction and the incident magnetic field $\bar{H}^i$ oscillates along the $\hat{y}$ direction.

By invoking Love's Equivalence Principle [65] we can consider a problem in which the fields in region one ($z < 0$) are replaced by equivalent currents on the surface S at $z = 0$. The equivalent currents on S must be such that this wave is continuing to propagate forward, with no backward propagation. Current calculations can be carried out as given by the following,

$$\begin{Bmatrix} \bar{J}_s \\ \bar{M}_s \end{Bmatrix} = \begin{Bmatrix} \hat{n} \times \bar{H}_s \\ \bar{E}_s \times \hat{n} \end{Bmatrix}, \tag{13}$$

where $\bar{J}_s$, $\bar{M}_s$ are the electric and magnetic currents on a closed surface respectively, $\bar{H}_s$ and $\bar{E}_s$ are the magnetic and electric fields on this closed surface respectively and $\hat{n}$ is a unit vector perpendicular to this closed surface. Equation (13) leads to the result,

$$\begin{Bmatrix} \bar{J}_s \\ \bar{M}_s \end{Bmatrix} = \begin{Bmatrix} -\hat{x}\frac{E_0}{Z_0} \\ -\hat{y}E_0 \end{Bmatrix}, \tag{14}$$

and by solving for the well-known vector potential equation, the fields in each region are given, for the electric current (e),

$$\begin{Bmatrix} \bar{E}_e \\ \bar{H}_e \end{Bmatrix} = \begin{cases} \begin{Bmatrix} \hat{x}\frac{E_0}{2}e^{ik_0 z} \\ -\hat{y}\frac{E_0}{2Z_0}e^{ik_0 z} \end{Bmatrix} & z < 0 \\ \begin{Bmatrix} \hat{x}\frac{E_0}{2}e^{-ik_0 z} \\ \hat{y}\frac{E_0}{2Z_0}e^{-ik_0 z} \end{Bmatrix} & z > 0 \end{cases}, \tag{15}$$

and for the magnetic current (m),

$$\begin{Bmatrix} \bar{E}_m \\ \bar{H}_m \end{Bmatrix} = \begin{cases} \begin{Bmatrix} -\hat{x}\frac{E_0}{2}e^{ik_0 z} \\ \hat{y}\frac{E_0}{2Z_0}e^{ik_0 z} \end{Bmatrix} & z < 0 \\ \begin{Bmatrix} \hat{x}\frac{E_0}{2}e^{-ik_0 z} \\ \hat{y}\frac{E_0}{2Z_0}e^{-ik_0 z} \end{Bmatrix} & z > 0 \end{cases}. \tag{16}$$

When the contributions are added from the symmetric fields due to the electric current source and the anti-symmetric fields due to the magnetic current source, the remaining fields are only in the $z > 0$ region. This also adds insight to the limitation that was previously mentioned for the plasmonic in-plane metasurface, where a surface

generating only a symmetric field cannot suppress a backward propagation and loses 50% of its power in this direction.

Of course, as mentioned previously, the only way to achieve this simultaneous control over the electric and magnetic fields is by use of a structure that is in the plane of propagation or OOP of the fabrication substrate. Adomanis designed his novel OOP metasurface by the use of a genetic algorithm (GA) to iteratively arrive at the best design that would achieve maximum forward propagation while minimizing the backward propagation, and to do this while still covering the 0-to-2π phase shift that is required for flat metalenses.

Due to the fact that the current research did not use a GA, I will not cover the concepts that describe how it works here. However, it is important to note that the two structures that were studied in this dissertation, those designed by Adomanis and those designed by Pennsylvania State University (PSU), were both designed by this methodology. However, I will discuss the materials around which the metalenses were designed. Figure 6 shows a concept design for the OOP metalens. As can be seen, the square boxes, which are referred to in this document as "voxels", are either filled or not. These filled or not-filled states correspond either to metal or air in that specific voxel respectively. The GA arrives at a specific configuration of these voxels which provides the desired phase shifts, while maintaining the maximum amplitude available.

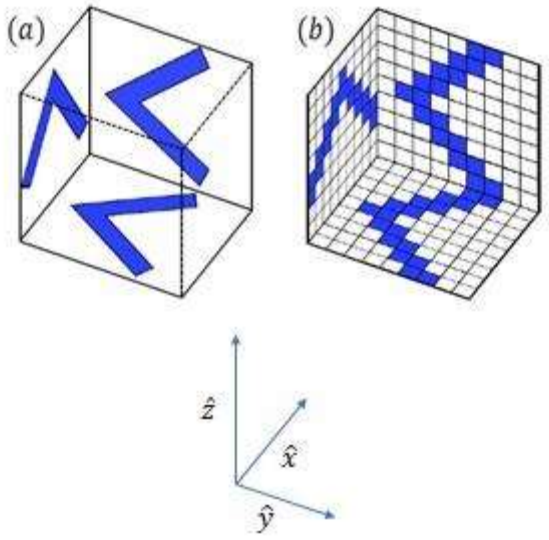

Figure 6. Concept architecture for supporting out-of-plane (OOP) scatterer. (a) An analog scatterer can be supported on vertical walls and floor of a cavity. (b) By deconstructing the walls into grids of 3D pixels, i.e. voxels, the grids can be optimized using a genetic algorithm routine by switching the voxels in a binary operation between metal or air. Image taken from source [42].

From the GA, Adomanis obtained eight different voxel layouts that covered the 0-to-2π phase were designed, with a mean absolute transmittance of $\langle T \rangle = 0.658$, which compares favorably to the maximum cap of 25% possible for in-plane plasmonics. There are two sets of phase elements, one by Adomanis and one by the PSU group. These two sets were fabricated in two different device configurations which are explained in the next section.

2.6 Fabricated Metasurface Devices

The previous section introduced the OOP phase elements, and mentioned the design of two distinct phase element sets, one by Adomanis and one by the PSU group. These two

sets were designed to work as a metasurface blazed transmissive diffraction grating, or a "beamsteerer", and the two different beamsteerers will be referred to in this document as the "blazed-grating" and "phased-array" designs, for the set designed by Adomanis and PSU, respectively. There were several differences between the two designs, which include their design wavelength, the size of their Membrane Projection Lithography (MPL) cavities (described later), the substrate material used, and most importantly the way in which the phase elements were arrayed with respect to one another. The terms blazed-grating and phased-array are specifically related to the orientation of the phase wrapping with respect to the polarization direction. These two designs are shown in Figures 7 and 8, where Figure 7 shows the blazed-grating and Figure 8 shows the phased-array beamsteerer designs. Figures 7 (a) and 8 (a) show the FEM models as they appeared in the modeling environment in which the beamsteerers were designed, COMSOL Multiphysics®.

The two beamsteering designs had to be tailored to the MPL fabrication technique. The fact that the phase elements had to be designed as decorations on a substrate sidewall meant that there were only a few changes that could be made from one design to the other, but one of the few differences incorporated is the direction of the phase wrap, shown in both Figures 7 and 8. For the blazed-grating (Figure 7) the phase elements repeat in the direction orthogonal to the design polarization. Light propagates tangentially to the side-wall decorations, the z direction in Figure 7. The E field of the propagating light is then aligned with the plasmonic decorations, the x dimension in Figure 7. There is only one like element like element along the polarization direction.

For the phased-array design (Figure 8), all like elements lie along the direction of polarization, again the $\hat{x}$ direction in Figure 8, with the successive phase elements arranged in the direction orthogonal to the polarization, the $\hat{y}$ direction in Figure 8.

Another noticeable difference between the two designs is that for the blazed-grating design only four different elements were used (#1, #3, #5, and #7), whereas for the phased-array design all eight design elements (#1 - #8) were used. This was due to the fabrication limitations at the time that the blazed-grating array was built, not due to a design specification. It is important to note that when discussing the fabricated devices, elements #1, #3, #5, and #7 shown in Figure 7 (b) are not the same elements #1, #3, #5, and #7 in Figure 8 (b). Figures 7 (a) and 8 (a) show the differences between the two sets of phase elements.

Both the blazed-grating and phased-array beamsteerer designs work in a similar fashion. Gold decorations that are oriented along the excitation polarization induce an amplitude and phase shift in the incoming light aligned along the excitation polarization. The amplitude response is designed to be maximized and uniform across the phase elements, and the phase response is designed to cover the 0-to-2π phase shift required.

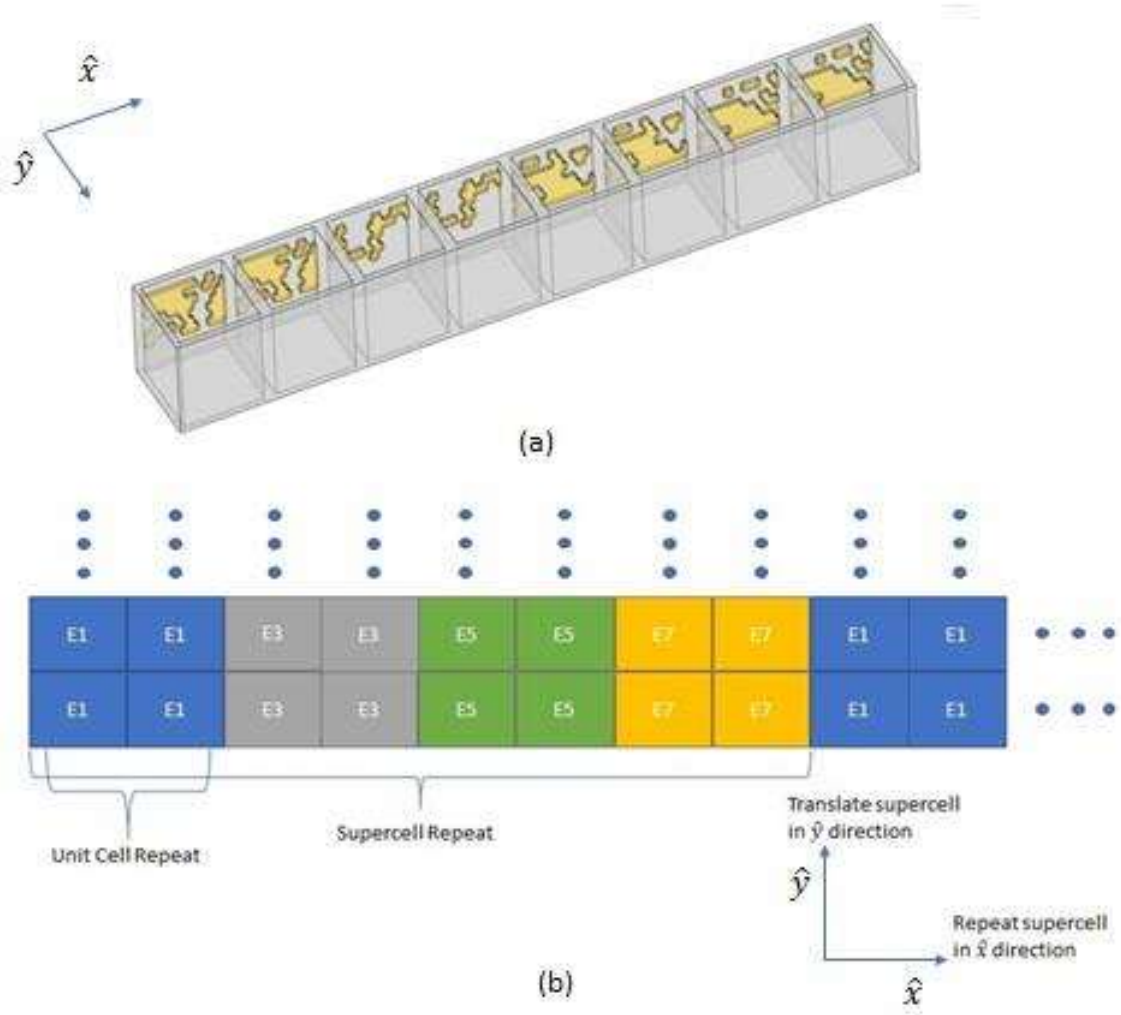

Figure 7. Eight element supercell that was used for the fabrication of the blazed-grating device, showing (a) the FEM model used in COMSOL, and (b) a sketch of how the supercell repeated in the fabricated device. The design polarization is along the $\hat{\boldsymbol{x}}$ direction. For the blazed-grating design only four of the eight designed elements are used. In the blazed-grating design there are repetitions of like elements in the $\hat{\boldsymbol{y}}$ direction, while there is only one neighboring like element in the $\hat{\boldsymbol{x}}$ direction.

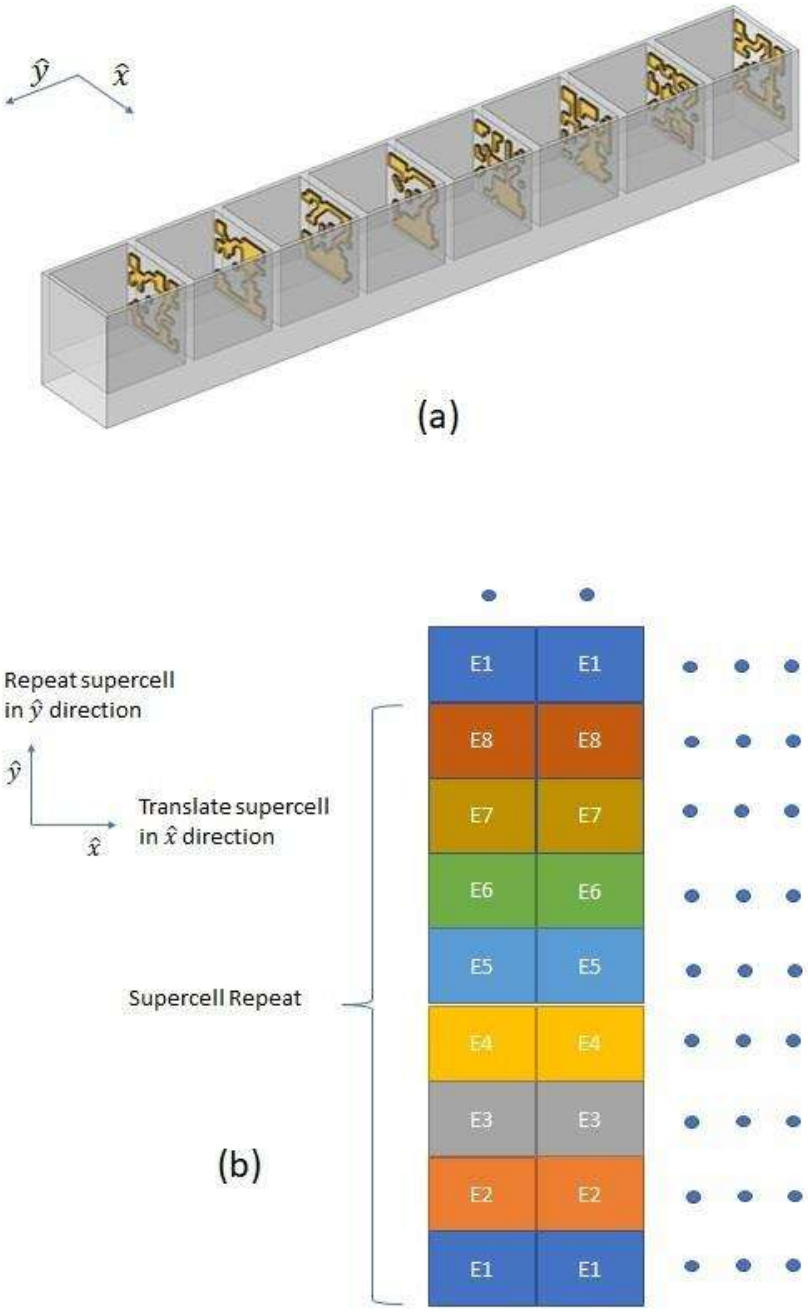

Figure 8. Eight element supercell that was used for the fabrication of the phased-array device, showing (a) the FEM model used in COMSOL, and (b) a sketch of how the supercell repeated in the fabricated device. The design polarization is along the $\hat{\boldsymbol{x}}$ direction. For the phased-array design all eight designed elements are used. In the phased-array design there like elements repeat in the $\hat{\boldsymbol{x}}$ direction, while the $\hat{\boldsymbol{y}}$ direction has the succession of the eight element phase wrap.

The phase elements used in both types of beamsteerers were also designed in a similar fashion. They were designed in an isolated unit cell, with periodic boundary conditions (PBC) along the $\hat{x}$ and $\hat{y}$ directions (referring to Figures 7 (a) and 8 (a)) and were iterated through a GA until the desired phase shifts and amplitudes were achieved. Thus, a disconnect between the design environment and the fabricated device can quickly be seen for both types of beamsteerers.

For both beamsteerers, the phase elements are not surrounded by like elements in both the $\hat{x}$ and $\hat{y}$ directions, which the PBC imply. In the phased-array configuration there are copies of like elements along $\pm\hat{x}$, but no like elements in the $\hat{y}$ direction. In the blazed-grating design there is only one neighboring like element in the $\hat{x}$ direction for each phase element, with like elements along $\pm\hat{y}$. This means that if the phase elements require adjacent like elements in order to achieve the desired phase shift and amplitude designed, the tiling of the phase elements in both types of beamsteerer designs already breaks this requirement. Regardless, even if the phase element is surrounded by like elements, these may not be *identical* copies due to fabrication limitations, which could further degrade the performance of the fabricated devices.

2.7 Membrane Projection Lithography

The two different beamsteerers described previously were fabricated using Membrane Projection Lithography (MPL), which is a variation of stencil lithography, which uses microelectromechanical system (MEMS) processing steps to fabricate arrays of micron-scale unit cells [44 – 47] Figure 9. These unit cells are decorated with plasmonic

meta-atoms, or phase elements, aligned along any of the coordinate axes, although for both fabricated metasurface optical devices used here, only one side was decorated (Figure 9 (f)). It is these phase elements that allow the device to have its unique properties. Unit cells can be decorated with a variety of phase elements, which in turn allow for unique electromagnetic scattering behaviors that are not possible with planar designs. The generic MPL process flow is shown in Figure 9. The steps are (a) the creation of the cavity, which is accomplished either by an additive or subtractive process, (b) backfilling the cavity with a sacrificial material, (c) planarizing the sacrificial material, (d) overlaying the membrane mask, (e) evacuating the sacrificial material, (f) depositing the meta-atom through the membrane mask, and lifting off the membrane mask (not shown).

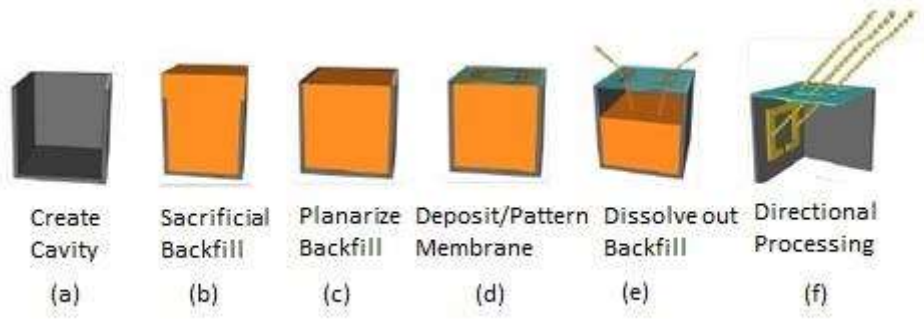

Figure 9. Schematic flow of the generic membrane projection lithography process. Image taken from source with permission [47].

In the case of both the blazed-grating and the phased-array designs, the meta-atoms were gold, but the substrates were not the same. For the blazed-grating beamsteerer the substrate in which the cavities were carved was silicon (Si), whereas for the phased-array device it was silicon nitrate (Si_3N_4). Another change was that the size of the cavities was increased from a cube with side length $w = 2.3\ \mu m$ for the blazed-grating device to a side length $w = 3\ \mu m$ for the phased-array device.

A variety of errors was identified during the fabrication of the blazed-grating beamsteerer which resulted from the MPL procedure. The level of complexity that the plasmonic metasurfaces required from the MPL process was one that had never been attempted before at Sandia National Laboratories (SNL, where the devices were fabricated) or anywhere else. The first issue that had to be addressed was reducing the thickness of the gold decoration due to a phenomenon known as "aperture clogging," which occured during the deposition process [46]. To curtail this effect the thickness of the gold decorations was reduced from 150nm to 100nm. This can become an issue due to the fact that at $\lambda = 8\ \mu m$, the design wavelength for the blazed-grating device, the skin depth of gold is around 23 nm. This reduction in the thickness of the gold decoration also affects the overall phase change and transmittance of the metasurface, and it was found that in order for the transmittance to stay above 50%, the metal thickness should remain between ~110 – 215 nm. Another effect that is encountered with MPL is dispersion of the metal as it is being deposited. This ultimately affect the precision of the MPL process and effectively limits it to being a low-precision process.

Lastly there was an issue that was noticed during the fabrication of other membranes using MPL, and that was an issue of curvature that was present in the vertical joints around the interior of the cavity. Without the curvature present it was assumed that the current induced from the electric response of the OOP scatterer was confined to the incidence plane (x-z plane in Figures 7 (a) and 8 (a)) and the magnetic response was confined to the orthogonal plane (H_y). With the curvature present there is the potential for an additional component to be generated for each response: a $\hat{y}$-directed current (I_y) and an $\hat{x}$-directed magnetic field (H_x).

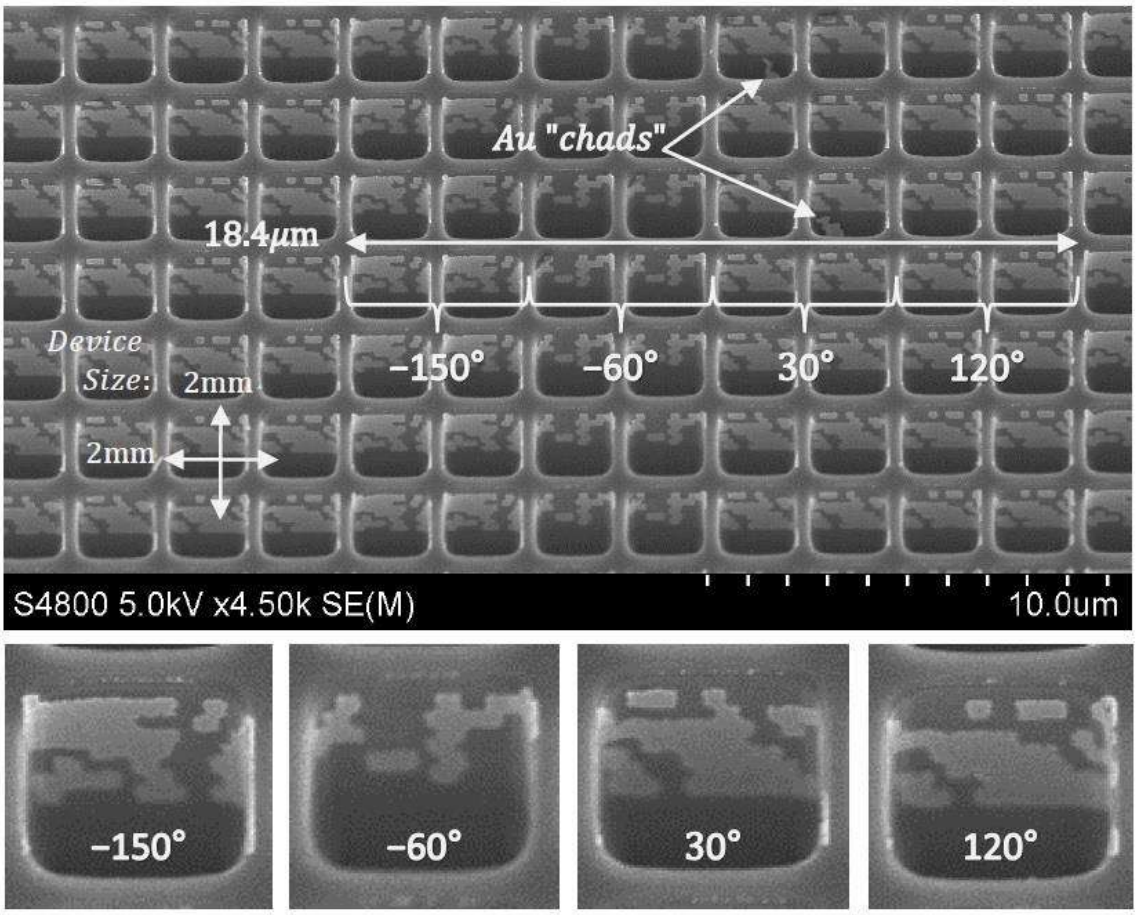

Figure 10. SEM of final, full scale beamsteering blazed-grating device, along with enlarged images of each element. Image taken from source [42].

The blazed-grating beamsteerer was designed with all these issues in mind. For the blazed-grating beamsteerer, a repeating four-element design was used. This was done to try to compensate for uncertainties in the fabrication of the plasmonic metasurfaces using the MPL methodology, and it was deemed to be good for a proof of concept. An SEM image of the fabricated blazed-grating beamsteerer experimental device is shown in Figure 10.

2.8 Background and Theory Summary

This chapter encompassed a small subset of the theory that lies at the heart of how metasurface optics operate. The first topic discussed was the generalized theory of refraction and reflection, which adds the effect of an abrupt phase shift at the interface into both Snell's law and the law of reflection. This abrupt phase shift is the key phenomenon which metasurface optics aim to exploit in order to replicate the behavior of a refractive optic but on a smaller scale. The next sections discussed how these abrupt phase shifts are incorporated into an optical device in order to achieve this behavior. A discussion on plasmonic scatterers, which is one of the methods used to impart the necessary phase shift, was included.

The first designed metasurface optical device, the V-antenna device, which imparted an abrupt phase shift using gold nanoantennas to act as these plasmonic scatterers, was introduced. The V-antenna devices are theoretically limited at 25% efficiency due to their in-plane orientation. This limit in transmission motivated the work that preceded this one, which culminated in out-of-plane (OOP) plasmonic gold decorations which improved upon the 25% transmission limitation, and led to the design of the devices which were studied in this research.

The two different devices studied here were detailed and their similarities and differences noted. The main difference between the two is the direction of the phase wrap, which is the succession of phase elements that cover the 0-to-2π range. This difference leads to the designation of the two transmissive blazed diffraction grating, or beamsteering, devices, with the device that has its phase wrap aligned with the polarization direction

termed the blazed-grating device, and the device with the phase wrap orthogonal to this direction termed the phased-array device.

It was also noted that the specific metasurface optical devices which could be realized with the designed phase elements were limited by the technique that was used for their fabrication, Membrane Projection Lithography (MPL). In order to achieve greater control of the incoming EM wave, the phase elements had to be designed in an OOP configuration, which the MPL technique achieves by placing the plasmonic phase elements on the walls of the cavities fabricated in the substrate. This limits the choices of how the phase elements can be configured in the device and led to the two configurations used in this work, the blazed-grating and phased-array designs.

III. Research Methodology

3.1 Introduction

This chapter covers the methodology used in obtaining the physical measurements and the models used for comparison in the experiment. The comparisons between measurements and modeling results are key to understanding the defects that are present in the fabricated devices and what effects these defects have on the performance of the devices.

The first section of this chapter will cover the CASI and explain the measurements of the fabricated devices that were completed. This will help the reader in understanding the methodology later employed in the models, and understand the similarities and differences between the models and the measurements.

The next section will then outline the modeling methodology employed in this experiment, which is the main area of focus of the work accomplished for this effort. The modeling methodology can be summarized as a two-step process in which the near fields are calculated using a full-wave solver and those are then propagated to the far-field using the Stratton-Chu formulation [66] to simulate what is obtained by the physical measurements.

3.2 Complete Angle Scatter Instrument (CASI) Measurements

The device used at AFIT to measure the performance of the fabricated devices is known as the "Complete Angle Scatter Instrument" (CASI®), developed by Schmitt

Measurement Systems [48-50]. This device is able to measure the Bidirectional Transmittance Distribution Function (BTDF) of a sample.

The BTDF (τ) in units of sr^{-1}, relates the transmitted radiance (L_t^e or the radiant flux density per unit solid angle in $W \cdot m^{-2} \cdot sr^{-1}$) to the incident irradiance (E_i^e or the radiant flux density in $W \cdot m^{-2}$) as a function of both incident and transmitted angles in a spherical space, where θ is the elevation angle with respect to the transmitting surface normal and ϕ the azimuthal angle about that normal, and subscripts i or t mean incident or transmitted, respectively,

$$\tau(\Omega_i, \Omega_t) = \frac{L_t^e}{E_i^e} = \frac{\partial^2 P_t^e}{\partial A_t \cos\ {}_t \partial \Omega_t} \frac{\partial A_i}{\partial P_i^e} = \frac{P_t^e}{\Omega_t} \frac{1}{P_i^e \cos\theta_t}, \tag{17}$$

where P_e is radiant flux, $A_{i,t}$ are incident or transmitted areas, assumed to be the same, and Ω_t is the solid angle into which the transmitted radiation flows.

The CASI allows measurement of τ by first measuring P_i^e at normal incidence (θ_i = 0, ϕ_i = 0) and then P_t^e through a selected aperture at a set distance (in this case 50 cm), which provides a known Ω_t, as the transmitted elevation angle is swept -90° ≤ θ_t ≤ 90°, and in this case, ϕ_t = 0 to measure only in the plane of incidence. Uncertainty analysis for Bidirectional Scatter Distribution Function (BSDF, either BTDF or Bidirectional Reflectance Distribution Function (BRDF)) calculations generally follow that detailed in Stover [67] or Cady et al [68]. The primary sources of uncertainty for BSDF measurements are aperture misalignment, aperture size uncertainty, detector nonlinearity and scattering error (at grazing angles in particular, not pertinent here). Measurement uncertainties

(ΔBSDF/BSDF) calculated for the AFIT CASI have been very small, e.g., <18% measured at one data point (0.011°) from the specular direction (0° for BTDF) to <11% at two data points and <8% beyond 0.5° away [69].

A schematic of the CASI setup is shown in Figure 11. As shown in the sketch, two linear polarizers are used to achieve the four linear polarization configurations, which could be envisioned in the figure as horizontal incident/horizontal measured (H/H), vertical incident/vertical measured (V/V), H/V and V/H. All four were collected, but only H/H will be primarily focused upon here since that is the polarization state in which the beamsteerers were designed to operate.

The CASI is able to use six tunable external-cavity quantum-cascade lasers (Daylight Solutions®) in order to span a nearly continuous range of mid-wave IR (4.37 - 6.54 μm) and long-wave IR (7.41-9.71 μm) wavelengths and also has an added capability for two fixed-wavelengths at 3.39 μm (HeNe) and at 10.6 μm (CO_2). In addition, an achromatic Dual Rotating Retarder polarimeter with automated rotation stages, was also incorporated in the CASI, which allows it to be a spectrally tunable IR Mueller matrix (Mm) polarimetric scatterometer, which can be tuned into and out of narrowband performance regions of nanostructured optical materials, such as the beamsteerers. While the CASI is able to extract the full Mm of a material, those measurements were not carried out on the devices under study here. For these devices only the BTDF with respect to two incident and scattered polarizations was studied, with the blazed-grating device characterized at one wavelength, $\lambda = 8\mu m$, and the phased-array device at four wavelengths $\lambda = 5.5, 6.0, 6.25$, and 6.5 μm.

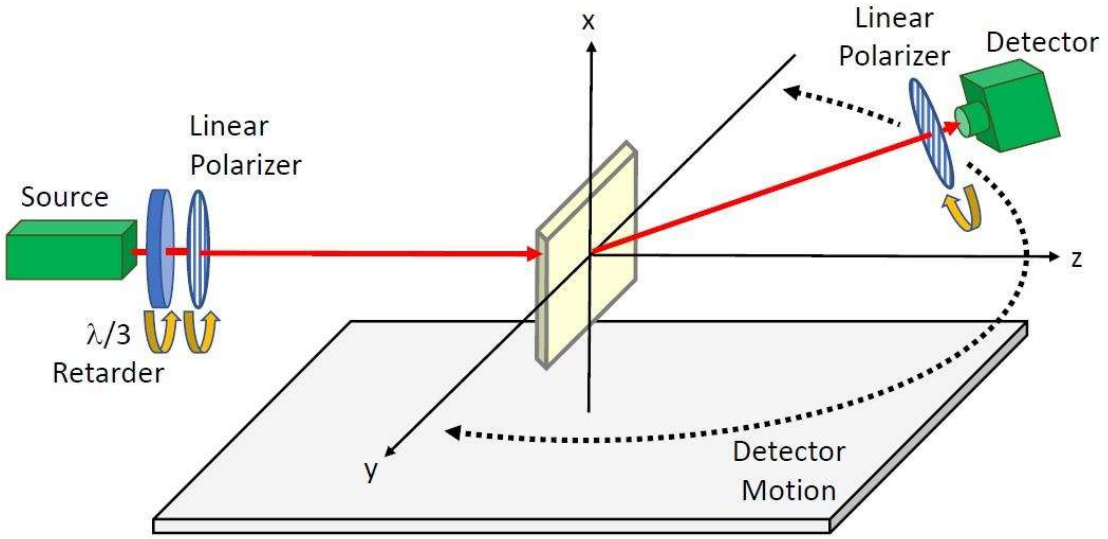

Figure 11. Schematic of SMS CASI BTDF system. The laser source is a Daylight Solutions tunable External-Cavity Quantum-Cascade Laser set at 8-μm wavelength. The retarder is an achromatic nominally λ/3 plate with actual retardance of 119◦at 8μm. The linear polarizer selects either vertical or horizontal polarization; the retarder is rotated to maximize throughput for that polarization. The beam is incident normal to the sample surface, although the sample could be rotated about the x-axis for non-normal incidence. The analyzing polarizer and detector rotate about the sample on a goniometer arm to measure in-plane scatter +/- 90◦from the sample surface normal (i.e. the z-axis). The linear polarizer selects either vertical or horizontal polarization so both co-polarization and cross-polarization measurements can be made.

3.3 Computational Modeling Methodology

This section will cover the different computational methods employed in order to simulate the measurements obtained by the CASI, and will provide examples that help validate the results obtained from the computational models. As mentioned the majority of the results presented in this work were obtained via a two-step process.

The first step employed a computational electromagnetic (CEM) solver, in this case COMSOL Multiphysics® [55], in order to obtain the near fields above the modeled meta optic phase element. As a modeling environment COMSOL® provides many tools that

could be employed to add imperfections into the designed phase elements and thus served as a great tool that could simulate the behavior of many different defects.

The next step used the near fields obtained from COMSOL® and using a script written in MATLAB® to propagate the calculated near fields to the far field using the Stratton-Chu Formulation.

3.3.1 Finite Element Method

The Finite Element Method (FEM) is a method that attempts to solve partial differential equations (PDE) by approximations which take the form of different types of discretizations [53, 54]. PDE are prevalent in many branches of physics including electromagnetics and therefore FEM is one such method that can be used as a CEM solver to model different problems. In order for FEM to be useful both the governing PDE and the boundary conditions for a specific problem need to be known beforehand.

The basic concept of FEM can be thought of as splitting the computational domain into individual small patches and finding local solutions that satisfy the PDE within the boundary of this patch. By stitching the individual solutions of these patches back together, a global solution can be obtained.

It is important to note that there is a measure of uncertainty surrounding results obtained from COMSOL, and this uncertainty stems from the mesh used in the FEM environment [70]. This is due to the fact that solving an FEM simulation with the incorrect meshing will produce results that are incorrect. The results presented in this subsection, which use the same methodology for meshing the FEM models as those presented later in

the document, show that the meshing methodology adopted for this study produce results that are accurate.

In order to obtain the near fields using COMSOL® each phase element of the beamsteerer had a total of 36 probes placed half a wavelength above it, as shown in Figure 12, with each probe sampling the E_x, E_y, E_z, H_x, H_Y, and H_z fields necessary to use the Stratton-Chu formulation. Previous research completed by Adomanis [42] determined that using only one probe per phase element would produce far-field results that were not representative of the devices being fabricated, since each phase element would then become a single spherical emitter, which it is not. Thus a total of 36 probes per phase element was chosen in order to produce a radiation pattern that would accurately replicate the behavior of the designed phase elements while still being computationally efficient.

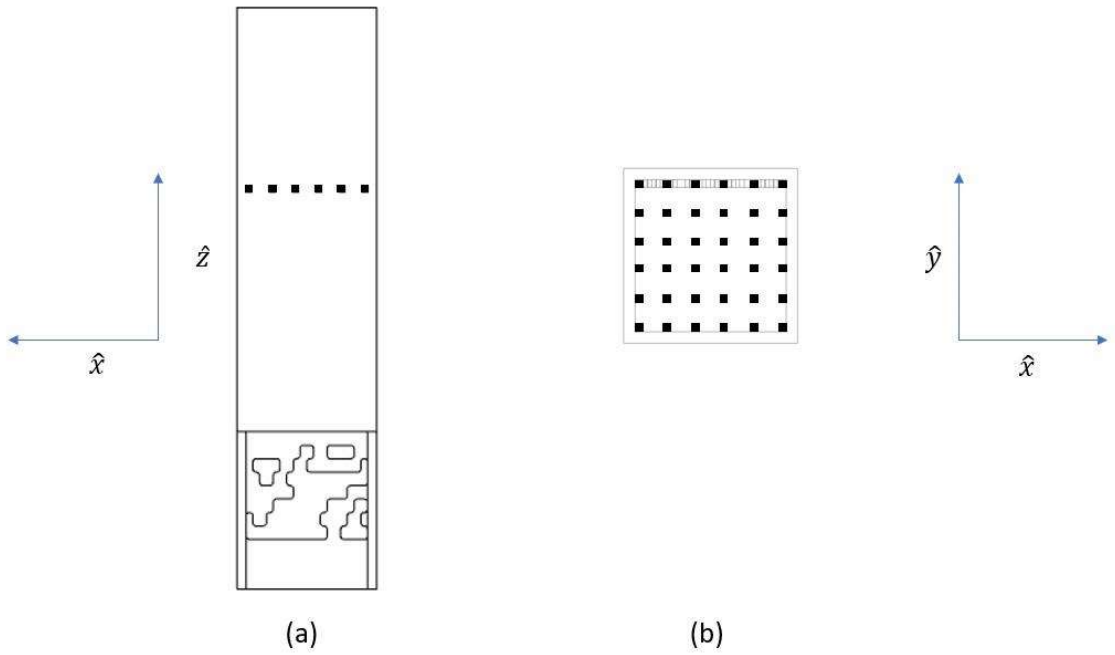

Figure 12. Probe setup used to obtain the near-fields from each individual phase element with (a) a front view, and (b) a top down view of the relative placement of the probes (the black squares), with respect to the phase element and to each other. For each probe the E_x, E_y, E_z, H_x, H_Y, and H_z fields were sampled, which would be then used in the Stratton-Chu equation to project to the far field.

Each probe was equidistant from its nearest neighbors and the probes at the edge were placed such that they maintain this same distance to a probe on an adjacent phase element. For an 8-element supercell model, each phase element would have the same number of probes placed above it at the same relative positions, for a total of 288 probes. Whether one-element or 8-element-supercell models were used in COMSOL®, the near fields collected by the probes were arrayed into a digital beamsteerer array in MATLAB® which was 108 supercells long and 1 supercell wide, and propagated to the far field using the Stratton-Chu formulation. Comparisons between digital beamsteerer arrays which were 108 x 1 array wide to square 108 x 108 arrays wide were carried out, and aside from an increase in magnitude, there was no discernible difference in the shapes of the calculated BTDFs, but there was a very noticeable time increase in calculating the BTDF of a rectangular array versus that of a square array. Calculating the far field of a rectangular array for 1000 points took on average 5 seconds, whereas the same number of points for a square array could take up to 30 minutes.

3.3.2 Stratton-Chu Formulation

The Stratton-Chu equation [66] was used to propagate the electric fields formed by the beamsteerer phase elements to the detector,

$$\bar{E}(\bar{r}) = \hat{r} \times i\frac{1}{2\lambda}\int\int [\hat{n} \times \bar{E}' - Z\hat{r} \times (\hat{n} \times \bar{H}')]exp(i2\pi\lambda\bar{r}' \cdot \hat{r})d\bar{S}' \qquad (18)$$

where the tangential fields $\bar{E}'$ and $\bar{H}'$ are the E_x, E_y, E_z, H_x, H_y and H_z taken from COMSOL® at a homogenous boundary $\bar{S}'$ above the phase element, $\hat{n}$ is the unit vector normal to $\bar{S}'$, $\bar{r}'$ is the vector from the origin to $\bar{S}'$, Z is the impedance of vacuum $\sqrt{\mu_o/\varepsilon_o}$, $\hat{r}$ is the unit vector from the origin to the point $\bar{r}$, and λ the vacuum wavelength of the light.

A discretized version of the Stratton-Chu formulation was used in my calculations, which had its axes aligned with those of Figures 7 (a) and 8 (a). In this case $d\bar{S}$ was in the $\hat{x}$ and $\hat{y}$ plane, with the polarization direction aligned with $\hat{x}$ direction, and $\hat{n}$, the direction of propagation, was aligned with $\hat{z}$.

The discretized version of the Stratton-Chu Formulation that was used was of the form,

$$\bar{E}(\bar{r}) = \frac{i\,dx\,dy \exp\left(i\ {}^{2\pi}/_{\lambda}\left((x-x')^2 + y'^2 + z^2\right)\right)}{2\lambda((x-x')^2 + y'^2 + z^2)^2}$$

$$\times \sum_{i,j=1}^{N} \left\{ \begin{array}{c} -\hat{x}\left[zE_{x'}^{i,j} + \dfrac{Z\left(z^2\, H_{y'}^{i,j} + y\,\left(y'\, H_{y'}^{i,j} + \,(x-x')H_{x'}^{i,j}\right)\right)}{((x-x')^2 + y'^2 + z^2)} \right] \\ \hat{y}\left[-zE_{y'}^{i,j} + \dfrac{Z\left(z^2\, H_{x'}^{i,j} + (x-x')\,\left(y'\, H_{y'}^{i,j} + \,(x-x')H_{x'}^{i,j}\right)\right)}{((x-x')^2 + y'^2 + z^2)} \right] \\ \hat{z}\left[y'\, E_{y'}^{i,j} + (x-x')E_{x'}^{i,j} + \dfrac{Z\left((x-x')zH_{y}^{i,j} - z\, y'H_{x'}^{i,j}\right)}{((x-x')^2 + y'^2 + z^2)} \right] \end{array} \right\}, \quad (19)$$

where dx and dy are given by the distance between probes along both x and y directions, x and x' corresponded to the coordinate at which the far field was being sampled and of the probe respectively in the $\hat{x}$ direction, y' was the coordinate of the probe in the $\hat{y}$ direction, and z the coordinate at which the far field was being sampled in the $\hat{z}$ direction.

$E_{x'}^{i,j}$, $E_{y'}^{i,j}$, $H_{x'}^{i,j}$, and $H_{y'}^{i,j}$ corresponded to the electric and magnetic near fields obtained from the FEM models, and i and j are the x' and y' coordinates of the probes being sampled, and N summed over all the probes. Although the total number of probes was kept constant for all the results shown in the dissertation, it could be varied by adjusting the size of the simulated beamsteerer.

As mentioned in the previous section the entirety of the data presented in this dissertation is obtained from beamsteerer models that are composed of a rectangular array of 108 x 1 supercells, which would contain 5184 x 6 probes. The far field sampled from these probes was collected at a distance of 50 cm and it swept a ±90° arc about the surface normal of the sample, which would mimic the conditions under which the CASI® measurements were completed.

3.3.3 Validation of Computational Modeling Methodology

While the methods that will be used in order to obtain comparisons to the measured data have been presented, they have not been validated. In order to accept that the results presented are accurate representations of the measured devices it is important to show that these methods do provide accurate predictions of plasmonic metasurfaces. In order to prove the validity of this method we look to modeling a well-known plasmonic metasurface, the V-antenna metalenses, which are discussed in Section 2.4, using COMSOL® Multiphysics. The model used in COMSOL® is shown in Figure 13.

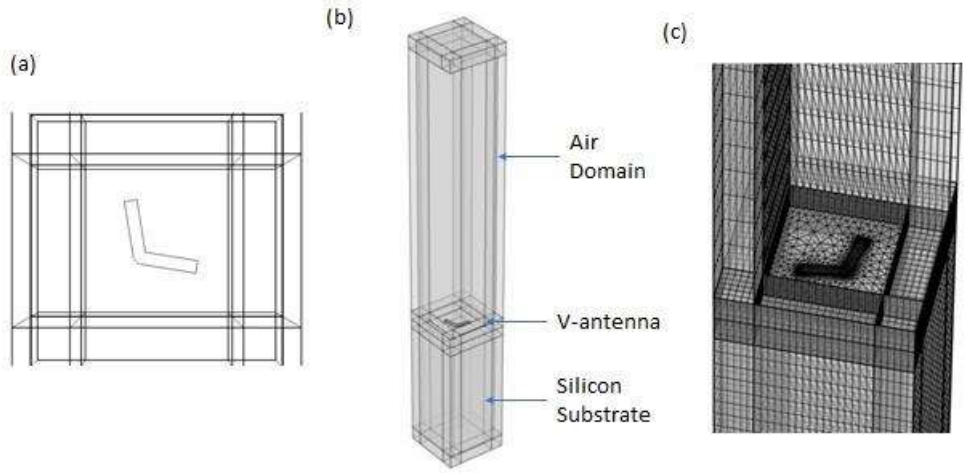

Figure 13. Different views of the V-antenna model used in COMSOL. (a) Top-down view of a V-antenna model built in COMSOL. (b) Full model view of the V-antenna model in COMSOL including the air domain and the silicon substrate on which the antenna is placed. The V-antenna is excited from the bottom of the silicon substrate. (c) View of the meshing used for this model.

The first results obtained from COMSOL® were the phase and amplitude responses that were analytically calculated for the V-antennas as shown in Figure 5. The values obtained from COMSOL® are shown in Figure 14, which includes the modeled amplitude and phase, (a) and (b), and the original amplitude and phase, (c) and (d). The modeled amplitude and phase were obtained by sampling over vertex angles ranging from 25° – 180° in 4° steps and half-dipole lengths from 0.7 – 1.6 μm in 0.05 μm steps. The analytical data covers from 0.4 – 1.8 μm and from 0° – 180°. The modeled and analytical data have clear overlaps showing that this methodology is accurate. Both amplitude plots show a region from 100° – 150° and 1.3 – 1.8 μm with lowered amplitude values, and there is a curve in the phase plot that corresponds to a 0° phase shift which is present in both the modeled and analytical plots. These plots show that COMSOL® accurately models gold

plasmonic metasurfaces at infrared wavelengths, which are the characteristics that we desire for our designed phase elements.

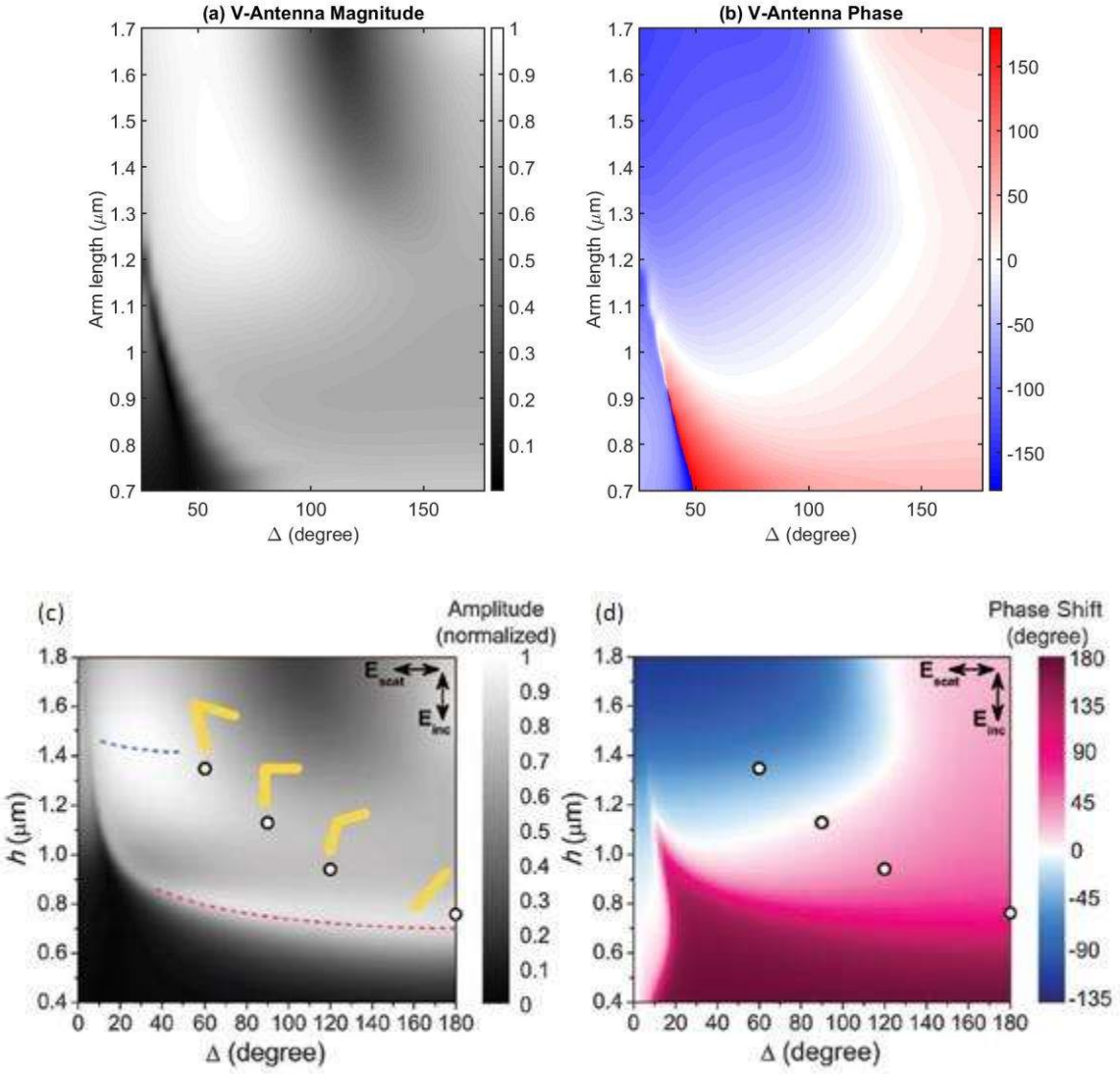

Figure 14. Comparison between modeled, (a) and (b), to analytical, (c) and (d), amplitude and phase of the cross-polarized light for V-antennas for a variety of lengths and angles between the rods at $\lambda_o = 8$ μm. Image, (c) and (d), taken from source with permission [6].

Near-fields obtained from COMSOL® are then propagated to the far-field using the Stratton-Chu formulation. Figure 15 shows an intensity heatmap for the scattered EM wave incident on a V-antenna beamsteerer designed using COMSOL®. The beamsteerer used eight designs that were based on the four circles outlined in Figure 14 (c) and (d). In order to cover the entire 0-to-2π phase range the four outlined designs had to be rotated by 180° which introduced a π phase shift. As mentioned in Section 2.4 the V-antenna metasurfaces impart the desired amplitude and phase shift on the cross-polarized component of the incoming EM wave. The Stratton-Chu Formulation has also been demonstrated by Adomanis to successfully propagate COMSOL® near-fields to the far-field [43].

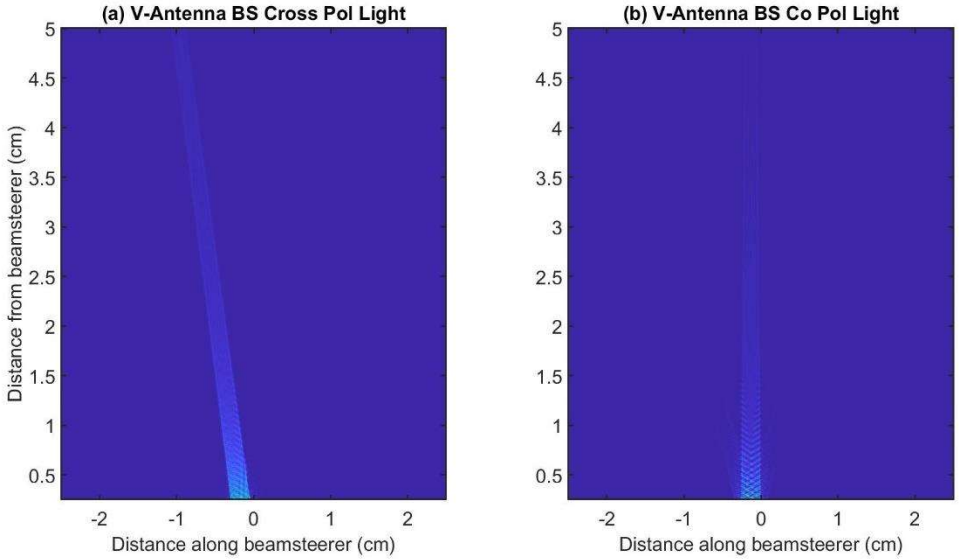

Figure 15. Heatmap of intensity for a V-antenna beamsteerer (BS) showing both the scattered (a) cross-polarized and (b) co-polarized light. The V-antenna device is designed to impart an abrupt amplitude and phase on the cross-polarized component of the incoming EM wave.

3.4 Research Methodology Summary

The two main sources of data that are discussed in this dissertation were presented in this chapter. The first is the measured data obtained from the fabricated metasurface devices. Both devices were characterized in terms of their bidirectional transmission distribution function (BTDF), and both were characterized for four different polarization configurations.

The second source of data was the computational data, which is first collected as near fields from a Finite Element Method (FEM) solver, and then propagated to the far-field using the Stratton-Chu Formulation. This combination will give simulated BTDF for different configurations of the fabricated devices, and will help me to understand the phenomena underlying the performance of the fabricated devices. Further it was shown by comparing simulated phase and amplitude profiles to analytical models that COMSOL® was accurate in its predictions of the behavior of gold plasmonic metasurfaces in the IR. Near-field data from COMSOL® in combination with the Stratton-Chu formulation showed that this combination also provided accurate predictions of the behavior of the V-antenna metasurfaces, which provided proof that this methodology is accurate in predicting the behavior of gold plasmonic elements in the IR for both near-field and far-field calculations.

IV. Measurements, Ideal Models, and Defect Study of the Blazed-Grating Beamsteering Device

4.1 Introduction

This chapter will discuss the results obtained from the measurements, the ideal models and the supercell models, and introduce various defect models accomplished for the blazed-grating (BG) beamsteering device. The ideal models are those that simulate the phase elements in the FEM environment exactly as they were obtained from the genetic algorithm (GA), that is as individual phase elements that were modeled with periodic boundary conditions (PBC).

PBC repeat the behavior of the unit cell at each applied boundary, and thus a model with PBC simulates a unit cell surrounded at each boundary by an infinite periodicity of identical unit cells. The ideal models did not predict the measurements of the fabricated BG device well, which led to the adoption of a more complex model, the 8-element supercell shown in Figure 7 (a). This model should be the best match for the fabricated device, since here the supercells were surrounded by other supercells, but this model still did not predict the measurements well.

Next the 8-element supercell was kept the same, but this time modeled with perfectly matched layers (PML) as boundary conditions. PML apply a layer at the boundary which absorbs an outgoing wave as it propagates through it, preventing any reflections from interacting with the unit cell, thus isolating it from any effects that are not produced

within the unit cell itself. Although this should not match the conditions of the fabricated device, PML were considered just to see what the device response would be if there was no cell-to-cell interaction. Neither the PBC nor PML supercell models were able to produce results that agreed with measurements and thus another alternative was sought, which was to introduce defects into the models.

The defect study was carried out in two steps, the first sought to study the effect of defects on the individual phase elements, and the second the behavior of the 8-element supercell with the defects. The individual study looked at the effect these defects had on the amplitude and phase imparted by the phase elements for both "global" and "local" defects, which will be further explained later. Once these effects were quantified, the 8-element supercell was modeled with specific defects, and from these, simulated BTDF results were obtained that favorably matched the CASI measurements.

4.2 Comparison between Measured Data and Ideal Models

There was one data set collected with the CASI against which the models could be compared. This data set was collected at the design wavelength of $\lambda = 8\,\mu m$, at four polarization configurations, which were incident horizontal/measured horizontal (H/H), incident horizontal/measured vertical (H/V), incident vertical/measured vertical (V/V), and incident vertical/measured horizontal (V/H). These measurements were accomplished by AFIT student, James Ethridge.

An important note is that the design polarization for the BG device is the incident horizontal polarization. Therefore, the designed mode of operation for these devices is the

H/H polarization. For the purposes of completeness, Figure 16 shows a comparison between the measurements and the ideal model results for all four polarization states, but the rest of the work presented afterward will focus on comparing the measured data to the modeling results only for the input and scattered design polarizations, i.e. H/H. In general the orthogonal V/V polarization always showed good agreement between measurement and model, and for the cross polarizations, H/V and V/H, as agreement between measurement and model improved for the H/H polarization, it also improved for these. The rest of these polarization plots are available for readers to view in Appendix A.

The comparison between the modeled and measured BTDF of the BG device is shown in Figure 16. These BTDF measurements are very accurate. As discussed in Section 3.2, their measurement uncertainty is conservatively <10% for all angles. Since the range of these measurements generally covers 5-6 orders of magnitude and their details are best seen on a log plot, this means any associated uncertainty bars would not even be visible on these plots and have therefore been omitted.

The measured BTDF of the design polarization for the fabricated beamsteerer is shown in Figure 16 (a) and (c), where a majority of the energy, 53%, is in the 0-diffraction order, and only 11% in the designed +1-order, the second highest peak. The remainder of the energy is in the other diffraction orders or in the diffuse scatter. The ideal model (b) and (d), shows the device behaving as a blazed diffraction grating with 89% of the energy deposited in the designed +1-order, and only 4% of the energy in the 0-order. The energy in a diffraction order is calculated here as the area of the full width of a peak between its half maxima. Figure 16 (a) and (b) shows both sets of data in linear space, which allows a comparison of the main peaks; Figure 16 (c) and (d) shows them in log space which shows

the huge dynamic range of a BTDF measurement and the fidelity to which the model simulates all the diffraction orders. Figure 16 also shows the issue at heart of this research, which is the stark disagreement between modeling results and measurement.

The input design and output orthogonal polarization, H/V, is also shown in Figure 16 (a) – (d). The measured data shows peaks that are in reasonably close agreement with the measured H/H polarization, with 49% of the energy in the 0-diffraction order and 14% in the +1-order. The model again shows a different behavior, however; here the ±1-diffraction order peaks have almost equal magnitudes, each with 32% of the energy, whereas the 0-order peak has only 12% of the energy. As mentioned in Chapter II, curvatures in the MPL cavities that were unaccounted for might increase the intensity of the cross-polarized fields measured from the fabricated device, which could lead to the disagreement noted here.

The orthogonal polarization V/V is shown in Figure 16 (e) – (h), where both the model and measurement show a majority of the energy in the 0-diffraction order peak, 97% and 93%, respectively. In the log models, Figure 16 (g) and (h), the ±1- and ±2-diffraction orders are visible, but in all cases the amount of energy in these orders is less than 0.5% for both measurements and models. This indicates, as expected, that there is very little interaction between the orthogonal polarization and the plasmonic decorations.

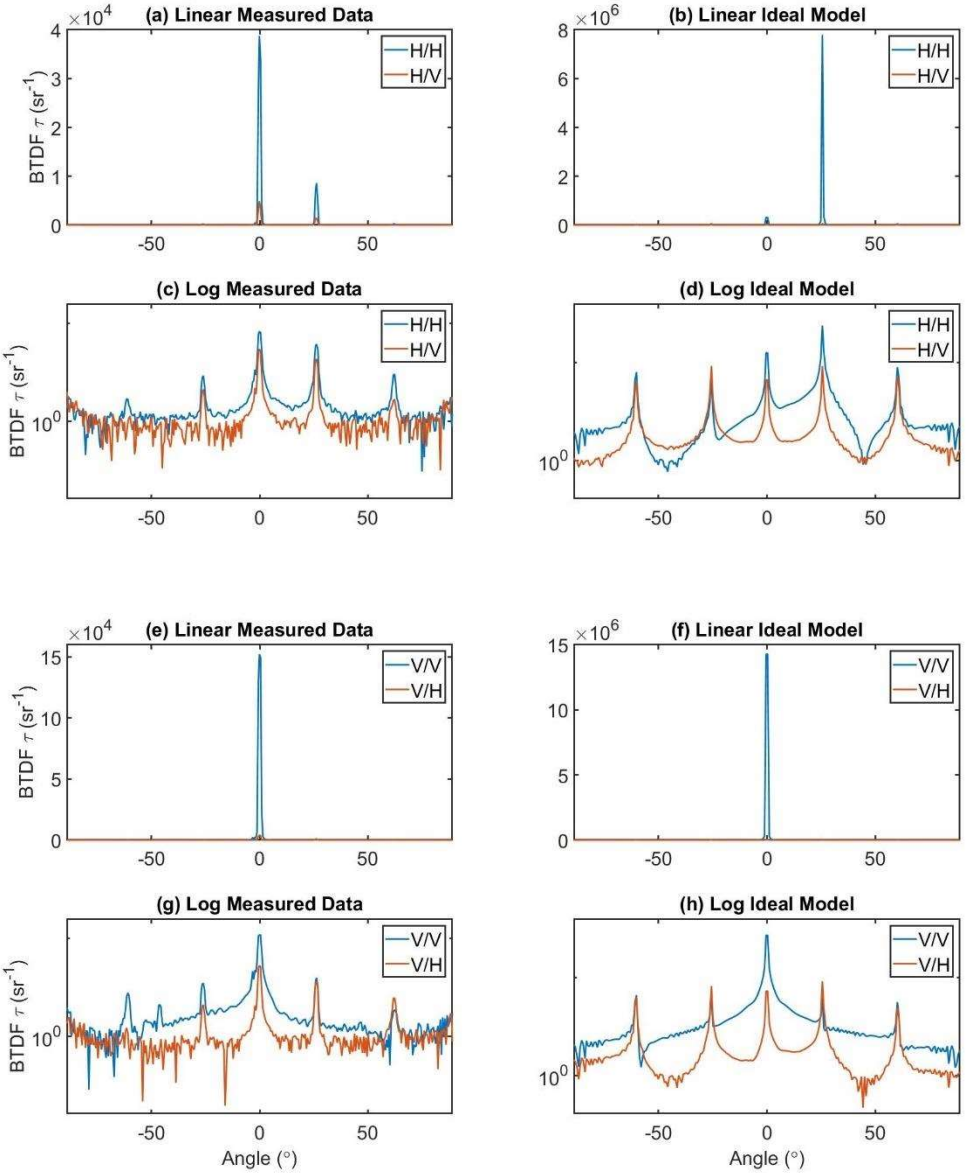

Figure 16. Comparison of BTDF measurement and ideal FEM model of the plasmonic OOP blazed-grating beamsteerer for all four different polarization configurations; results are in ((a), (b), (e), and (f)) linear space and ((c), (d), (g), and (h)) log space. Comparison between the left column, measurement, and the right column, model, shows stark disagreement between the two in terms of which diffraction order has the most energy for the design polarization H/H. As designed in H/H, the model predicts the majority of the energy (89%) in the +1-order, while the measured BTDF shows the majority of the energy (53%) in the 0-order, with only 11% in the designed +1-order. This suggests that the fabricated device works somewhat as designed, but not as well as it should. The log data in ((c), (d), (g), and (h)) shows the huge dynamic range achievable in the BTDF measurement and the fidelity to which the model predicts all the diffraction orders.

The input orthogonal and output design polarization, V/H, is also shown in Figure 16 (e) – (h). Similar to the other cross polarized measurement, H/V, the disagreement between the measurement and modeling results for V/H is stark. In the measured data the 0-diffraction order has 56% of the energy and the +1-diffraction order has 8%. The V/H model on the other hand shows a majority of the energy in the +1-diffraction order with 38%, and the 0- and -1-diffraction orders with 24% and 22% of the energy, respectively. Again, like for the H/V results, disagreement between measurement and modeling could be attributed to defects that increase the intensity of the cross-polarized fields.

Due to the fact that the V/V polarization is typically in good agreement between measurement and model, no other V/V polarization comparison plots will be shown outside the Appendix. Although further plots do not shed light on the issues that this dissertation tries to address, the agreement between measurement and model in the V/V polarization is still a topic that should be briefly discussed.

It is clearly shown that for the design H/H polarization, the model and measurement do not agree, whereas for the V/V polarization they do. This can be explained in terms of the aspect of the decorations with which either polarization interacts. The incident H polarization is designed to interact with the individual phase elements and is thus very sensitive to changes in them. It is hypothesized that any departure in design, as one could expect from the fabricated device, would lead to a departure from the intended behavior, and hence would lead to the measurement and ideal model disagreeing. On the other hand, the incident V polarization interacts orthogonally to the decorations, and thus is not nearly as sensitive to the small changes that would be present in the fabricated device.

In Figure 16, the angle of the +1-diffraction order of the fabricated beamsteerer was consistent with the design but its efficiency was low. As mentioned in the Theory section, the PBC of the designed phase elements were not consistent with the actual fabricated sample due to the proximity of dissimilar elements. This discrepancy was the main motivator in first developing FEM models of the entire supercell and then defect models that attempted to understand the issues that plague the performance of the fabricated device.

4.3 Eight Element Models

Once the ideal models were shown to be insufficient at predicting the behavior of the fabricated device the next level in complexity was to model the entire supercell with PBC. The ideal model simulated the individual unit cells with PBC, and therefore the near fields obtained from these simulations assumed that each unit cell was surrounded by an infinite periodicity of identical copies of itself. In the fabricated device, the phase elements are not surrounded by copies of itself, but rather they follow in the pattern shown in Figure 7 where the *supercell* is surrounded by a finite periodicity of "identical" copies of itself; this led to using PBC, since they would surround the supercells with copies of themselves. But as shown in Figure 17, the result of these models still did not agree with measurements, with 14% and 71% of the energy in the 0- and +1-diffraction order peaks, compared to 53% and 11% for the measurement.

As can be seen from comparing Figures 16 and 17, there are not many differences between the ideal models and the 8-element PBC model, although the 8-element PBC

results do show slightly better agreement with the measurements. The failure of the 8-element PBC model meant further analysis was needed. PBC allow for neighbor-to-neighbor coupling, i.e. responses to near fields not originating in that unit cell. This led to using the same FEM model as shown in Figure 7 (a), but with different boundary conditions, PML. The PML models add a layer around the model which absorb any outgoing waves, isolating a supercell from its neighbors. The result of this model is shown in Figure 18.

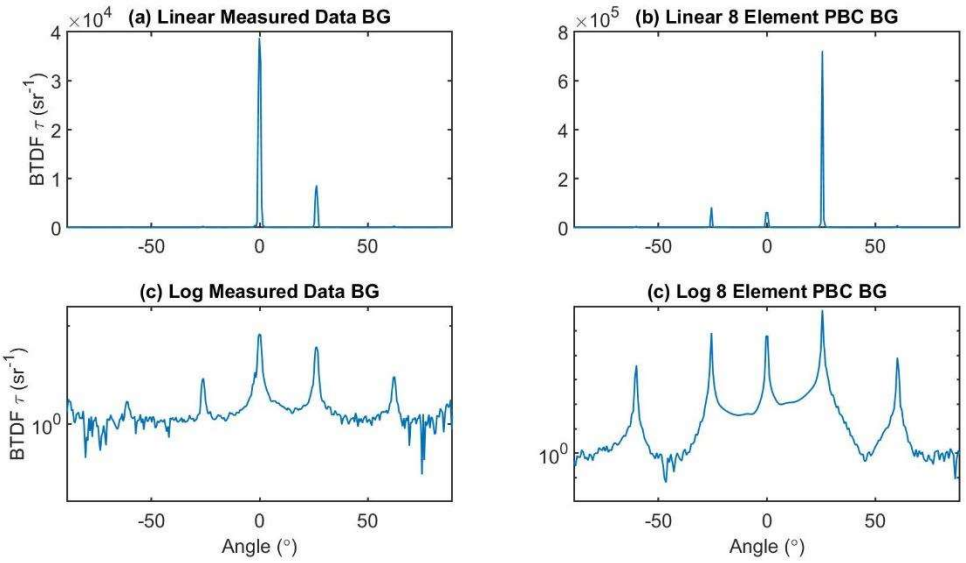

Figure 17. Comparison between measurement ((a) and (c)) to an 8-element FEM PBC model ((b) and (d)) of the blazed-diffraction design. The top row ((a) and (b)) is in linear space, while the bottom row ((c) and (d)) is in log space. In this model 71% of the energy is in the +1-order, (11% in the measurement and 89% in the 1-element model), 14% in the 0-order (53% in the measurement and 4% in the 1-element model). This model shows slightly better agreement with measurement as compared to the ideal model but still fails to accurately predict the measured behavior.

The results obtained from the 8-element PML model once again failed to predict the measurements of the fabricated device, although this time the disagreement between model and measurement was different than that of the PBC models. Both the ideal and

8-element PBC models showed too much beamsteering when compared to the measurement, but the 8-element PML model showed very little beamsteering, in fact, very little, if any, interaction between the incident beam and the device, with the majority of the energy in the 0-order peak, 95% compared to 53% in the measurement, and less than 1% in the designed +1-diffraction order, compared to 11% in the measurement.

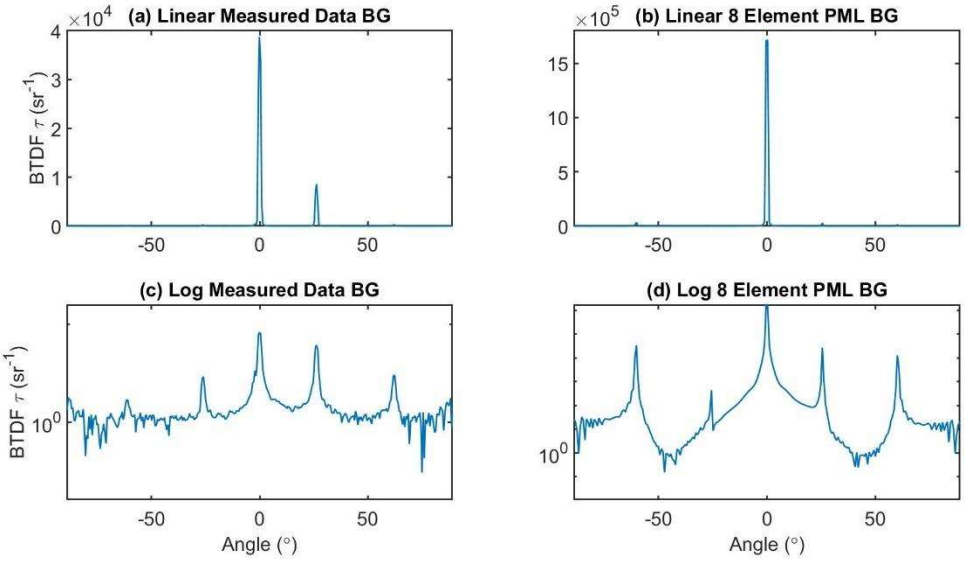

Figure 18. Comparison between measurement ((a) and (c)) to an 8-element FEM PML model ((b) and (d)) of the blazed-diffraction design. The top row ((a) and (b)) is in linear space, while the bottom row((c) and (d)) is in log space. The PML model shows the majority of the energy deposited into the 0-order peak (95% compared to 53% in the measurement), similar to the measured data, but it only shows a very small amount of energy deposited into the +1-order compared to the measurement (0.76% compared to 11% in the measurement).

To further understand the modeled BTDF results, further analysis was accomplished using the near-field data obtained from the ideal and the 8-element PBC and PML models. This analysis consisted of obtaining a reference set of near-field data with empty MPL cavities that had no gold decoration, and using boundary probes instead of point probes to obtain the near fields. Boundary probes calculate the values of a field over a given surface, whereas point probes give the value at a specific point. This undecorated

reference was then compared against the different models to obtain the relative amplitude and phases for the individual phase elements in the different configurations. This undecorated reference was obtained separately for the ideal model, the 8-element PBC model and for the 8-element PML model. Table 1 shows the calculated phases for the eight phase elements that Adomanis designed for use in the BG device.

Table 1. Relative amplitude and phase shift of the eight designed phase elements of the ideal model for the BG device with respect to the empty silicon cavity in the first two rows, respectively. The third row shows the difference between the phase imparted between successive elements. Amp and PD here are shorthand for amplitude and phase difference, respectively.

BG Device	#1	#2	#3	#4	#5	#6	#7	#8
Amp	0.97	0.87	0.96	0.99	0.85	0.90	0.79	0.77
Phase (°)	-80.3	-36.5	1.1	41.1	88.0	141.2	-163.5	-92.4
PD (°)	-43.8	-37.6	-40.0	-47.0	-53.1	-55.3	-71.1	-12.1

Table 1 shows the relative amplitude and phase shift of the individual elements with respect to the undecorated cavity in the first and second rows, respectively, and also shows the phase difference between successive elements in the third row. As mentioned in Chapter II, Adomanis designed eight phase elements to cover the 0-to-2π phase range, with each element having a ±45° phase shift with respect to either the preceding or succeeding phase element. The last row shows that this method extracts phases for these phase elements which are close to the ±45° phase difference between successive elements that Adomanis' GA extracted, with the exception of #7 and #8; the root mean square (RMS) of the phase difference between all phase elements is 47.7°. The RMS value is used instead of the mean because for a majority of the models the mean, which averages the difference between the eight elements, results in a value of 0.

This same method was applied to the data obtained for the 8-element PBC and PML models. Table 2 shows the relative amplitude and phase shift of the individual cells in the supercell for both the 8-element PBC and PML models in the first four rows, and these same values are illustrated in a bar chart in Figure 19. The last two rows show the phase difference between successive cells in both the 8-element PBC and PML models. The RMS phase difference for the PBC case is 49.5°. The fifth row shows that although there is variance, the phase difference between the adjacent cells in the PBC case is all the same sign. This indicates the phase tilt or "blaze" of the supercell is maintained as shown in Figure 19 (a) and leads to the strong beamsteering of Figure 17 (b) and (d). For the PML, the phase difference is small and does not always have the same sign, as shown in Figure 19 (b), which breaks the blaze and is why no beamsteering is shown in Figure 18 (b) and (d). The RMS phase difference was 4.9° for the PML case.

Table 2. Relative amplitude, phase shift and phase difference of the BG 8-element PBC and PML models with respect to the supercell without any gold decorations. The amplitude and phase are recorded from boundary probes above each of the cells in the supercell. Amp and PD here are shorthand for amplitude and phase difference, respectively.

BG Device	Cell 1	Cell 2	Cell 3	Cell 4	Cell 5	Cell 6	Cell 7	Cell 8
PBC Amp	0.51	1.00	1.15	0.72	0.54	0.67	0.58	0.40
PML Amp	0.68	0.77	0.94	1.08	1.11	1.03	0.89	0.85
PBC (°)	-57.9	-24.6	-7.5	23.8	100.5	148.3	-179.0	-133.4
PML (°)	0.57	-4.8	3.4	8.9	10.8	12.3	9.6	7.1
PBC PD (°)	-33.4	-17.1	-31.3	-76.7	-47.8	-32.6	-45.6	-75.4
PML PD (°)	5.3	-8.2	-5.4	-1.9	-1.4	2.6	2.5	6.5

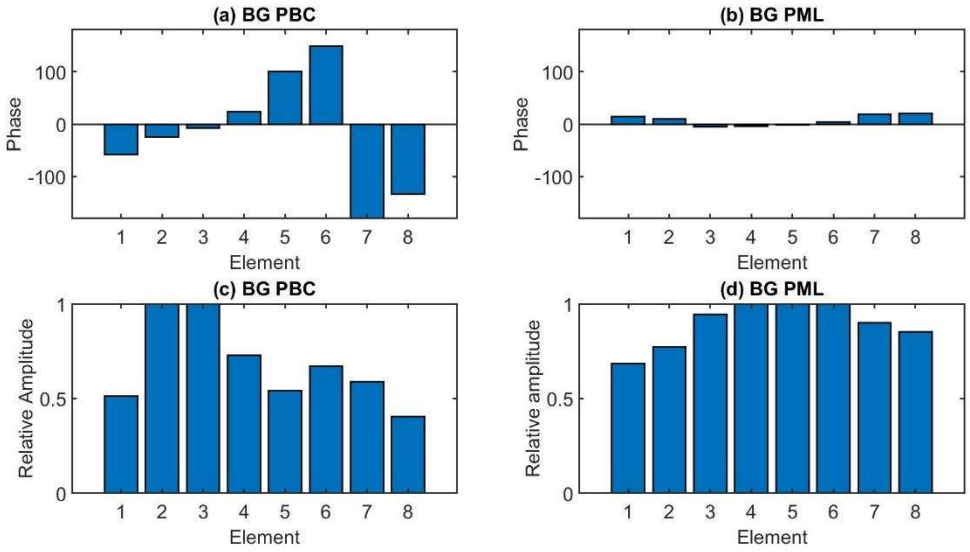

Figure 19. Bar charts depicting both the phase, (a) and (b), and amplitude, (c) and (d) imparted by each cell in the 8-element PBC, (a) and (c), and 8-element PML, (b) and (d), models. The phase plot shows a consistent phase difference between adjacent cells which explains why the 8-element PBC model works so well as a beamsteerer, whereas the 8-element PML model shows very little difference in phase between cells, which explains why it does not work as a beamsteerer.

Thus far, the attempted models, which modeled the device as fabricated and only adjusted boundary conditions, have failed to produce results that matched those obtained from the measurements. But they do provide an indication that there must be something affecting the amplitudes and phases imparted by the individual phase elements in the fabricated device that these models have failed to capture. These were assumed to be defects observed in scanning electron microscope (SEM) images of the fabricated device.

4.4 Defect Models

The defects were studied by the same FEM methodology that had been used up to this point. FEM modeling was accomplished which introduced two types of defects into

the individual phase elements and analyzed their effects on device performance. The defects studied were chosen since SEM images of the fabricated device indicated they could be present (Figure 20 (a)). The first type of defect can be seen as the gold (Au) plasmonic decoration wraps from the intended sidewall of the MPL cavity onto the top of the wall, or from one sidewall of the MPL cavity onto an adjacent wall. The defects are modeled here as vertical and lateral displacements of the plasmonic decoration, and are referred to as "global" defects, since all phase elements will have the same displacement applied. The rationale for this is that these defects could be produced by the general orientation of the metal deposition in the fabrication process, and therefore it is unlikely for any individual phase element to have a displacement independent of its neighbors.

Figure 20 (c) shows a vertical displacement of the "ideal" phase elements in (b), where some of the plasmonic decoration wraps from the sidewall of the MPL cavity onto the top of the wall. (d) shows a lateral displacement of the vertically displaced elements from (c), where some of the plasmonic decoration now wraps from one sidewall of the MPL cavity onto the adjacent wall.

The amplitude and phase changes induced by the defective phase elements were calculated from the near electric fields in the FEM model obtained at a distance half a wavelength above the element. The global defects were studied for four different displacements in each of the x- and z-directions, $\Delta x = 0$, 0.2, 0.4 and 0.6μm, and $\Delta z = 0$, 0.2, 0.4 and 0.6μm (note that the MPL cavity is 2.3μm on a side). If the decoration intersected with the top or sidewall of the MPL cavity, the gold would be deposited on the top or onto the sidewall. The OOP elements were originally designed with a gold thickness

of 150 nm, but due to aperture clogging in MPL fabrication, the thickness was reduced to 100 nm.

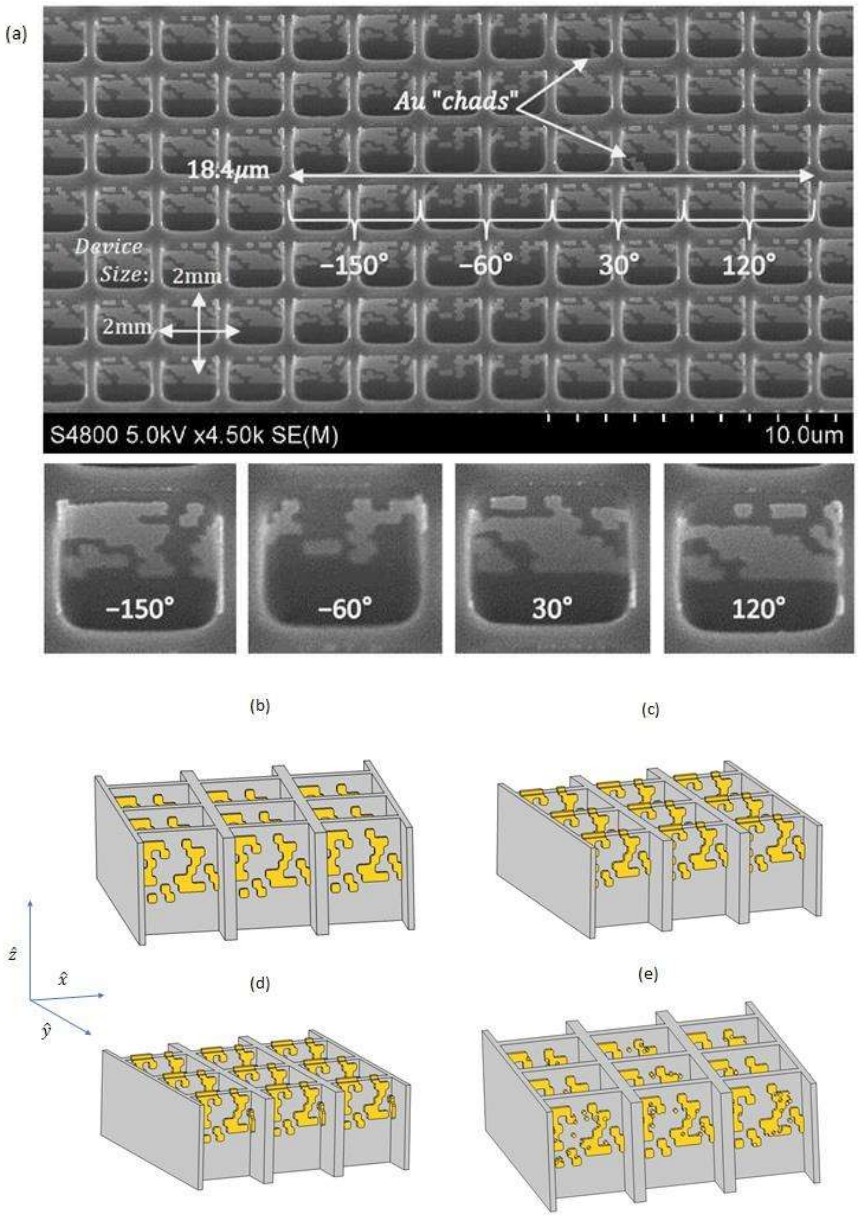

Figure 20. Defects in the phase elements. (a) SEM image of the fabricated device where several "defects" are noticeable. The top image shows "Au chads," which are extraneous gold deposits not part of the original design. Both the top and bottom images also show that the plasmonic Au decorations wrap both from the intended MPL sidewall to the adjacent walls and onto the top of the wall. (b)-(e) Modeled phase elements with these defects. (c) and (d) represent "global" defects to the ideal elements depicted in (b). (c) shows a vertical displacement, where part of the Au decoration is deposited onto the top of the sidewall. (d) shows both vertical and horizontal displacements, where part of the Au decoration is now also wrapped onto the adjacent sidewall. (e) represents "local" defects, where the ideal phase elements from (b) have Au blocks added to or subtracted from the decoration individually.

A total of 16 global-defect configurations was considered. The elements with displacements of $\Delta x = \Delta z = 0$ were considered ideal, and the amplitudes of the defected phase elements were normalized by the amplitude of this ideal phase element to present results as relative amplitudes.

The second type of defect is denoted in Figure 20 (a) as "Au chads." These are gold deposits not intended in the original design. Figure 20 (e) shows the modeled random addition and subtraction of material to/from the gold decorations, which is referred to here as a "local" defect. The local defects were unique and randomized for each phase element, with the rationale being that these defects could be attributed to defects on the MPL mask generating the phase element or other randomness in the process.

Due to the differing nature of the two types of defects, the global defects were modeled with PBC, and the local defects with PML. Figure 21 shows specific values of the differences in phase shift and relative amplitude for the global defects for eight different cases, again ((a) and (c)) $\Delta z = 0$, 0.2, 0.4 and 0.6 μm with $\Delta x = 0$, and ((b) and (d)) $\Delta x = 0$, 0.2, 0.4 and 0.6 μm with $\Delta z = 0$. Table 3 shows the standard deviations of the means of both the relative amplitudes and phase changes calculated for the 10 runs of the local defects to quantify the variation that these defects produce. Figure 21 shows that the horizontal displacement ((b) and (d)) affects the performance of both the phase shift and relative amplitude to a much greater degree than the vertical displacement ((a) and (c)) does. The largest phase shift and relative amplitude changes seen in the vertical displacement are less than 100° and 60% respectively, whereas for the horizontal displacement, these same values have changes almost as large as 200° and close to 100%. Furthermore, when comparing the phase shift and amplitude changes of global defects

shown in Figure 18 to the standard deviations of these from local defects as shown in Table 3, it is clear that the global defects affect both of these values to a much greater extent than the local defects do.

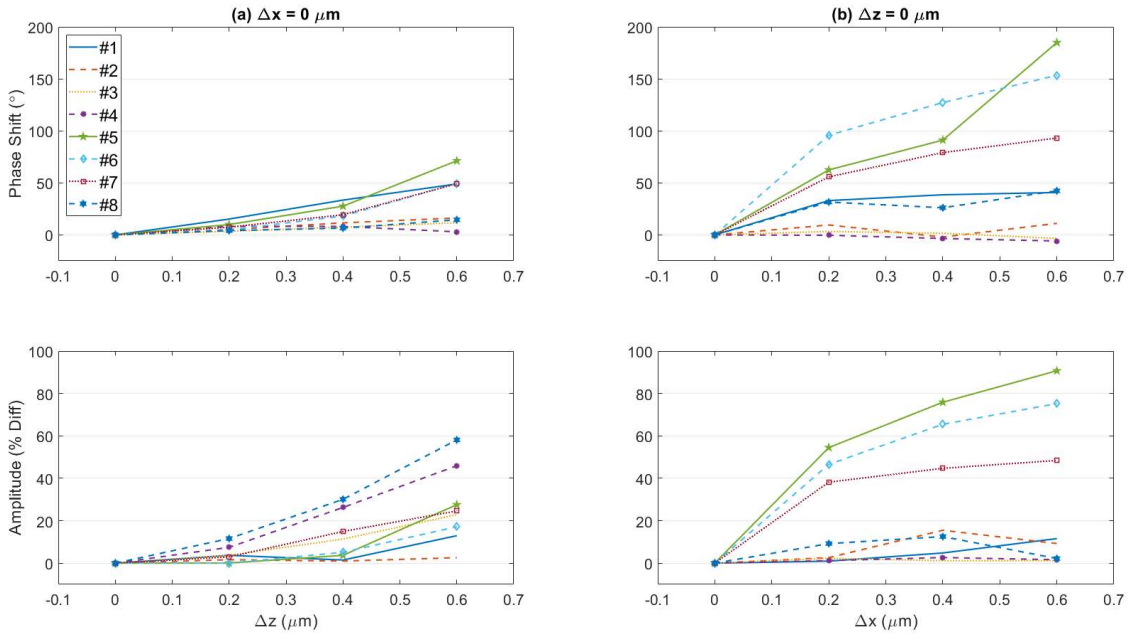

Figure 21. Plots showing global phase shift ((a) and (b)) and amplitude ((c) and (d)) errors for all eight designed elements (#1 - #8). (a) and (c) show both the change in phase shift and amplitude percent difference as the phase element is shifted along the +z direction from Δz = 0, 0.2, 0.4 and 0.6 μm with no x displacement, whereas (b) and (d) shows the same changes while the phase element is shifted along the +x direction from Δx = 0, 0.2, 0.4 and 0.6μm with no z displacement.

From Table 3 it is clear that the impact of local defects does not seem to vary much by element, where most phase shift standard deviations are less than 1°, save for one case, and where all amplitude standard deviations are less than 4%, but that is not the case for the global defects. It may be clearly seen in Figure 21 that while some elements, like #2, #3 and #4, tend to stay near a phase shift change of zero degrees, the rest of the elements are more susceptible to displacements, specifically those along $\hat{x}$, the horizontal direction.

Table 3. Standard deviation of the errors introduced into the phase shift and amplitude for each element for the local defects.

Elements	Phase Shift Std. Dev. (°)	Amplitude Std. Dev. % Diff
#1	0.77	0.70
#2	0.27	0.40
#3	0.80	1.99
#4	2.17	1.64
#5	0.84	3.43
#6	0.58	1.51
#7	0.74	0.91
#8	0.31	0.82

These defects clearly affect phase-element performance; therefore, their overall effect on beam-steering device performance was also considered. Note that only elements #1, #3, #5 and #7 were used in the fabricated device, and recall they were designed to all have similar amplitudes and phase shifts of 90° relative to the successive element. Three of these four were shown to be very susceptible to horizontal shifts in terms of their amplitude and phase shift. FEM modeling was again accomplished using each of the described defects to see how they affect the simulated BTDF. The only defected BTDF simulation that resulted in device performance similar to that measured was an x-displacement, or horizontal, defect, the result of which is shown in Figure 22.

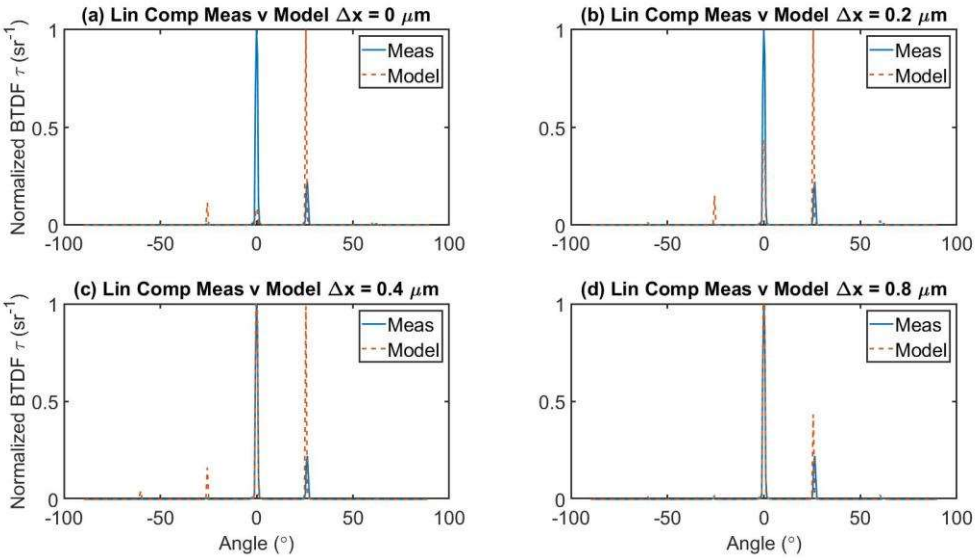

Figure 22. Comparison of lateral displacement modeling to measurement results. As the +x-displacement of the phase elements increases, energy is shifted from the designed +1-diffraction order to the 0-order, emulating the measured device performance. (a)Δx = 0, the simulated relative energy in the +1-order is 71%, compared to 11% measured, and in the 0-order is 14% simulated, compared to 53% measured. (b) Δx = 0.2 μm, 45% and 37% simulated in the +1-and 0-orders, respectively. (c) Δx = 0.4 μm, 29% and 56%, and (d) Δx = 0.8 μm, 16% and 72%. In all models the 0-order peak is wider than the +1-order peak, which in part accounts for the higher energy measured in the 0-order peak for the four studied cases.

As the x-displacement increases, energy is shifted from the designed +1-diffraction-order to the 0-order. Again, the relative energies in the +1- and 0-orders for the nondisplaced, Δx = 0, case (Figures 22 (a)) were 71% and 14%, respectively. The relative energies in these orders for the lateral-displacement cases are now (Figure 22 (b)) 45% and 37% for Δx = 0.2μm, (c) 29% and 56% for Δx = 0.4μm, and (d) 16% and 72% for Δx = 0.8 μm. Again, this is compared to 11% and 53% for the measurement.

X-displacement both decreases the gold in the decoration on the design back wall and increases it on the adjacent sidewall. Separate studies were accomplished that only decreased the gold on the design wall or increased it on the adjacent sidewall. It was found that decreasing the gold on the design wall by itself led to similar results to those shown in

Figure 22, whereas only increasing the gold decoration on the side walls did not produce similar results. Figure 23 shows the simulated BTDF of another x-displacement study, but without adding any gold decorations on the side walls.

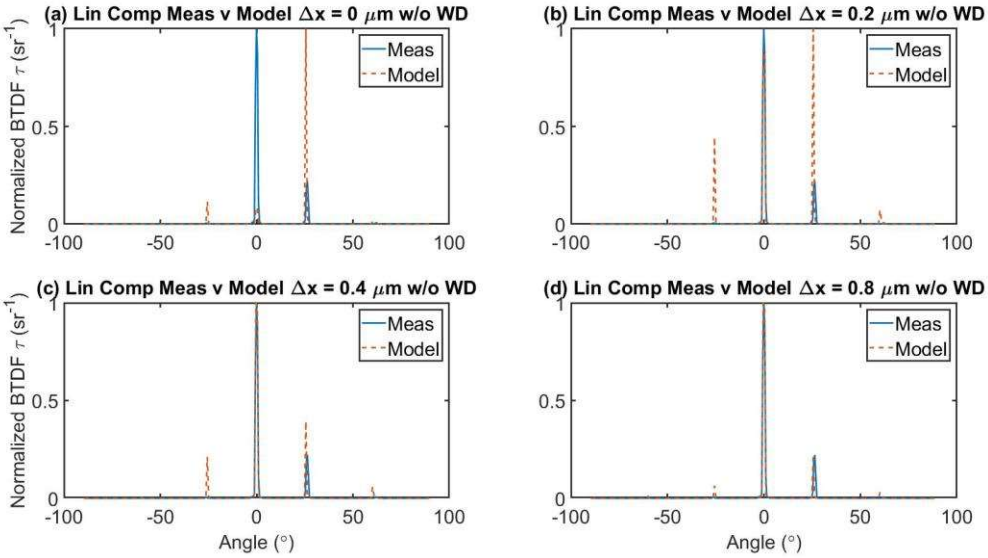

Figure 23. Comparison of lateral displacement modeling to measurement results, with no added gold decorations on the side wall. The shorthand notation "w/o WD" is short for "without wall decoration". As the +x-displacement of the phase elements increases, energy is shifted from the designed +1-diffraction order to the 0-order, emulating the measured device performance. (a)Δx = 0, the simulated relative energy in the +1-order is 71%, compared to 11% measured, and in the 0-order is 14% simulated, compared to 53% measured. (b) Δx = 0.2 μm, 28% and 48% simulated in the +1-and 0-orders, respectively. (c) Δx = 0.4 μm, 13% and 67%, and (d) Δx = 0.8 μm, 9% and 78%. In all models the 0-order peak is wider than the +1-order peak, which in part accounts for the higher energy measured in the 0-order peak for the four studied cases.

Similar to Figure 22, Figure 23 shows that as the lateral displacement increases, so does the energy that is directed away from the designed +1-order to the 0-order. The relative energies in the +1- and 0-order peaks for the lateral-displacement cases of Figure 23 are (b) 28% and 48%, respectively, for Δx = 0.2μm, (c) 13% and 67% for Δx = 0.4μm, and (d) 9% and 78% for Δx = 0.8μm. Again, the only difference between the elements

studied in Figures 22 and 23 is that as the lateral displacement increases in the model in Figure 23, no gold is deposited on the adjacent side wall.

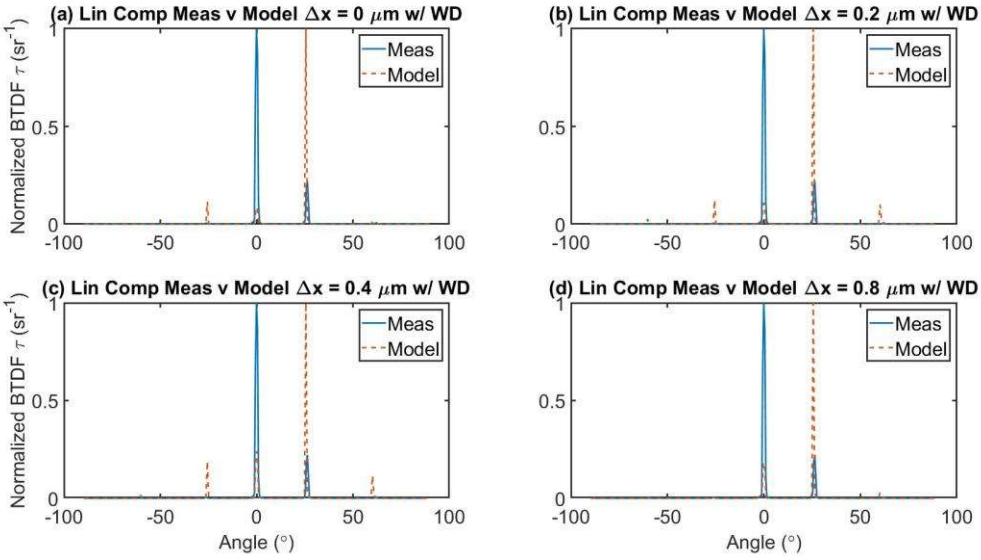

Figure 24. Comparison of lateral displacement modeling to measurement results, where the lateral displacements only affect added gold decorations on the side wall. The shorthand notation "w/ WD" is short for "with wall decoration". As the +x-displacement of the phase elements increases, energy is shifted from the designed +1-diffraction order to the 0-order, emulating the measured device performance. (a)Δx = 0, the simulated relative energy in the +1-order is 71%, compared to 11% measured, and in the 0-order is 14% simulated, compared to 53% measured. (b) Δx = 0.2 μm, 61% and 12% simulated in the +1-and 0-orders, respectively. (c) Δx = 0.4 μm, 50% and 23%, and (d) Δx = 0.8 μm, 65% and 22%. In all models the 0-order peak is wider than the +1-order peak, which in part accounts for the higher energy measured in the 0-order peak for the four studied cases.

For completeness, in the next study, the central gold decoration is not displaced as the now notional lateral displacement increases, but an increasing amount of gold is still deposited on the adjacent side wall. Figure 24 shows that unlike the results shown in Figures 22 and 23, the addition of gold decorations on the side walls by itself is not enough to shift the energy from the +1-order to the 0-order. The added gold on the side wall does change the behavior of the device, but it does not change that the designed +1-diffraction order peak is larger when compared to all other peaks. The relative energies in the +1- and

0-diffraction order peaks for the sidewall gold deposition cases of Figure 24 are (b) 61% and 12%, respectively, for $\Delta x = 0.2\mu m$, (c) 50% and 23% for $\Delta x = 0.4\mu m$, and (d) 65% and 22% for $\Delta x = 0.8\mu m$.

The results shown in Figures 22 - 24 lead to the conclusion that the global defect of x-displacement of the gold decorations in the fabricated device is a likely contributor to the measured fabricated-device performance. While it is interesting to note that the model in Figure 23 shows that removing part of the phase element is enough to shift the energy away from the +1-diffraction order, it is important to reconcile this with the fabricated device. If part of the gold in the phase element in not being deposited on the back wall, it would have to end up elsewhere and there are only so many alternatives. The first scenario is that the gold is deposited on the adjacent sidewall, which is what Figure 22 models. A second scenario could be that gold is deposited on the top of the wall. Simulated BTDF results from this scenario were not shown here, but it was shown in Figure 21 that vertical displacement does not affect the performance of the individual phase elements as much as lateral displacement. A final scenario would be the removal of gold from every phase element, which would be similar to the local defect studied but extended over the entire device to make it a global defect. This would require a repeated defect be present in the mask, which in discussion with the fabrication researchers at SNL, is highly unlikely. The models shown in Figures 21 and 22 are the first to attempt to directly model defects in plasmonic optical metasurfaces, and they produced good agreement with measurements of fabricated devices.

4.5 Measurements, Ideal Models and Defect Study Summary

The measurements of the fabricated blazed-grating beamsteerer device showed strong 0-order diffraction that was not present in the original device simulations, along with weaker designed +1-order diffraction. Additional targeted FEM modeling revealed that this disagreement between measured and designed performance could be attributed to defects observed in the fabricated device. This defect study found that global defects, or defects such as a displacement of the plasmonic decoration within the MPL cavity where all phase elements suffer the same effect, more significantly affect the overall device performance than local, individualized defects. Among the global defects, a lateral displacement was found to best reproduce measured results in simulation.

V. Adjusted Models for Blazed-Grating Device

5.1 Introduction

A second approach to analyzing the fabricated metasurface beamsteering device's performance as observed in the measurements was undertaken in order obtain models that better explained the measured performance of the measured data. These relied on a different approach than that taken by the defect models of Chapter IV by not addressing the defects directly. Rather, the differences between the measurements and the modeling results were studied to see what could be learned from their comparison. This approach focused on the *effects* of potential defects without specifically modeling the defects themselves.

The first observation made when comparing the measured data to the periodic boundary conditions (PBC) models was that the defects shifted energy away from the designed +1-diffraction order into the 0-order. Comparison of measured data to the perfectly matched layer (PML) model showed that the PML model put the majority of the energy in the 0-diffraction order, like the measurement, but the amount of beamsteering it displayed, i.e. the amount of energy in the designed +1-order, was far less than that measured and virtually nonexistent. Therefore, it was observed that the measurement results potentially lie somewhere between the PBC and PML modeling results, and I wanted to see if studying this middle ground would yield correct predictions and insight as to what was affecting the device. This middle ground was studied by considering the

coupling between the phase elements, which determines how strongly neighboring phase elements interact with one another and ultimately affects the performance of the device.

5.2 Performance comparison of Blazed-Grating and Phased-Array beamsteerers

The first step in studying this middle ground was to compare the two basic beamsteering device designs, the blazed-grating (BG) and the phased-array (PA). The fabricated PA device will be discussed in detail in Chapter VI, but a direct comparison of the two fabricated designs would not have been useful here since they were designed to function at different wavelengths, and the shapes and sizes of the phase elements were different. Therefore, in order to make a fair comparison between the BG and PA beamsteerers, the phase elements that were originally designed by Adomanis for the BG design were modeled in an FEM environment but arrayed as a PA with PBC, such as the model shown in Figure 8. The near fields were obtained from this model and the simulated BTDF was calculated and compared to the simulated BTDF of the same phase elements arrayed in a BG design. Figure 25 shows this comparison between the two beamsteerer setups.

As shown in Figure 25, the PA directs more energy to the designed +1-diffraction order peak than the BG setup does (96% compared 71%). This is not surprising given that in the PA design, the like elements are oriented along the direction of polarization, whereas in the BG design there is only one like element along the direction of polarization. The PA placement aligns better with the environment in which the phase elements were designed, with PBC on all boundaries, since like elements are only separated by the MPL cavity's

membrane wall in the PA design, whereas in the BG design they are separated by a membrane wall plus the entire width of the MPL cavity. It was hypothesized that the designed phase shift imparted by the phase elements was dependent on coupling among adjacent elements, and these results reinforce that notion. If coupling between adjacent elements was not an issue, one would expect that both beamsteerers behave similarly, but that was not the case.

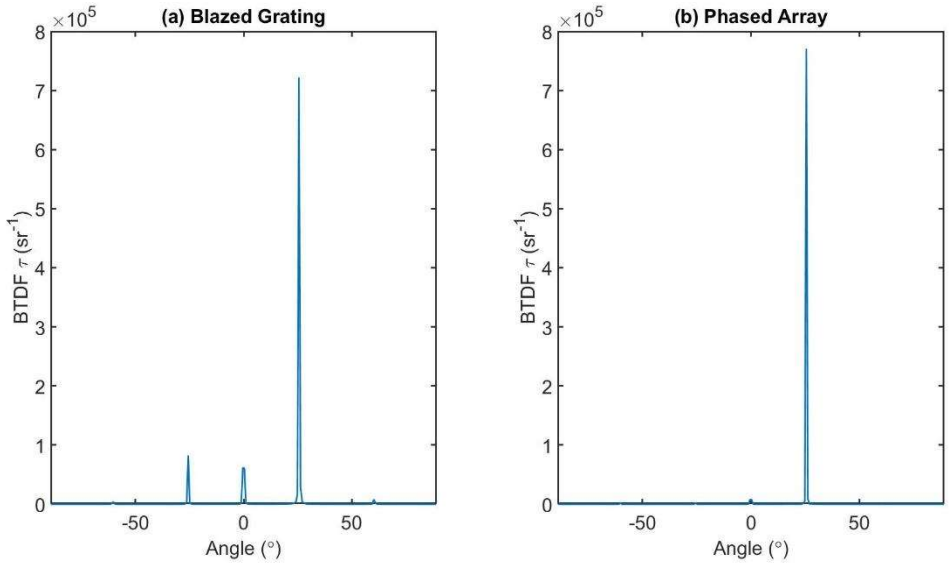

Figure 25. Comparison of simulated BTDF for a blazed-grating (a) and phased-array (b) beamsteerer composed of the same phase elements. The blazed-grating design directs 71% of the energy to the designed +1-diffraction order compared to 96% for the phased-array design. All plots are in linear space.

A phase analysis of the two different setups is shown in Table 4 where the relative amplitude and phase shift of the individual cells in the supercell for both the 8-element BG (same as Table 2) and PA models are shown in the first four rows, and the phase difference between successive cells in both these models in the last two rows. Figure 26 illustrates the phase and amplitude of each cell in the BG and PA designs. Figure 26 (a) and (b) and the

last two rows of Table 4 show that the phase difference between adjacent elements is more stable for the PA design than it is for the BG design. As mentioned previously the RMS phase difference for the BG design is 49.5°, while it is 46.0° for the PA design. On the other hand, the standard deviation of the phase difference is 22.0° and 9.9° for the BG and PA designs, respectively. The amplitude of the PA design is also consistently higher across the cells as shown in Figure 26 (d), which coupled with the more stable phase difference for the PA design leads to a more efficient beamsteerer as shown in Figure 25.

Table 4. Relative amplitude, phase shift and phase difference of the 8-element BG and PA models with respect to the supercell without any gold decorations for the Adomanis designed phase elements. The phase is recorded for boundary probes above each of the cells in the supercell. Amp and PD here is shorthand for amplitude and phase difference, respectively.

	Cell 1	Cell 2	Cell 3	Cell 4	Cell 5	Cell 6	Cell 7	Cell 8
BG Amp	0.51	1.00	1.15	0.72	0.54	0.67	0.58	0.40
PA Amp	0.83	0.99	0.96	0.88	0.83	0.68	0.86	0.90
BG (°)	-57.9	-24.6	-7.5	23.8	100.5	148.3	-179.0	-133.4
PA (°)	-88.6	-50.5	-17.8	27.2	74.1	132.9	-169.0	-134.4
BG PD (°)	-33.4	-17.1	-31.3	-76.7	-47.8	-32.6	-45.6	-75.4
PA PD (°)	-38.0	-32.7	-44.9	-46.9	-58.7	-58.0	-34.6	-45.8

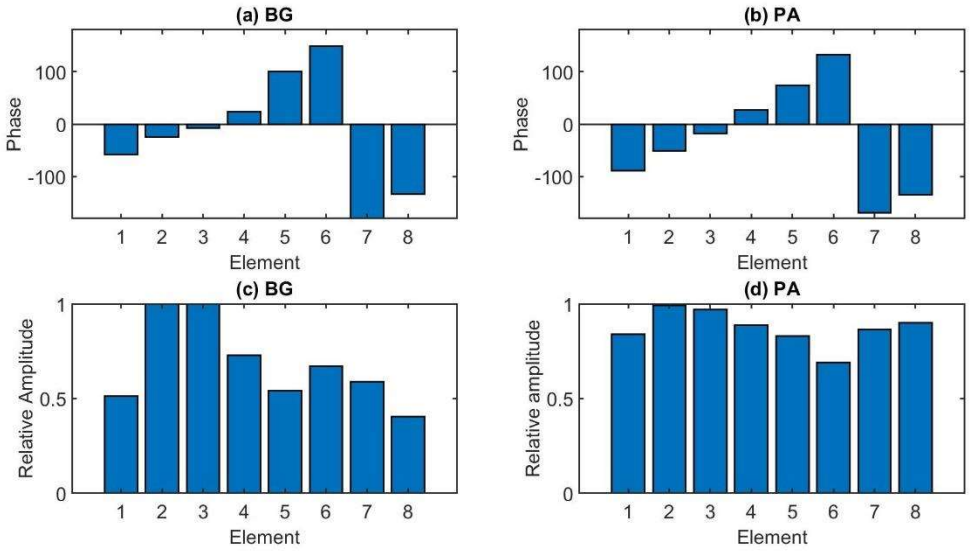

Figure 26. Bar charts depicting both the phase, (a) and (b), and amplitude, (c) and (d) imparted by each cell in the blazed-grating model, (a) and (c), and phased-array model, (b) and (d), with the same phase elements. The phase plot here shows that both have a consistent blaze, but the PA design has less variance with a standard deviation of 9.9° compared 22° for the BG design, and the PA design also has a higher mean amplitude that the BG design, which could help explain why the PA design is much more effective at beamsteering.

5.3 Adjusted Coupling Models

From the previous results, the impact of coupling on the behavior of the beamsteerer was observed, and thus it was decided to further study coupling to see if better agreement between measurement and model could be achieved. In Figure 25 both models still showed a significantly higher designed +1-diffraction order peak than any other peak, but the reduction in coupling seen from the PA to the BG model trends in the right direction that is observed in the measurements.

The 8-element PML model could be thought of as one extreme of the coupling spectrum, which is no coupling at all. Here the 8-element supercell is isolated from any outside effects, and thus the only coupling expected would be between elements in the

supercell interacting with one another. The 8-element PBC model on the other hand could be thought of as the other extreme; i.e. it is completely coupled. Here the PBC boundaries surround the modeled supercell with a periodicity of identical copies of itself and thus every phase element in the supercell interacts with elements within its own supercell, and with elements outside of it. The measured data appeared to be between these two extremes, and thus a model that adjusted coupling was undertaken in an attempt to understand what could be causing this measured performance. Not only could these adjusted models provide accurate predictions of the performance of the devices, but they could give insight into what effect led to the performance observed in the fabricated device.

The adjusted coupling model was termed the "PBC-extended" model, shown in Figure 27, where the FEM model used for both the (a) single cell and (b) supercell simulations are shown. These models use PBC but add additional space outside either the unit cell or the supercell. This empty space reduces the interactions among the unit cells or supercells being studied from that simulated by the PBC models, which again was perfect coupling, and thus perhaps reduces, but definitely changes, the coupling.

The simulated BTDF of the single-element PBC-extended model is shown in Figure 28 for an added spacing of 0.25 MPL cavity around each phase element. It well predicts every diffraction order in the measured data; now, 89% of the energy is in the 0-order compared to 53% measured, and 7% of the energy is in the +1-order for both the modeled and measured data. The phase analysis for these results is shown in Table 5.

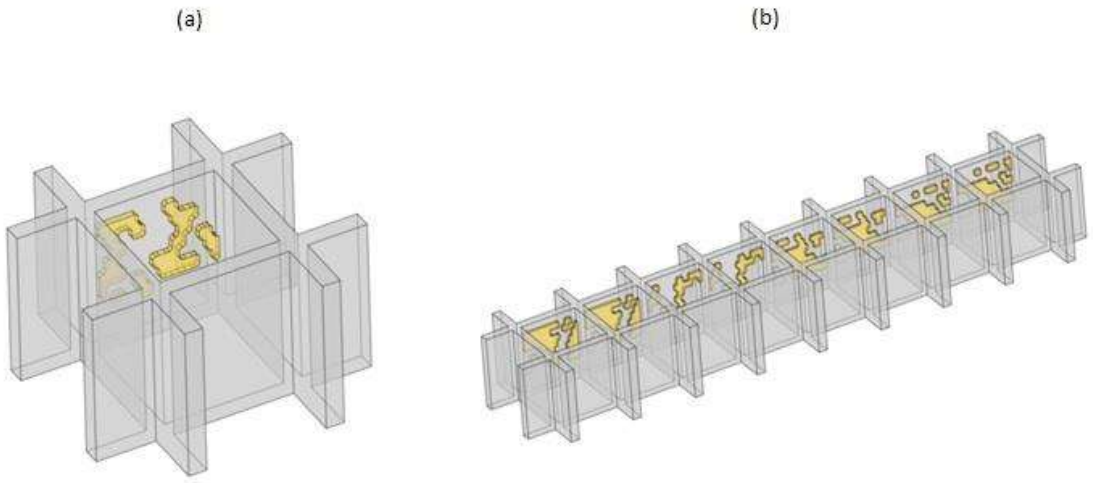

Figure 27. The PBC-extended model. Schematic of FEM modeling space used to obtain the near fields for a (a) single-phase element and for the (b) 8-element supercell. Comparing (b) to Figure 7 (a), additional space is placed around each phase element to reduce its coupling to its nearest neighbors.

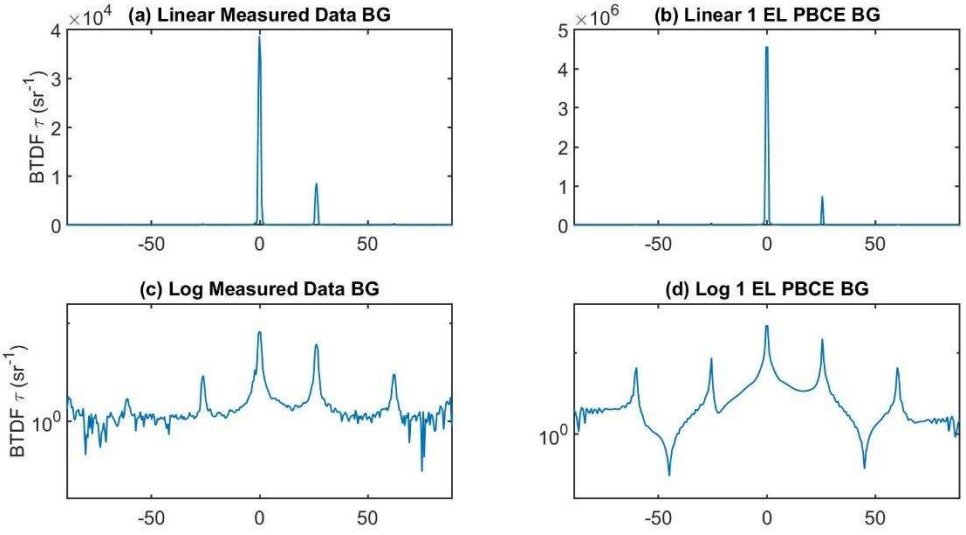

Figure 28. Comparison between measured data, left column, to the simulated one-element FEM blazed-grating design model (Figure 27 (a)) that has added space between repeating elements wtih PBCs. The top row is in linear space, and the bottom in log space. This model accurately predicts the measured data in that it has the 0-order peak the highest (89% energy compared to 53% measured) followed by the +1-order peak (7% energy compared to 11%).

Table 5 again shows the relative amplitude and phase shift of the eight phase elements for the single-element PBC (same as Table 1) and PBC-extended models in the first four rows, and the phase difference between successive phase elements in both these models in the last two rows. Figure 29 illustrates the amplitude and phase of the phase elements that were used to model Figures 16 and 28, which were #1, #3, #5 and #7. Again, the relatively consistent phase difference between successive elements for the PBC case is not repeated for the PBC-extended case, where the phase tilt or blaze of the supercell illustrated in Figure 29 (a) has been significantly reduced by the changed sign of elements #5, #6 and #7. The RMS phase difference of the PBC-extended case is 30.8° compared to 47.7° for the ideal case. Looking at the relative amplitudes of elements #5, #6 and #7, they are significantly lower than those of the first four, which is observed in Figure 29 (d). This may explain why this beamsteerer still steers some of the beam into the designed +1-order in Figure 28, albeit inefficiently.

The simulated BTDF of the 8-element PBC-extended model is shown in Figure 30 for an added spacing of a half cavity around the supercell both along and orthogonal to the polarization direction. This model also does a good job of predicting the diffraction orders of the measured data; predicting 81% of the energy in the 0-order, and 8% in the +1-order. The half-cavity spacing resulted from a study of various sized spacings. Figure 31 shows a comparison of four different values of added cavity spacings, 0.25, 0.5, 1 and 2 MPL cavities, that were modeled for the 8-element FEM model.

Table 5. Relative amplitude, phase shift and phase difference of the eight designed phase elements of the BG device with respect to the empty silicon cavity, and of the same eight elements with 0.25 spacing added around the cavity. The last two rows show the difference between phase imparted between successive elements. Amp and PD are shorthand for amplitude and phase difference, respectively.

BG Device	#1	#2	#3	#4	#5	#6	#7	#8
PBC Amp	0.97	0.87	0.96	0.99	0.85	0.90	0.79	0.77
PBCE Amp	0.72	0.82	0.80	0.83	0.44	0.17	0.48	0.20
PBC (°)	-80.2	-36.4	1.1	41.1	88.0	141.2	-163.4	-92.3
PBCE (°)	-88.2	-63.3	-49.3	-36.7	-18.5	-76.0	-80.2	-122.6
PBC PD (°)	-43.7	-37.6	-39.9	-46.9	-53.1	-55.3	-71.1	-12.1
PBCE PD (°)	-24.8	-14.0	-12.6	-18.2	57.5	4.1	42.4	-34.3

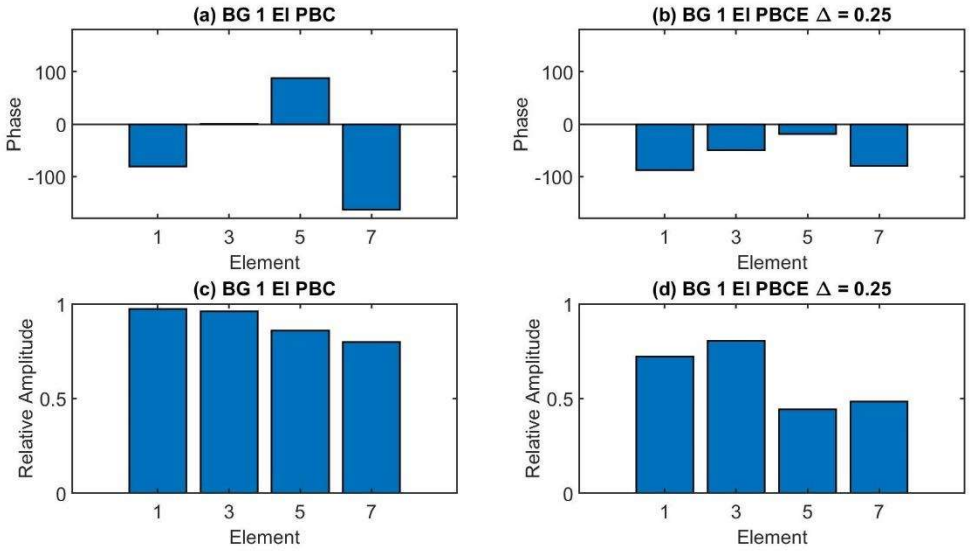

Figure 29. Bar charts depicting both the phase, (a) and (b), and amplitude, (c) and (d) imparted by each cell in the ideal model, (a) and (c), and 1-element PBC-extended model, (b) and (d). Both BTDF models showed in Figures 16 and 28 only used elements 1, 3, 5 and 7 and thus are the only ones shown here. The phase plots show that the ideal model maintains a consistent phase difference, which is not the case for the 1-element PBC extended model, and also maintains a higher mean amplitude than the PBC-extended model.

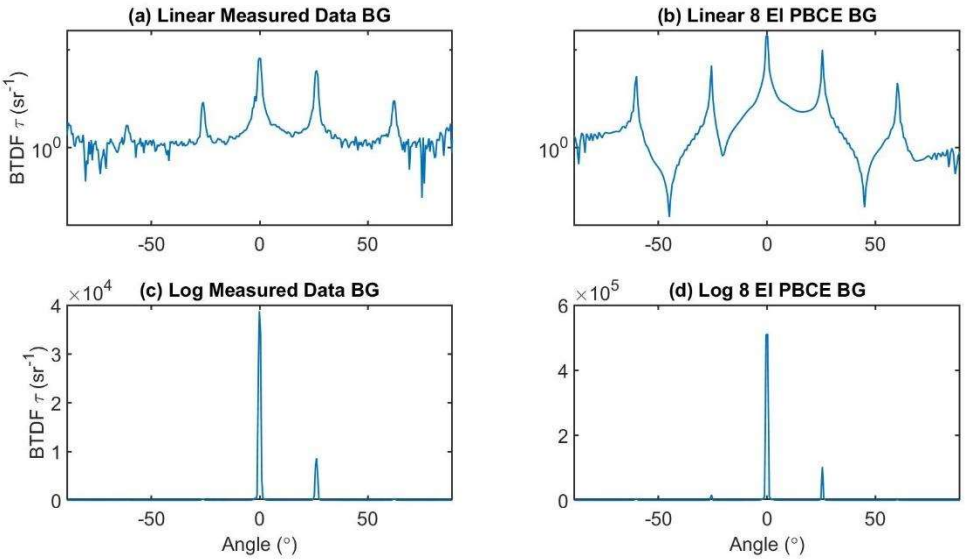

Figure 30. Comparison between measured data, left column, to the simulated 8-element FEM model (Figure 27 (b)) that has added space between repeating supercells wtih PBCs. The top row is in linear space, and the bottom in log space. This model accurately predicts the measured data in that it has the 0-order peak the highest (81% energy compared to 53% measured) followed by the +1-order peak (8% energy compared to 11% measured).

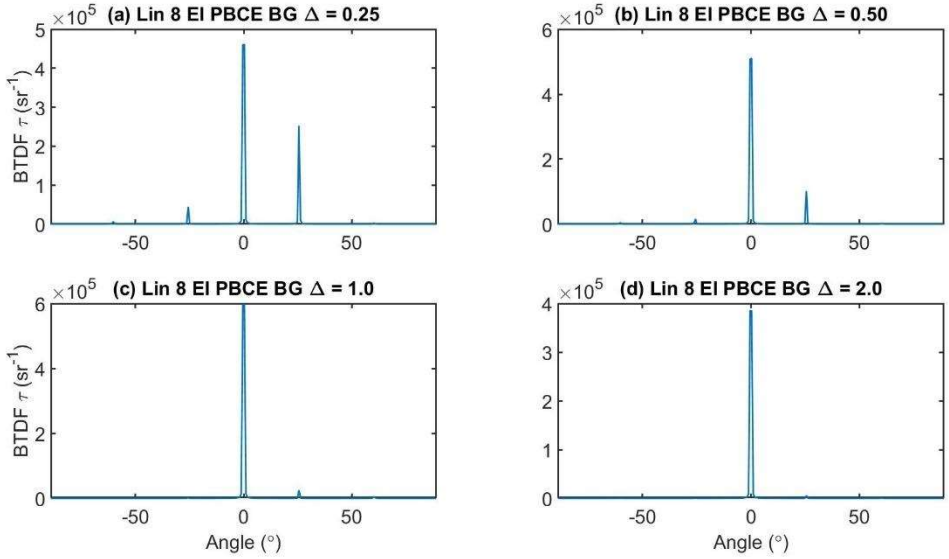

Figure 31. Comparison of modeled BTDF for the BG PBC extended case as the spacing around the supercell is increased from 0.25 (a), 0.5 (b), 1.0 (c), and 2.0 (d). The energy deposited in the 0- and +1-orders for the four cases are, 68% and 19% for 0.25, 81% and 8% for 0.5, 89% and 2% 1.0, and 91% and 1% for 2.0. It can be seen that as the added spacing around the FEM model increases, the amount of energy directed towards the design +1-order peak decreases.

From Figure 31, it is evident that as the spacing increases around the supercell in the FEM model, the amount of energy directed to the designed +1-diffraction order peak decreases, with the energy going to the 0- and +1-order peaks for all four cases being 68% and 19%, respectively, for 0.25 MPL cavity spacing, 81% and 8% for 0.5, 89% and 2% for 1.0, and 91% and 1% for 2.0. Rather than in tabular form, the relative amplitude and phase difference for these results are shown in Figures 32 and 33.

Figure 32 shows the relative amplitude of the individual phase elements with respect to the undecorated cavities for the different spacings used in the PBC, PML and PBC-extended model, and Figure 33 shows the phase differences between the successive phase elements for all these cases. Figure 33 again shows the relatively consistent phase difference between successive elements of the PBC case (same as Table 2) being both lost and reduced in magnitude as spacing in the PBC-extended model is increased, again reducing the phase tilt or blaze of the supercell and explaining the BTDF results of Figure 30. The RMS phase difference values of the different spacings are 32.3°, 17.9°, 9.6° and 5.6°, for $\Delta = 0.25$, 0.5, 1 and 2, respectively. Beamsteering is strongest for the $\Delta = 0.25$ case, apparently because phase elements #2-#5 maintain a relatively consistent phase difference along with strong relative amplitudes; the amplitudes of elements #6-#8 have been reduced.

The results shown in Figures 28 – 33 and Table 5 not only provide a model that is able to accurately predict the performance of the fabricated device, but it also helps give insight into why the fabricated device is not an efficient beamsteerer. Figures 28 and 30 show that the $\Delta = 0.25$ spacing for the one-element PBC extended model and the $\Delta = 0.5$ spacing for the 8-element model, respectively, provide predictions that agree with

measurements, and Table 5 and Figures 32 and 33 give detailed explanations of why that is. It is shown that unlike the ideal and 8-element PBC models, these added-spacing models have an inconsistent blaze that switches sign in elements #5 and #7 in the one-element PBC-extended model, which are in the fabricated device, and in cells 6 and 7 in the 8-element PBC-extended model. It is also shown that the relative amplitudes of the elements of these models are lower than those of the ideal and 8-element PBC models. Thus, from these two models, it can be hypothesized that the fabricated device suffers from an inconsistent blaze resulting from the amplitudes and phase shift imparted by the phase elements being significantly different than what was designed.

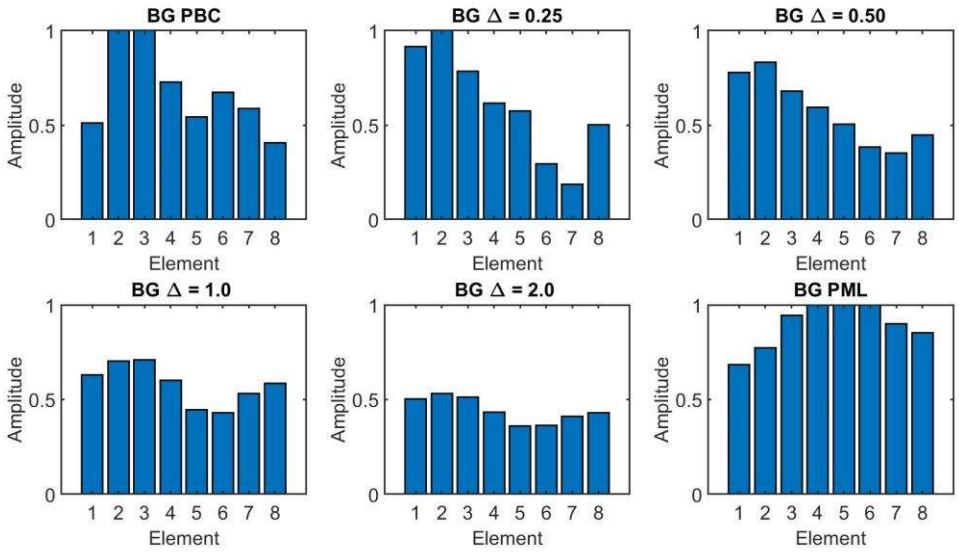

Figure 32. Relative amplitude of the cells for the 8-element FEM models of the BG device. For the models with PBC, it is shown that as the spacing increases, the relative amplitude decreases. This effect could lead to the observed decrease in efficiency in beamsteering that is observed as the spacing increases.

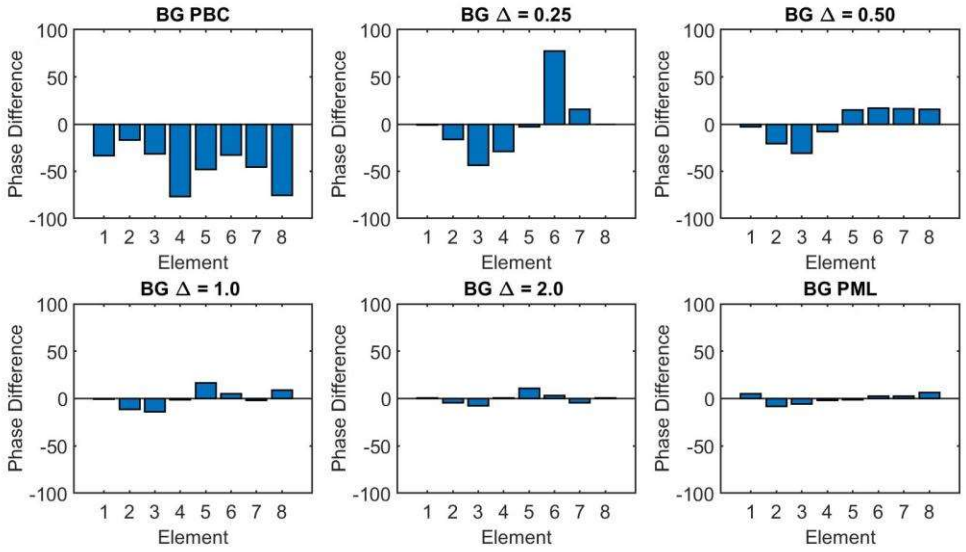

Figure 33. Relative phase difference between adjacent elements for the 8-element FEM models of the BG device. While the PBC case shows a relatively consistent phase difference, the rest of the attempted models show variances that lead to their poor beamsteering efficiencies.

The success of the 1-element PBC-extended model at predicting the measured BTDF results of the fabricated device suggests a potential improvement over the current method employed to design new phase elements. As previously mentioned, currently, the phase elements are designed in a genetic algorithm (GA) where the phase element decorations are iteratively manipulated until those decorations that achieve the desired amplitudes and phase shifts are found. This iteration occurs in an FEM space that is the size of the MPL cavity and is bounded on all sides by PBC. The boundary conditions used in the GA are appropriate for ideal interactions between adjacent phase elements, and thus lead to designed phase elements that are reliant on neighboring identical phase elements in order to achieve the designed amplitude and phase. Perhaps using a PBC-extended-type model in the GA would lead to designed phase elements that are less reliant on having

identical adjacent phase elements to perform as designed, and thus lead to more robust phase elements.

5.4 Adjusted Models Summary

An alternate methodology to produce models that accurately predict the behavior of the fabricated beamsteering devices was explored. This alternate methodology focused on adjusting the coupling between adjacent phase elements in order to obtain more accurate predictions, as opposed to incorporating defects directly into the FEM models as was done in Chapter IV. First, by comparing models of idealized blazed-grating and phased-array devices, it was shown that the coupling between adjacent phase elements noticeably affects the performance of the device, and therefore this effect was studied further.

Two PBC-extended models were studied, which added an additional spacing around either the unit-cell phase element or the 8-element supercell. The 1- and 8-element models directed the majority of the energy to the 0-order (89% and 81%, respectively, compared to 53% measured) followed by the designed +1-order (7% and 8%, respectively, compared to 11% measured), while still maintaining relatively low -1- and ±2 orders, in agreement with measurements.

Phase analysis and comparison of the 8-element PBC-extended model showed that as the spacing increased, the relatively consistent phase difference between the phase elements of the designs which steered the beam efficiently was lost, and the efficiency of the beamsteerer was reduced; this led to the models that well predicted the measurements. These models also provided insight into what effects could be causing the poor

performance of the fabricated beamsteerer as models with an inconsistent phase blaze and reduced or irregular amplitudes among the phase elements of the supercell were those that were able to successfully predict the measured data.

The success of these adjusted models highlights the importance of coupling in these devices. How strongly the adjacent elements interact with one another impacts the performance of the device, and not accounting for this effect can lead to differences between the expected and measured behavior of these devices. Further, the success of the PBC-extended models, specifically the 1-element model, suggests that a slight alteration to the current GA design method could lead to the design of more robust phase elements in the future. Using a PBC-extended-type model in the FEM model in which the GA operates could lead to phase elements that are less reliant on having adjacent like elements in order to perform as designed, and which could improve the performance of the fabricated devices.

VI. Phased-Array Beamsteering Device

6.1 Introduction

Aside from its brief introduction in Chapter 5, the phased-array (PA) beamsteering device has not yet been discussed in detail with regards to its performance, and thus far no models of it have been shown. The reason for this is that the majority of the work that was accomplished for the blazed-grating (BG) device was also accomplished for the PA device, and there are no new methodologies that arise from the study of this fabricated device.

In this chapter, the methods that were previously explored in Chapters IV and V for the BG device were applied to the PA device, and from those, a great deal was learned. Thus far, these methods were shown to either succeed or fail in their ability to predict the performance of the fabricated device, but whether that is due to the method itself or the device being studied is something that could not be addressed with only one device being studied. This additional data set for a different device allows for the effectiveness of these different methods to be better understood.

This chapter will start by discussing results obtained from the ideal and the 8-element PBC and PML models, and how they compared to the measured data obtained from the fabricated PA device. Unlike for the BG device, the PML model for the PA device predicts more beamsteering than what was measured for the fabricated device. Reasons for this difference in performance between the PML models for the two devices will be discussed in that section. Due to the results for the 8-element PML model, a single-element PML model, which was not discussed for the BG device, was also explored for the PA

device to see what it would predict. Those predictions did not display any beamsteering, which provides evidence for the first time that coupling exists between the phase elements *across* the MPL cavities in the 8-element PML model. The last section focused on applying the PBC-extended model to the PA device, both for one- and 8-element devices. These results again illustrate the "reduced coupling" effects that are present in that model.

6.2 Comparison between Measured Data and Ideal Models

There was a total of four different measurement sets collected with the CASI against which the models could be compared for the PA device. These were collected at four different wavelengths, $\lambda =$ 5.5, 6.0, 6.25 and 6.5 μm, at four polarization configurations, incident horizontal/measured horizontal (H/H), incident horizontal/measured vertical (H/V), incident vertical/measured vertical (V/V), and incident vertical/measured horizontal (V/H). The PA design was intended to be a broadband device, which is why it was measured over the $\Delta\lambda = 1\ \mu m$ range centered at $\lambda = 6$ μm, the wavelength at which the PA phase elements were designed. These measurements were accomplished by AFIT student, Matthew Miller.

Similar to the BG device, this device was designed to work with the H/H polarization. Characterization at the four different wavelengths will be shown in Figure 34, where the ideal model and the measurement results are compared, but for the purposes of brevity and clarity, only the design wavelength of $\lambda = 6$ μm and design polarization, H/H, will be shown in the rest of the figures in this chapter. The figures for the other polarizations and wavelengths are shown in Appendix A.

In Figure 34, similar to those of the BG device, the ideal models of the PA device show much more beamsteering than was measured. For all four wavelengths, the ideal model again places the majority of the energy in the designed -1-diffraction order, 71%, 86%, 85% and 90% for λ = 5.5, 6.0, 6.25 and 6.5 μm, respectively, and the second highest peak is the 0-order with 22%, 2%, 3% and 2% of the energy, again respectively for the four wavelengths. This is in contrast with the measurement which had the majority of the energy in the 0-order for all four wavelengths, 31%, 27%, 33% and 27%, again respectively, and the second highest amount in the -1-order for the four wavelengths with 2%, 2%, 1% and 1%, respectively.

From the measurement results shown in Figure 34 (a), (c), (e) and (g), it is hard to see the device is beamsteering as designed, especially due to the fact that in all four cases the amount of energy deposited into the -1-order ranges only from 1-2%. In an effort to show that the device does steer the beam as designed to some extent, Figure 35 shows the measurement data shown in Figure 34 (c) in both linear and log space, but it limits the span of the y-axis in the linear plot, to show that there are differences in magnitude between the ±1-order peaks. The energy in the three peaks are 27%, 2%, and 0.6% for the 0-, -1-, and +1-orders, respectively. The rest of the energy is deposited either in the other orders or in the diffuse scatter. The relative amplitude and phase difference for these results is shown in Table 6.

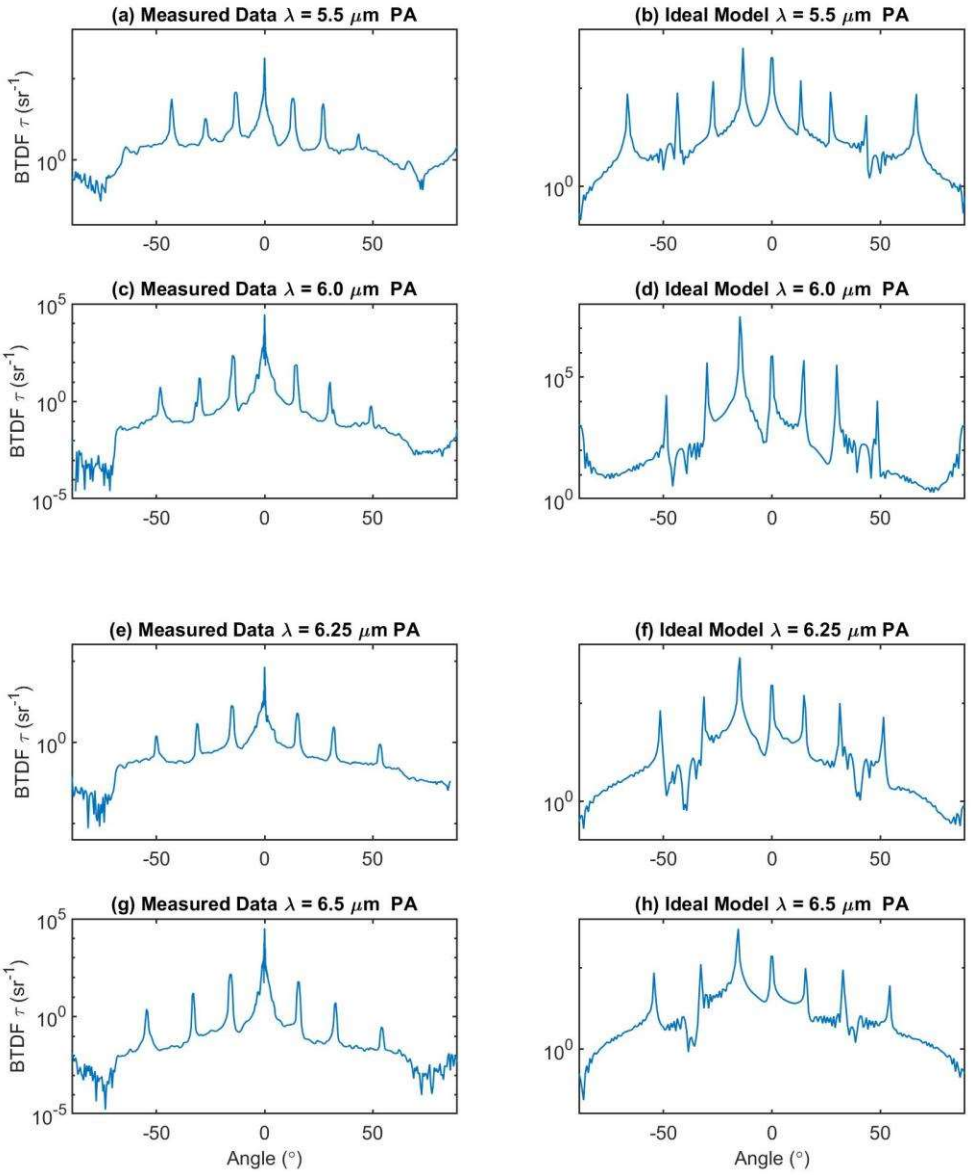

Figure 34. Comparison of BTDF measurement, left column, and ideal FEM model, right column, of the PA beamsteerer in log space. Comparison between the measurement and model shows stark disagreement between the two in terms of which diffraction order has the most energy in all four wavelengths. As designed, the model predicts the majority of the energy, 71%, 86%, 85% and 90%, respectively for λ = 5.5, 6.0, 6.25 and 6.5 μm, in the -1-order, with only 22%, 2%, 3% and 2% in the 0-order again for the four wavelengths. In the measured BTDF the majority of the energy is in the 0-order, with 31%, 27%, 33% and 27% for the four wavelengths and 2%, 2%, 1% and 1% for the four wavelengths in the designed -1-order. The log data shows the huge dynamic range achievable in the BTDF measurement and the fidelity to which the model predicts all the diffraction orders.

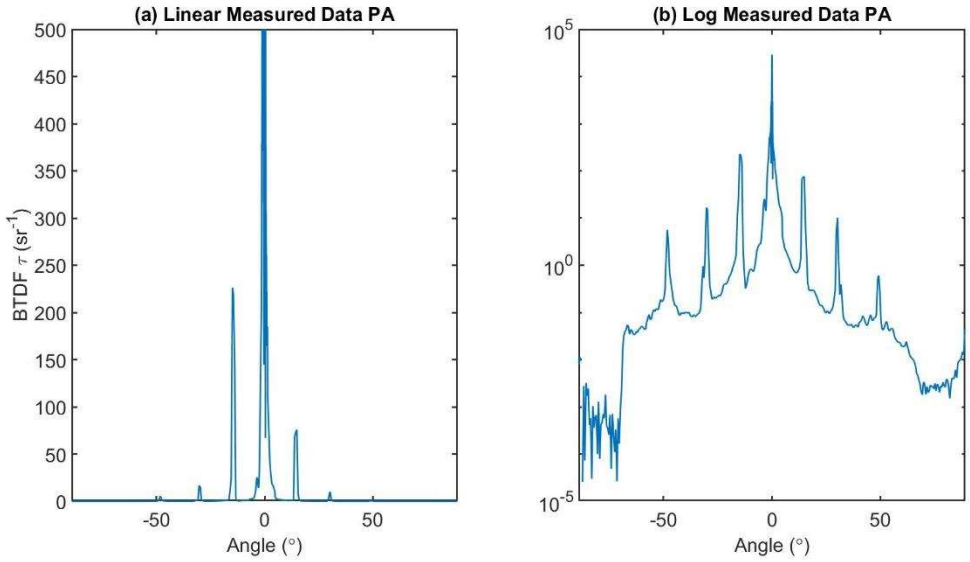

Figure 35. BTDF meaurement of the fabricated device at the design wavelength, for linear space (a), and log space (b). In (a), with the y axis limited, it is easier to see the difference between the -1-order peak, which has 2% of the measured energy, compared to the +1-order peak, which has 0.6% of the measured energy. Although small, this distinction does show that the device does steer the beam.

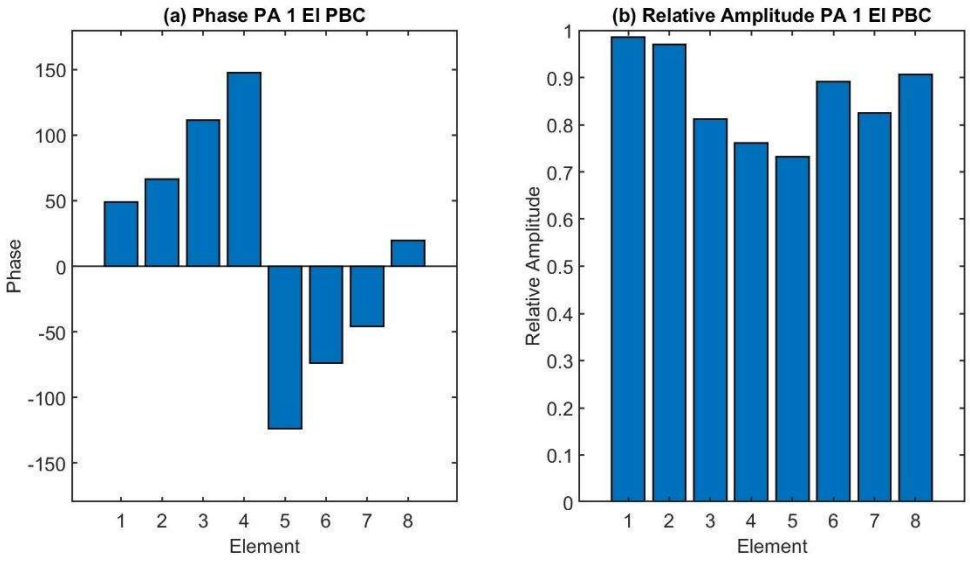

Figure 36. Bar charts depicting both (a) the phase and (b) amplitude imparted by each element in the ideal PA model. The plots show that the ideal model maintains a consistent phase difference and a high relative amplitude which help explain why it is so effective at beamsteering.

Table 6 and Figure 36 again show the relative amplitude and phase shift of the eight phase elements and the phase difference between successive phase elements for the ideal PA model, with an RMS phase difference value of 49.9°. Similar to the BG device, the phase elements here have relatively consistent relative amplitudes and there are relatively consistent phase differences between successive elements, which explains the efficient beamsteering in the ideal models of Figure 34.

Table 6. Relative amplitude and phase shift of the eight designed phase elements of the PA device with respect to the empty silicon cavity in the first and second row, respectively. The last row shows the difference between phase imparted between successive elements. Amp and PD here are shorthand for amplitude and phase difference, respectively.

PA Device	#1	#2	#3	#4	#5	#6	#7	#8
Amp	0.98	0.97	0.81	0.76	0.73	0.89	0.82	0.90
Phase (°)	49.2	66.4	111.6	147.9	-123.8	-73.8	-45.9	19.9
PD (°)	-17.2	-45.2	-36.3	-88.3	-50.0	-27.9	-65.8	-29.3

6.3 Eight Element Models

Similar to the BG device, once the ideal model was shown to be inadequate at predicting measured device performance, alternative models which were more complicated were explored. First are the 8-element supercell models. The 8-element FEM model used for the PA device was shown previously in Figure 8 (a). The result of the 8-element PBC model is shown in Figure 37. The linear plots shown for the measured data in Figures 37

and 38 again have scaled y-axes to help illustrate that the device does steer the beam, although not very effectively.

Like for the BG device, the 8-element PBC model for the PA device does not predict the measured behavior well. Also similar to the BG device, the ideal model directs more energy to the design order, in this case the -1-order (86%), than the 8-element PBC model does (82%), so like with the BG device, the 8-element model agrees slightly better with the measurement, but not by much.

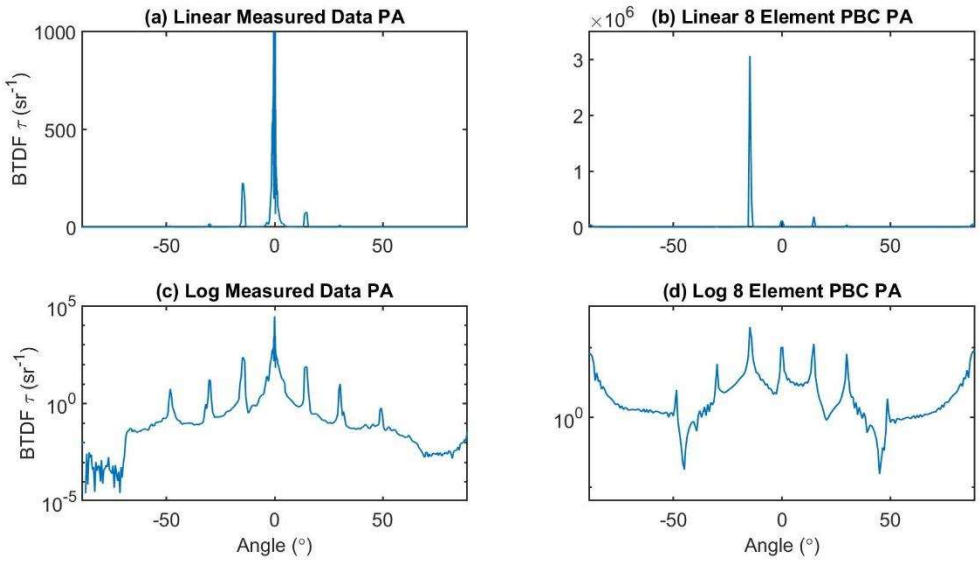

Figure 37. Comparison of BTDF measurement and 8-element PBC model of the PA beamsteerer; results are in ((a) and (b)) linear space and ((c) and (d)) log space. The y-axis in (a) is scaled down to show beamsteering in the measured device. In this model 82% of the energy is in the -1-order, (2% in the measurement and 86% in the 1-element model), 2% in the 0-order (27% in the measurement and 2% in the 1-element model).

The next step was to model the 8-element FEM model with PML. The result of this model is shown in Figure 38, where unlike for the BG device, the PML model for the PA device shows more beamsteering than the measured data, with 21% of the energy in the

designed -1-diffraction order as opposed to the measurement that had only 2% of the energy in the same order. The amount of beamsteering this model predicts is less than that of the 8-element PBC model, yet it is considerable. The relative amplitude and phase analysis for the 8-element PBC and PML models is shown in Table 7 and is illustrated in bar charts in Figure 39.

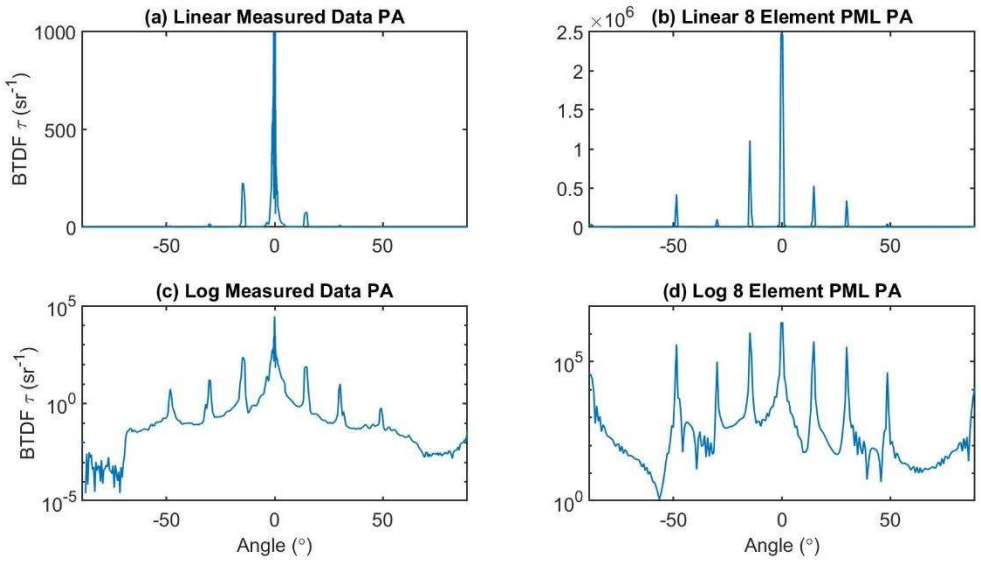

Figure 38. Comparison of BTDF measurement and 8-element PML model of the PA beamsteerer; results are in ((a) and (b)) linear space and ((c) and (d)) log space. The y-axis in (a) is scaled down to show beamsteering in the measured device. The PML model shows the 0-order peak with 44% of the energy compared to 27% in the measurement, and 21% of the energy in -1-order peak compared to 2% for the measurement. This PML model does account for beamsteering, although not as strongly as the PBC model.

Table 7 again shows the relative amplitude and phase shift of the individual cells in the supercell for both the 8-element PBC and PML models for the PA device in the first four rows, and the phase difference between successive cells in both these models in the last two rows. The phase elements have relatively consistent relative amplitudes and there are again relatively consistent phase differences between successive cells in the PBC model

as illustrated in Figure 39 (a), and as there were in the ideal PA model, which explains its efficient beamsteering behavior (Figure 37). On the other hand, there are much-reduced and disparate relative amplitudes among the phase elements of the PML model, and the phase tilt or blaze of the supercell has been significantly reduced by the changing sign of the elements, as illustrated in Figure 39 (b) and (d), which explains the reduced beamsteering and shift of energy to the 0-diffraction order in Figure 38. The PBC and PML models have RMS phase difference values of 50.1° and 118.8°, with standard deviations of 23.7° and 118.3°, respectively.

Table 7. Relative amplitude, phase shift and phase difference of the 8-element PBC and PML PA models fabricated with respect to the supercell without any gold decorations. The phase is recorded for boundary probes above each of the cells in the supercell. Amp and PD here are shorthand for amplitude and phase difference.

PA Device	Cell 1	Cell 2	Cell 3	Cell 4	Cell 5	Cell 6	Cell 7	Cell 8
PBC Amp	1.09	0.99	0.87	0.79	0.43	0.95	0.99	0.66
PML Amp	0.33	0.06	0.32	0.30	0.32	0.20	0.42	1.02
PBC (°)	42.2	67.6	95.9	132.4	-134.9	-80.4	-61.5	-0.2
PML (°)	128.6	-98.4	40.5	7.9	-38.9	-94.6	92.9	-29.1
PBC PD (°)	-25.5	-28.2	-36.5	-92.7	-54.5	-18.9	-61.3	-42.4
PML PD (°)	132.9	-138.9	32.6	46.8	55.7	172.4	122.1	-157.8

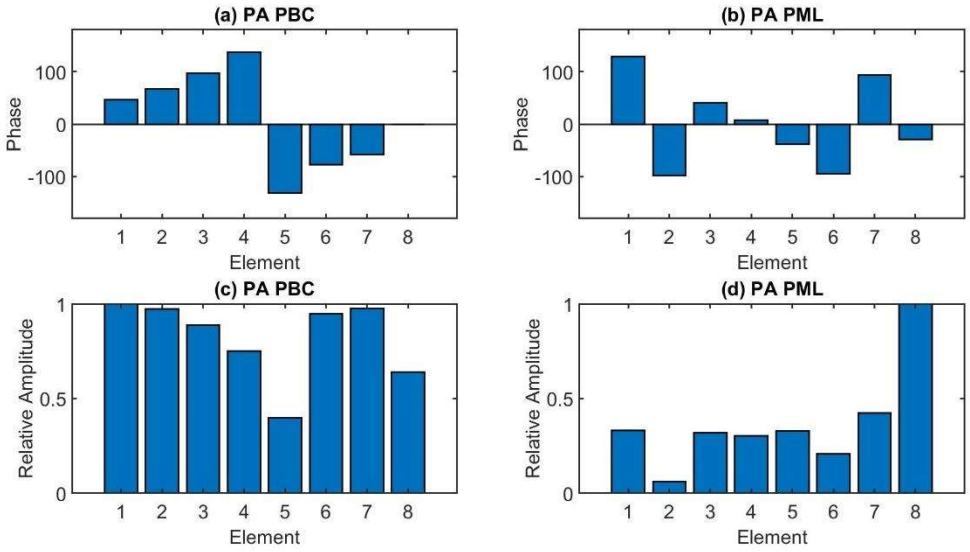

Figure 39. Bar charts depicting both the phase, (a) and (b), and amplitude, (c) and (d) imparted by each cell in the 8-element PBC, (a) and (c), and PML, (b) and (d), models. The phase plots show that the PBC model maintains a consistent phase difference, which is not the case for the PML model, where it varies wildly, and also maintains a higher mean amplitude than the PML model.

6.4 Single Element PML Model

Due to the fact that the 8-element PML model for the PA device showed more beamsteering than what was measured, a single-element PML model was sought. This model was similar to the ideal model in that each unit cell was modeled individually, but the difference was that instead of being bounded by PBC, it was bounded by PML. The result of this model is shown in Figure 40.

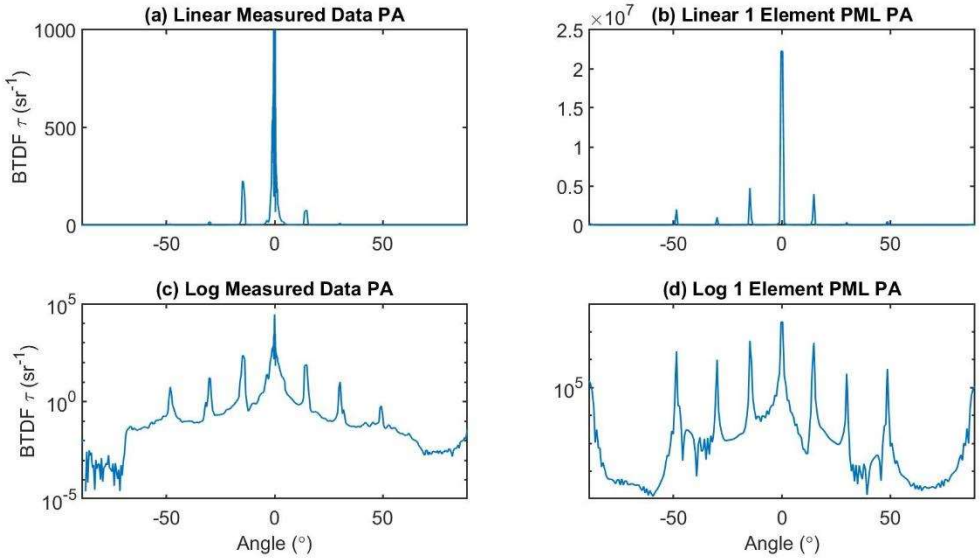

Figure 40. Comparison of BTDF measurement and one-element PML model of the PA beamsteerer; results are in ((a) and (b)) linear space and ((c) and (d)) log space. The y-axis in (a) is scaled down to show beamsteering in the measured device. The PML model shows the 0-order peak with 73% of the energy compared to 27% in the measurement, and 8% of the energy in -1-order peak compared to 2% for the measurement. In this model the ±1-order peaks are of almost exact magnitude, with the -1-order and +1-order peak having 8% and 7% of the energy deposited in them respectively.

As shown in Figure 40, the one-element PML model for the PA device is similar to the 8-element PML model for the BG device in the sense that it displays less beamsteering than what was measured. The presence of beamsteering in the 8-element PML model, contrasted to the lack of beamsteering in the one-element PML model, indicates that in the 8-element PML model, coupling between the different phase elements *across the MPL cavity* is occurring. So far when discussing coupling, the focus had been on elements that were only separated by the thickness of the MPL cavity wall. The 8-element PML model, which does not include elements that are separated only by a substrate wall, but rather by an entire cavity, shows for the first time that significant coupling also occurs across cavities and not just across the substrate walls.

6.5 Adjusted Models for PA

The previous three sections featured models of either a single phase element or the supercell which were unable to produce results that agreed with the measurements. This was similar to the BG device in that neither the ideal model nor the 8-element models were able to predict the measured data well. However, in the BG device, the 8-element PML model did not show any beamsteering, whereas it did for the PA device. In the subsequent implementation of adjusted models for the BG device, shown in Chapter V, the main rationale behind the adjusted models was that the 8-element PBC and PML models represented two extremes in coupling. The PBC model fully coupled the supercell with adjacent supercells and thus predicted a large amount of beamsteering, whereas the PML model fully uncoupled the supercell from adjacent supercells and thus predicted no beamsteering. The measured data for the BG device was somewhere in between these two extremes, so it was hypothesized that there was some coupling, but not as strong as in the PBC model. This led to the PBC-extended models, which adjusted the coupling and produced results that better predicted the measured data.

The rationale that was used to attempt the adjusted models for the BG device is no longer applicable to the PA device. As was shown in the previous sections, the cases that were two extremes for the BG device, the 8-element PBC and PML models, both show significantly more beamsteering than in the measured data for the PA device. On the other hand, for the one-element FEM models, the ideal model and the one-element PML model show a large amount of beamsteering and no beamsteering, respectively. Therefore, using the same logic that was previously applied to the BG device, a one-element PBC-extended

model should be able to predict the measured data, since the measured data falls in between these two extremes. The PBC-extended model was applied to both the one- and 8-element PA models to test these assumptions.

The PBC-extended FEM models for one-element unit cells and 8-element supercells are shown in Figure 41; the results of these models are shown in Figures 42 and 43, respectively. Figures 42 and 43 somewhat agree with what was hypothesized for these two models. When comparing the energy deposited in the designed -1-diffraction order (6% in the one-element and 33% in the 8-element) to the energy in the 0-order (90% in the one-element and 68% in the 8-element), the one-element PBC-extended model, with an added 1.5 MPL cavity, does a better job of predicting the measured data.

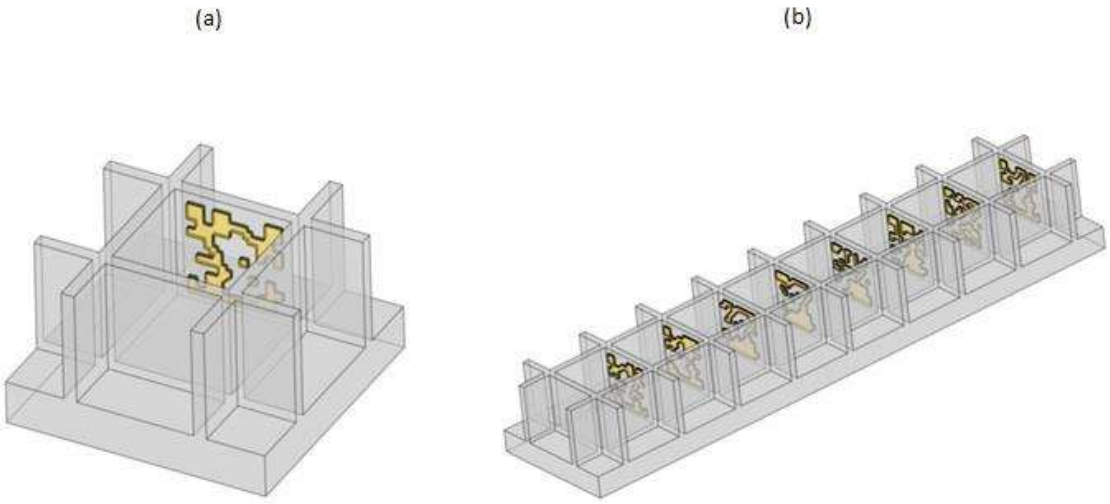

Figure 41. FEM models of the PA PBC extended designs, for both one element, (a), and a supercell, (b).

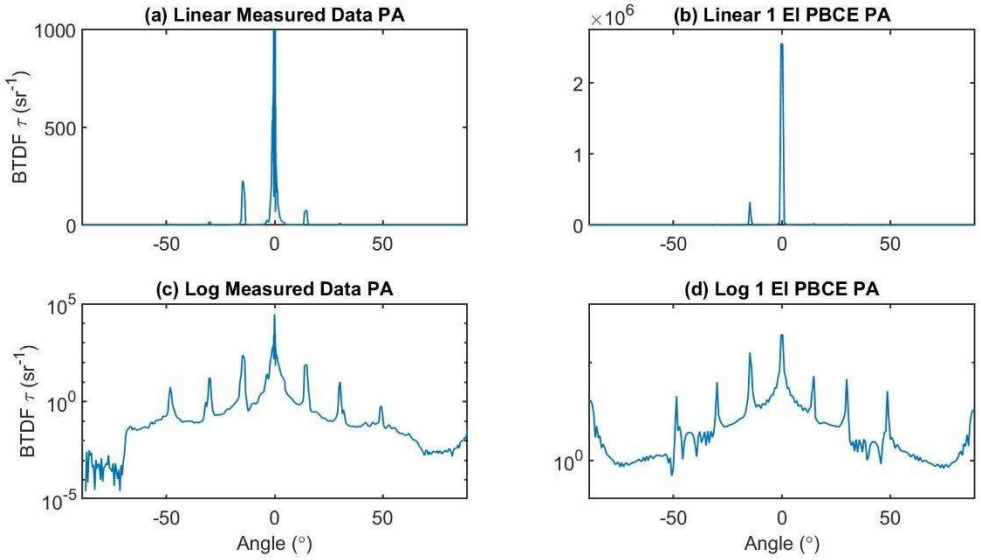

Figure 42. Comparison of BTDF measurement and one-element PBC extended model of the PA beamsteerer; results are in ((a) and (b)) linear space and ((c) and (d)) log space. The y-axis in (a) is scaled down to show beamsteering in the measured device. In this model 6% of the energy is in the -1-order, (2% in measurement), 90% in the 0-order (27% in measurement).

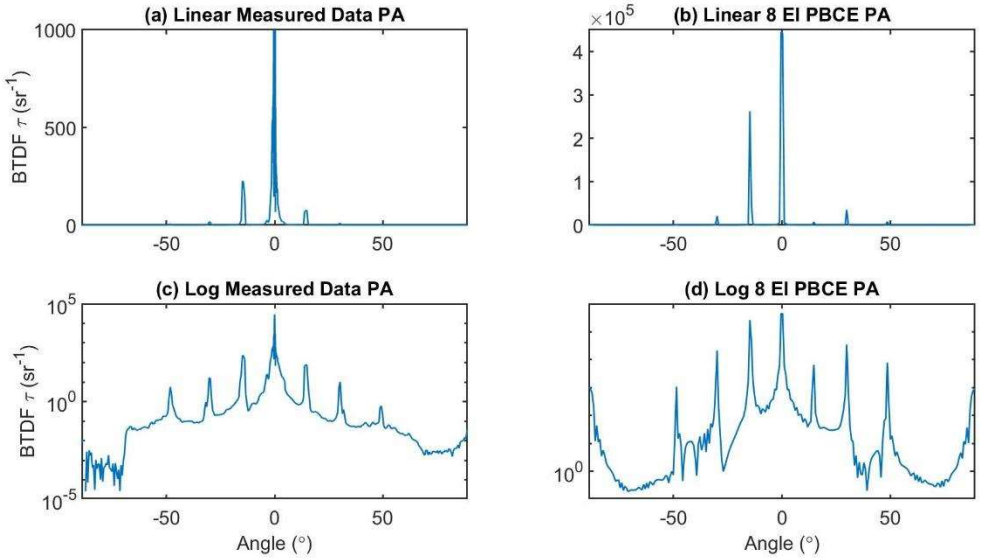

Figure 43. Comparison of BTDF measurement and 8-element PBC extended model of the PA beamsteerer; results are in ((a) and (b)) linear space and ((c) and (d)) log space. The y-axis in (a) is scaled down to show beamsteering in the measured device. In this model 33% of the energy is in the -1-order, (2% in measurement), 52% in the 0-order (27% in measurement).

A similar phase analysis to that accomplished in Table 4, which compared the relative amplitude and phase of the elements and the phase differences between elements for the ideal model and the one-element PBC-extended model is shown in Figure 44. The plots shown in Figure 44 (a) and (c) are the same shown in Figure 36. Figure 44 (a) and (b) show the phases of the successive phase elements, and (c) and (d) show the relative amplitudes of the eight phase elements for the single-element PBC (same as Table 6) and PBC-extended models. Again, the phase tilt or blaze of the supercell has been broken as the relatively consistent phase difference between successive elements for the PBC case is both lost and significantly reduced in magnitude in the PBC-extended case, where the RMS phase difference of the PBC-extended model is now 6.3° compared to 49.9° for the ideal case. This leads to the behavior observed in Figure 42, where the majority of the energy is in the 0-diffraction order, which agrees well with measurement. Similar to Section 5.3.1, a series of FEM models of the 8-element supercell was accomplished that progressively increased the spacing around the 8-element supercell in the PBC-extended model for the PA device. The results of these models are shown in Figure 45.

Figure 45 shows a progression in the PBC-extended model as the spacing around the supercell, both along the direction of polarization and orthogonal to it, is increased from 0.5-unit cells to 1-, 1.5- and 2-unit cells. Here the energy deposited in the 0-order is 24%, 38%, 52% and 23% for the Δ = 0.5, 1, 1.5 and 2 added spacings, respectively, and, 55%, 49%, 33% and 62% in the -1-order for the same spacings, respectively. The plot shown in Figure 43 (b) for a spacing of 1.5 is the same one shown in Figure 45 (c). The first thing to notice from the results shown in Figure 45 is that they do not follow the pattern that was shown in Figure 31 for the BG device. In Figure 45, as the spacing increases, energy shifts

from the -1-diffraction order to the 0-order, peaking with a spacing of Δ = 1.5, where the 0-order is the largest, but then shifts back to the -1-order at a further increased spacing of Δ = 2. The PBC-extended model for the BG device showed that as the spacing increased, the amount of energy deposited to the 0-diffraction order continued to increase, all the way to Δ = 2. This difference between the BG and PA designs in this model raises the question of what exactly is different between the two. To better understand the difference between the performance of the 8-element PBC-extended model for the PA device and the BG device, the relative amplitude and phase analysis of the models was accomplished, and the results are shown in Figures 46 and 47.

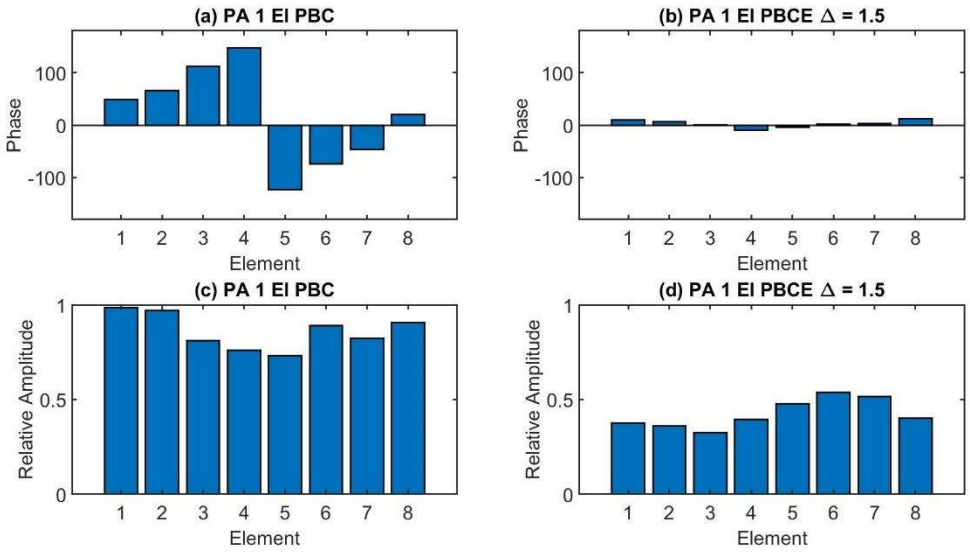

Figure 44. Bar charts depicting both the phase, (a) and (b), and relative amplitude, (c) and (d) imparted by each element in the ideal, (a) and (c), and 1-element PBC-extended, (b) and (d), models. The phase plots show that the ideal model maintains a consistent phase difference, which is not the case for the PBC-extended model, where there is almost no variation, and also maintains a higher mean amplitude than the PBC-extended model, both of these factors contributes to the fact that ideal model is much more effective at beamsteering.

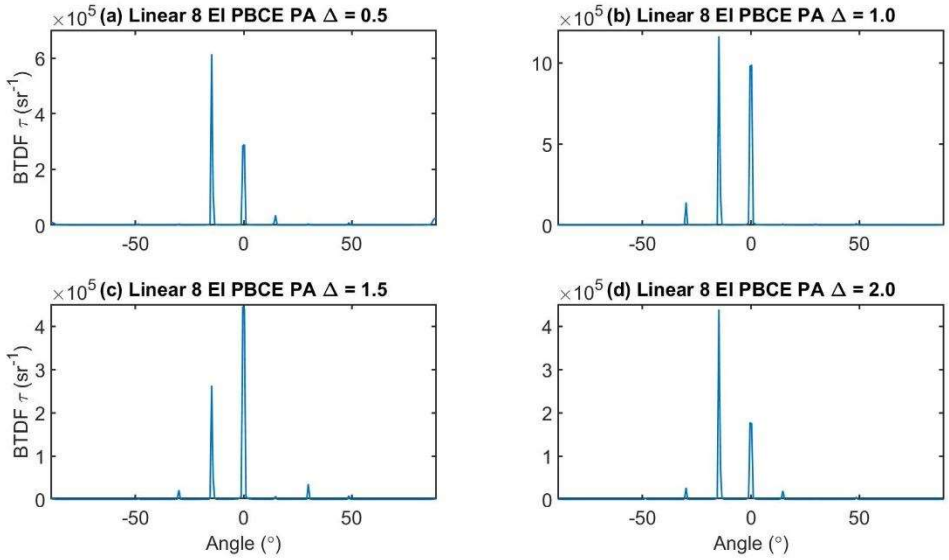

Figure 45. Comparison of modeled BTDF for the PBC extended case as the spacing around the supercell is increased from 0.5 (a), 1.0 (b), 1.5 (c), and 2.0 (d). The energy deposited in the 0- and -1-orders for the four cases are, 24% and 55% for 0.5, 38% and 49% for 1, 52% and 33% 1.5, and 23% and 62% for 2. The only scenario in which the 0-order is higher than the -1-order is when the spacing is an additional 1.5 unit cells.

Figure 46 shows the relative amplitudes of the individual phase elements with respect to the undecorated cavities for the different spacings used in the PBC, PML and PBC-extended models, and Figure 47 shows the phase between the successive phase elements for all these cases. Figure 47 again shows the relatively consistent phase tilt of the successive elements of the PBC case (same as Table 7) is lost as the magnitudes of the phases are decreased or the sequential phases even begin to oscillate as the spacings increase. The RMS phase difference value for the PBC-extended case as the spacing increases is 73.6°, 46.8°, 14.6° and 26.3°, for $\Delta = 0.5$, 1, 1.5 and 2, respectively. The fact that the RMS value of the PBC-extended case is lowest at $\Delta = 1.5$, agrees well with Figure 45 (c), which is the worst of these at beamsteering.

While there were differences in how the PBC-extended models affected the BG and PA designs, in both cases the versions of those models that were able to better predict the

performance of the measured devices did so by affecting the amplitudes of the individual phase elements and the phase blaze of the supercell. For the 8-element PBC-extended model for both the BG and PA designs, with $\Delta = 0.5$ spacing and $\Delta = 1.5$ spacing, respectively, the RMS phase difference value and relative amplitudes of the individual phase elements with respect to the ideal unadjusted model were decreased. This repeated success by adjusting both the phase blaze and phase-element amplitudes of the models lends credence to the hypothesis that these are the equivalent effects that are affecting the performance of the fabricated device.

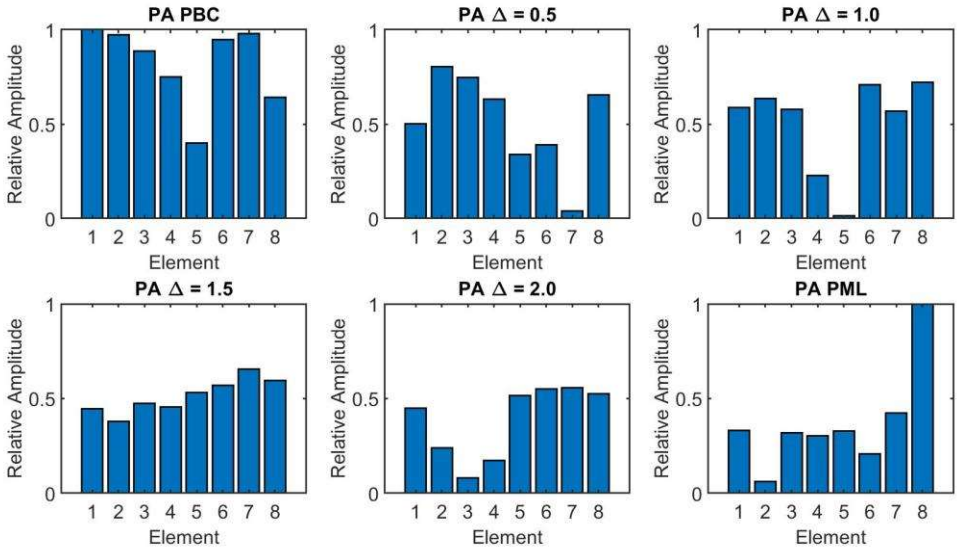

Figure 46. Relative amplitudes among adjacent elements for the 8-element FEM models of the PA device. The amplitude of the PBC case is the highest when compared to the PBC-extended models, but it is also shown that relative to the other spacings the $\Delta = 2$ seems to have the lowest average amplitude. The PML model has the lowest average amplitude out of the six models.

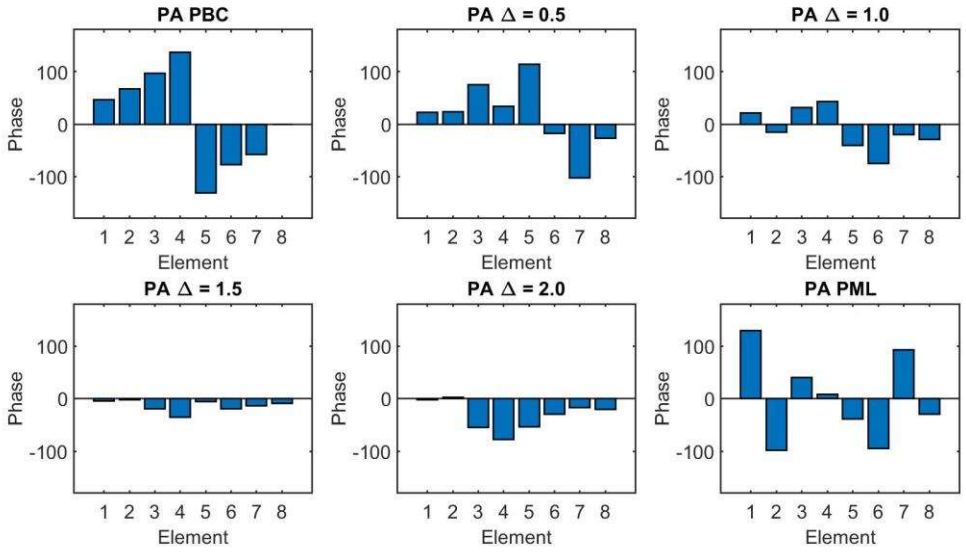

Figure 47. Phase of the elements for the 8-element FEM models of the PA device. The PBC model has a relatively constant phase difference, unlike the rest of the models. The Δ = 1.5 spacing case shows the smallest phase difference which leads to the simulated BTDF showing the least beamsteering.

With respect to how the PBC-extended model affected the simulated BTDF of either the BG or PA device, it is important to study their differences. One of the differences between the BG and PA designs is the direction of the phase wrap with respect to the polarization direction, which means that the application of the PBC-extended model between the two designs is significantly different. The phase elements in the supercell share a substrate wall with elements within the supercell for the BG design, whereas they share a substrate wall with like elements outside the supercell for the PA design. In the PA design, as the spacing around the supercell increases, so does the spacing that "buffers" each phase element. In the BG design, six out of the eight phase elements in the supercell are still separated only by a substrate wall from neighboring elements in the supercell. Here, as the spacing increases around the supercell, only the two end elements have an increasing gap between themselves and an adjacent phase element, and only on one side.

Along the direction of polarization, as the spacing increases in the PA design, the periodicity between each individual phase element and identical phase elements is increased. This means that there is a different phasing between like phase elements that is occurring due to the different spacing. In the BG design, it is the spacing between adjacent supercells that increases, rather than between individual like phase-elements.

The PBC-extended model for the PA device shows that increasing the spacing does not simply result in a linearly decreasing blaze, as was the case for the BG design, but rather a cyclical reduction in the blazing that once it crosses a threshold, starts to direct energy back to the design diffraction order. Even with added spacing, the supercells are still periodic, but the spacing changes the periodicity. The fact that the energy cycles between the designed -1-diffraction order and the 0-order is an indicator that there may be a periodic 0-to-π phase shift associated with the spacing between adjacent supercells. This effect could also be present in the BG case, but the spacing is being added between adjacent supercells, or along the blaze of the beamsteerer's blazed diffraction grating, rather than between like phase elements of a phased array, which makes its effect less consequential.

6.6 Phased Array Beamsteerer Device Summary

The computational methods that were developed for the study of the blazed-grating beamsteerer were applied here to the phased-array device, and their effectiveness studied. This study began by comparing measurements of the fabricated PA device to ideal models, but the measurements showed a strong 0-order diffraction that was not present in modeling results, similar to the results of the BG device. Also similar to the BG device, the 8-element

PBC model of the PA displayed too much beamsteering when compared to the measurements. Unlike for the BG device, however, the 8-element PML model for the PA device showed more beamsteering than the measurement; the same model for the BG device showed too little beamsteering. This difference led to the one-element PML model for the PA device which produced no beamsteering. This difference between the 8- and one-element PML models showed for the first time that there was indeed significant coupling of the phase elements occurring across the MPL cavities in these devices.

Further PBC-extended modeling of the PA device was accomplished for both one- and 8-element models, and both directed more energy into the 0-diffraction order than the designed -1-order, as in the measurements. A study which varied the size of the spacing around the supercells of the 8-element PBC-extended model again showed the decoupling that the PBC-extended accomplished results in an inconsistent phase blaze and reduced or irregular amplitudes among the phase elements of the supercell, which again appears to explain the performance of the measured device.

VII. Conclusions

7.1 Introduction

The main motivator for the work accomplished in this dissertation was to better understand what phenomena were affecting the behavior of fabricated plasmonic metasurface optical devices, in this case, blazed transmissive diffraction gratings, or "beamsteerers," in that this behavior differed significantly from that predicted by the ideal models. As mentioned in the Introduction chapter, metasurface optical devices are a key item of interest for the DoD; therefore, it is important to understand what issues might plague the performance of these fabricated devices. To that end, successful methods were developed that accounted for the behavior by both modeling defects observed in the fabricated devices, and by methods that incorporated changes in the coupling of the phase elements that predicted results similar to those observed in measurements.

7.2 Devices Studied

The devices studied were two distinct metasurface optical beamsteerers. There was a variety of similarities and differences between the two devices, which were termed the blazed-grating (BG) and phased-array (PA) devices. Similarities included their fabrication technique, Membrane Projection Lithography (MPL), the number of distinct phase elements designed to cover the 0-to-2π phase shift range required for optical devices, eight, the method by which these phase elements were designed, a Genetic Algorithm (GA), the

method by which they induce a phase shift, gold decorations that act as plasmonic scatterers, and the placement of the gold decorations with regards to the incoming EM wave, in an out-of-plane (OOP) configuration. This configuration meant they were deposited on the walls of cavities formed in the substrate, or OOP with the plane of the substrate, such that they would be tangential to the direction of propagation of the light with which they interact, rather than deposited normal to the direction of propagation.

The differences between the devices although subtle, did impact their behavior. The first of these differences is the wavelengths at which they were designed to operate, with the BG device operating at $\lambda = 8$ μm and the PA device operating broadband at $\lambda = 5.5$, 6.0, 6.25 and 6.5 μm, although it was specifically designed at 6 μm.

Another difference between the two devices is the direction of the phase wrap of the blazed diffraction grating, which is the succession of phase elements that cover the 0-to-2π phase range. In the BG device, the phase wrap is along the direction of polarization of the incident light and there were only four distinct phase elements used out of the designed eight to cover the 0-to-2π phase range. To fill the 8-element supercell, each distinct phase element was used twice, repeating in a pattern such as 1-1-3-3-5-5-7-7, where the number denotes a specific phase element used. The direction orthogonal to the polarization direction had identical phase elements. The important thing to note is that in this configuration, the polarization direction is also the direction in which the phase elements are closest to one another and the only thing that separates them is the substrate wall, which is 300-nm thick, formed between the MPL cavities formed in the substrate. This proximity means interactions between phase elements in this configuration should be stronger.

In the PA device, the phase wrap is along the direction orthogonal to the polarization, meaning the successive phase elements are separated by the substrate wall and the 2.7 μm long cavity. The direction that is aligned with the polarization, and separated only by a substrate wall, is populated with identical phase elements. The PA device used all designed eight elements.

With regards to the design space of the devices, each phase element unit cell was designed individually and surrounded by Periodic Boundary Conditions (PBC), meaning every phase element is essentially surrounded by an infinite periodicity of itself, a condition that is inconsistent with both configurations of the two devices just described. However, the PA design is much closer to these GA conditions since here, like elements are separated only by a substrate wall. In the BG device, where there are two like elements side by side in the phase wrap, the majority of the like elements are across from each other, separated by a substrate wall and an entire empty cavity, which for the BG device is 2-μm long. These design considerations were very important when attempting new models and techniques to analyze these fabricated devices' measured performance.

7.3 Research Questions

Four research questions were posed at the beginning of this document. These can be categorized as: Which modeling methodology is best? What can be learned from these methodologies? How can defects be incorporated into the models? What from these models could be incorporated into future designs to improve device performance?

7.3.1 Optimal Modeling Methodology

The first question was, "What modeling methods are useful in predicting the behavior of the fabricated devices and which are not?" The method that was shown to work for both devices was termed the "PBC-extended" model, which introduced a "decoupling" between the phase elements of the modeled supercells. This decoupling could be adjusted in both amplitude and phase to achieve models that well-predicted the results measured for fabricated devices.

Other methods were attempted, and some were either partly successful or completely unsuccessful, but ultimately pointed the way to the PBC-extended model. These other unsuccessful methods included one that used perfectly matched layers (PML) as boundary conditions and added additional phase elements at the end of the supercell, but this model did not produce enough beamsteering. Others either introduced random phase shifts, or certain random variations within the supercells, but these also did not produce results representative of the fabricated devices' behavior.

The basis for the successful adjusted models in the BG device was motivated by the fact that the 8-element, i.e. the size of the supercell, PBC model over-predicted the fabricated beamsteerer performance, while the 8-element PML model underpredicted it. It was expected that the increasing spacing added in the PBC-extended model would allow for the beamsteerer performance to be adjusted until it agreed with measurement. In the PA device, this same argument was applied to the 1-element PBC and PML models, which over-predicted and underpredicted the performance of the fabricated device, respectively.

The PBC-extended models were further analyzed by studying how the amplitude and phase imparted by each unit cell changed as the spacing increased for either the BG or PA device. It was observed that as the spacing increased in the BG device the phase difference between adjacent cells decreased, making it behave more like a regular, i.e. not blazed, diffraction grating. This was not the case for the PA device, where rather than monotonically degrading the blaze of the beamsteerer, the increased spacing caused a cyclical response in which after a particular spacing, the blaze of the model improved once again.

A defect study was also carried out for the BG device. This method identified several defects observed in SEM images of the fabricated device and classified them as either "global" or "local" defects, and implemented them in the FEM models. The global defects were found to more likely impact the performance of the device, as models of the 8-element supercell with defects consisting of lateral displacements of the gold plasmonic decorations on the MPL cavities' side walls were found to well-predict the behavior of the fabricated device. This method, while successful, was more difficult to implement, and limited in the type of defects that could be modeled in the FEM environment and how to implement them in this environment.

7.3.2 Lessons Learned from Optimal Modeling Methodology

The second research question that was addressed was, "What do the functional modeling methods tell us about the effects that degraded the fabricated devices' performance?" The variety of models showed that the issue of coupling, which was studied

in Chapters V and VI, is very important in understanding how these devices behave. This was first shown by comparing performance of BG and PA beamsteerers modeled with the same phase elements. The PA device, which has like elements essentially side by side, separated only by a MPL cavity's substrate wall of thickness 300 nm, is more effective at steering the beam. The only thing that differed between the two designs is the placement of the phase elements. This comparison shows the importance of coupling between elements that are only separated by the MPL cavity walls.

Furthermore, when comparing the one- and 8-element PML models of the PA device, the 8-element model showed beamsteering while the one-element model did not. This showed that there is significant coupling between phase elements separated by the full space of the MPL cavity. This coupling had not been specifically demonstrated previously.

The PBC-extended models for both devices were attempts at adjusting the coupling to obtain models that better predicted the measurement. For both devices, it was found that the specific spacing of the PBC-extended model that predicted the performance of the fabricated beamsteerer did so by both worsening the phase blaze of the diffraction grating and the regular amplitudes of the individual elements. This strongly implies that in comparison to ideal models, the fabricated devices suffer from less-than-optimal phase blazes and amplitudes.

7.3.3 Models with Defects Incorporated

The third research question asked was, "How can defects be modeled to attempt to explain the behavior of the fabricated devices?" This question was addressed in Chapter

IV and partially described in the answer to the first question. Two different defects were studied, displacement of the plasmonic gold elements either vertically or horizontally on the MPL cavity walls, referred to here as "global" defects, and the random addition and subtraction of gold material to/from the phase elements, referred to here as "local" defects. The first study showed that global defects affected the amplitude and phase shift imparted by the phase elements to a much greater extent than the local defects did. A subsequent study solely focused on the horizontal displacement of the gold decorations in a supercell, and found that as this displacement increased, the agreement between modeled predictions and measurement results improved. Further, it was shown that it was specifically the removal of gold from the intended wall of the MPL cavity that was introduced by this horizontal displacement as some gold was wrapped to an adjacent side wall that produced these results. These two studies were the first to characterize the effects of defects on plasmonic metasurface optical devices and showed directly how the phase elements themselves affect the performance of the device.

7.3.4 Improvements for Future Designs

The last question asked was related to the GA design of these devices and was, "Is there anything learned from the functional models and the modeled defects that can lead to a new design space that would improve the performance of these fabricated devices?" The impact of coupling on the performance of these devices was described in the answer to the second question and shows that this issue is key to understanding how to build better-performing devices. Initially it was thought that the PBC-extended models were able to

adjust coupling *strength* by increasing an arbitrary spacing inserted around the modeled elements, but this was not the full case. The PBC-extended models produced results that better predict the measured results for the PA device by adjusting the *phase* of the coupling between neighboring supercells, as well as the strength of the coupling. Better understanding coupling should lead to being able to design more robust phase elements if they can be designed to be less reliant on nearby elements in order to impart their designed amplitude and phase shift.

7.4 Lessons Learned and Future Work

A variety of modeling techniques was applied in an attempt to understand the performance of fabricated plasmonic metasurface optical devices, and as a result, the effectiveness of these techniques was determined and a deeper understanding of how these metasurface optical devices behave was achieved. Directly addressing defects observed in SEM images of fabricated devices led to models that showed good agreement with measurements. More *indirect* approaches to modeling "defective" devices led to a better understanding of the effects that influence the behavior of the device, such as phase-to-phase element coupling, and showed that by developing models that could be adjusted to be more predictive of the measurements, insight into the behavior of the fabricated device could be attained. These studies demonstrated that real device performance can be analyzed in models that incorporate details and this can be used to further refine designs. These methods and processes developed could also be applicable to dielectric as well as metallic metasurfaces.

It is yet to be determined how these adjustments can be implemented in the genetic algorithm (GA) process that designs the phase elements for these devices. However, future work is already planned as more metasurface optical beamsteerers are scheduled to be fabricated by SNL that will incorporate both the Adomanis (BG) and Pennsylvania State University's (PA) designs. Measurement and study of these new devices will further help in refining our analysis techniques, and in devising new ways to design and analyze the devices. In terms of modeling, coupling is hypothesized to be the path that would yield the most fruitful results, and a more-thorough study, which makes use of the understanding developed here as to why the decoupling as it is implemented in the PBC-extended models is so effective at predicting measured device performance, would be key to developing better-performing fabricated plasmonic metasurface devices.

Also, it is possible with the current characterization device, AFIT's CASI, to obtain the full Mueller matrix for the directional scatter of the devices. As metasurfaces have shown to be optically active, this would serve as another tool to better understand their performance.

Appendices

A. Plots of all four polarization configurations

This appendix contains the plots presented in the dissertation which compare the performance of the measured device versus the models, and it contains all four polarization states measured with the CASI, which are H/H, H/V, V/V, and V/H, where H/V for example is input polarization horizontal, measured polarization vertical. The design polarization in this experiment was the horizontal polarization, and all the images shown in the main document are in the H/H configuration.

Figures 48 – 52 show the measured data from the two devices, the blazed-grating and phased-array beamsteerer. The blazed-grating device was measured at $\lambda = 8$ μm, for all four polarization configurations, and the phased-array was measured at $\lambda = 5.5$, 6.0, 6.25, and 6.5 μm for all four polarization configurations with the exception of the measurement at $\lambda = 6.25$ μm which only measured H/H and H/V.

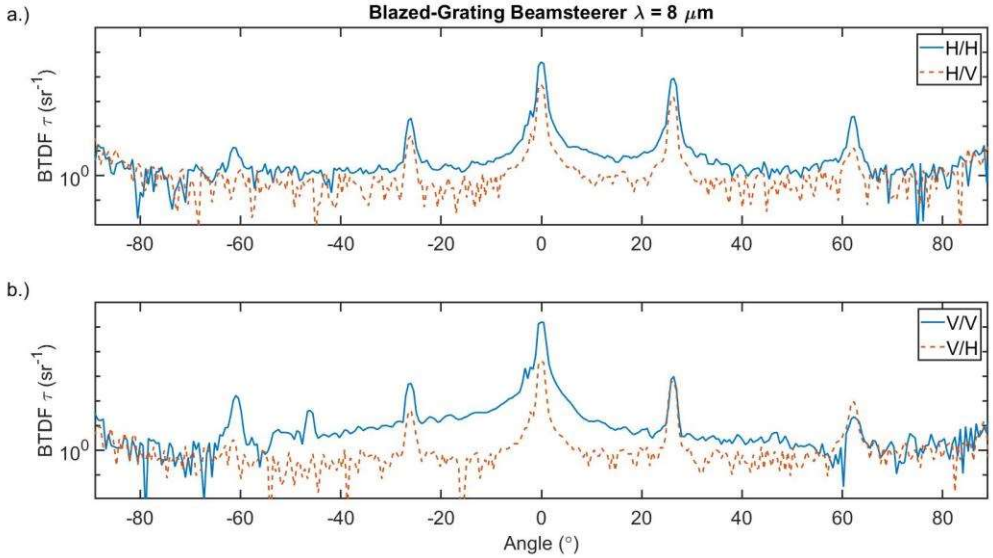

Figure 48. BTDF Measurements of the blazed-grating beamsteerer at λ = 8 μm, for all four polarization configurations. a.) shows the input design polarization, output design polarization (H/H), and output orthogonal polarization (H/V). b.) shows the input orthogonal polarization, output orthogonal polarization (V/V), and output design polarization (V/H). As seen in a.) the majority of the energy is deposited in the 0-peak order, followed by the +1 order peak, the designed peak of the beamsteerer.

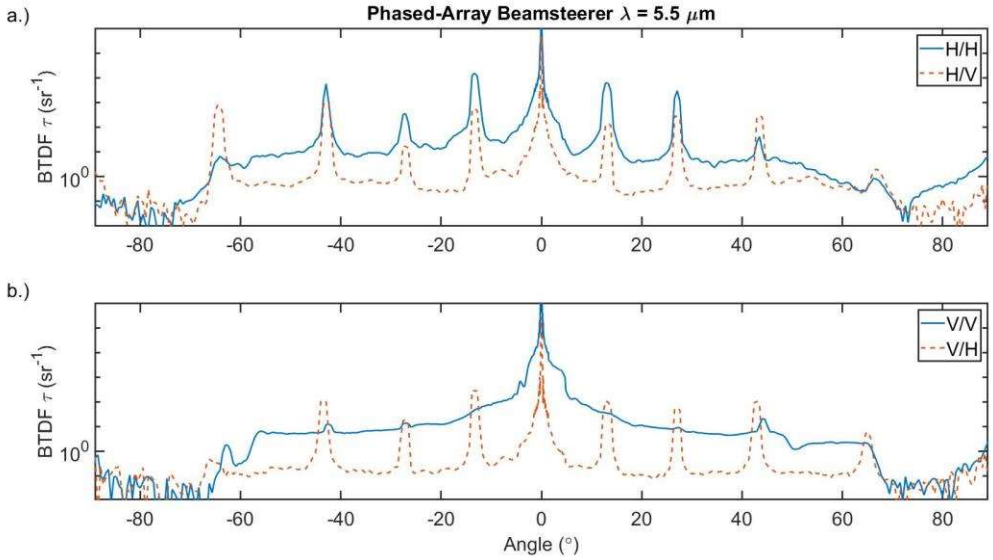

Figure 49. BTDF Measurements of the phase-array beamsteerer at λ = 5.5 μm, for all four polarization configurations. a.) shows the input design polarization, output design polarization (H/H), and output orthogonal polarization (H/V). b.) shows the input orthogonal polarization, output orthogonal polarization (V/V), and output design polarization (V/H). As seen in a.) the majority of the energy is deposited in the 0-peak order, followed by the -1 order peak, the designed peak of the beamsteerer.

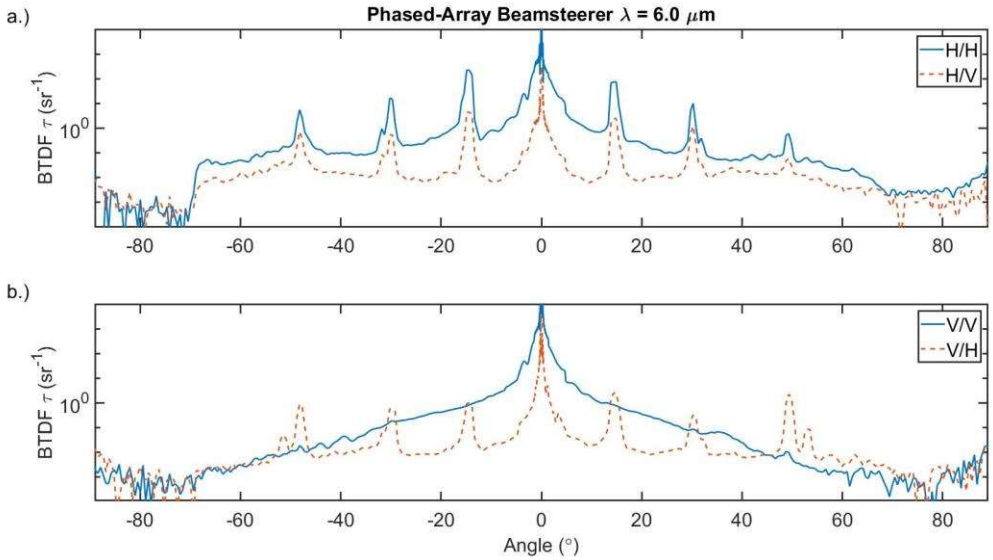

Figure 50. BTDF Measurements of the phase-array beamsteerer at λ = 6.0 μm, for all four polarization configurations. a.) shows the input design polarization, output design polarization (H/H), and output orthogonal polarization (H/V). b.) shows the input orthogonal polarization, output orthogonal polarization (V/V), and output design polarization (V/H). As seen in a.) the majority of the energy is deposited in the 0-peak order, followed by the -1 order peak, the designed peak of the beamsteerer.

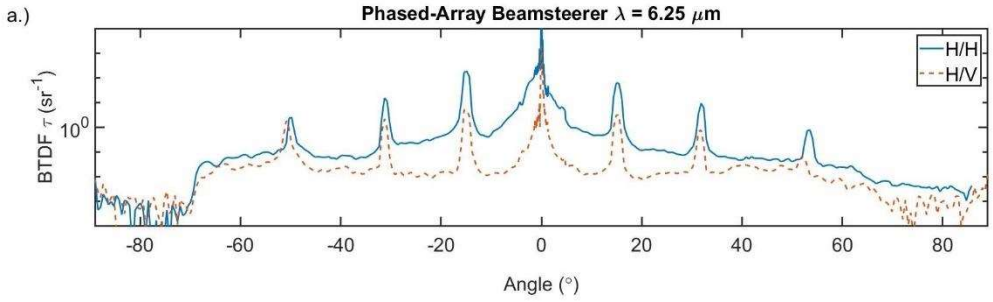

Figure 51. BTDF Measurements of the phase-array beamsteerer at λ = 6.25 μm, for two polarization configurations. a.) shows the input design polarization, output design polarization (H/H), and output orthogonal polarization (H/V). No data was collected at this wavelength for input orthogonal polarization. As seen in a.) the majority of the energy is deposited in the 0-peak order, followed by the -1 order peak, the designed peak of the beamsteerer.

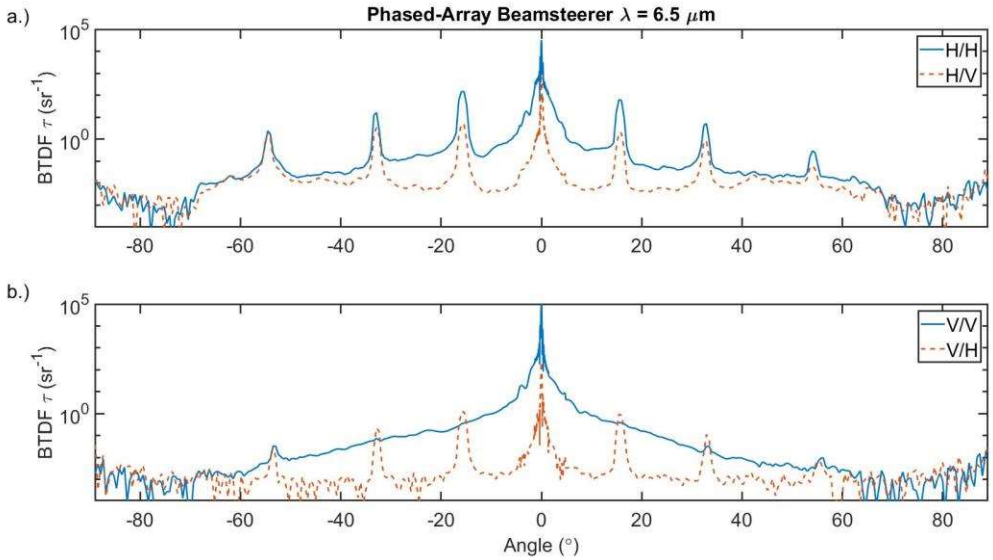

Figure 52. BTDF Measurements of the phase-array beamsteerer at λ = 6.5 μm, for all four polarization configurations. a.) shows the input design polarization, output design polarization (H/H), and output orthogonal polarization (H/V). b.) shows the input orthogonal polarization, output orthogonal polarization (V/V), and output design polarization (V/H). As seen in a.) the majority of the energy is deposited in the 0-peak order, followed by the -1 order peak, the designed peak of the beamsteerer.

Figure 53 and 54 show the 8-element PBC and PML models for the BG device respectively at both the design and orthogonal polarization. Figure 55 shows the 8-element PBC-extended model at a spacing of Δ = 0.5 for both the design and orthogonal polarization.

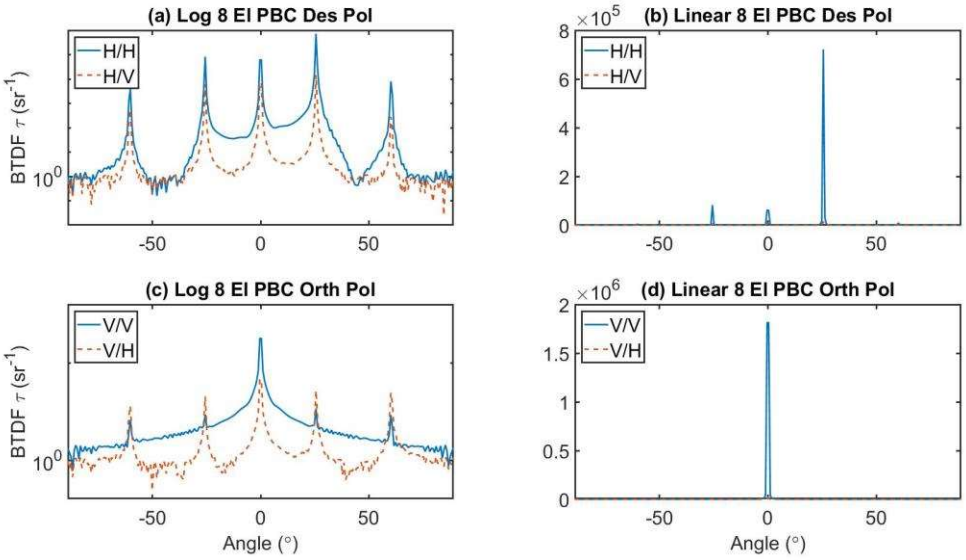

Figure 53. Model of the BG beamsteerer BTDF with near field data collected from 8-element FEM models with PBC, with (a) and (c) corresponding to the data presented in log space, and (b) and (d) in linear space.

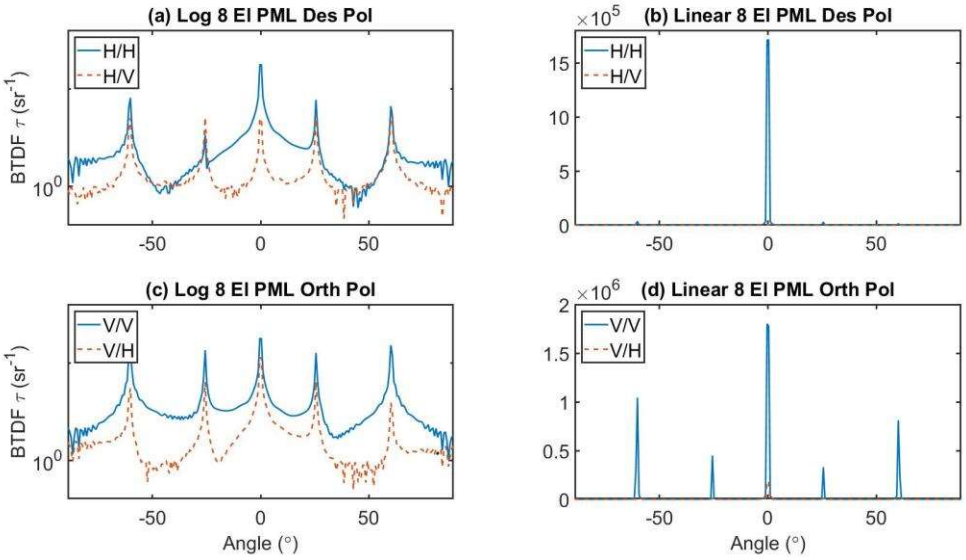

Figure 54. Model of the BG beamsteerer BTDF with near field data collected from 8-element FEM models with PML, with (a) and (c) corresponding to the data presented in log space, and (b) and (d) in linear space.

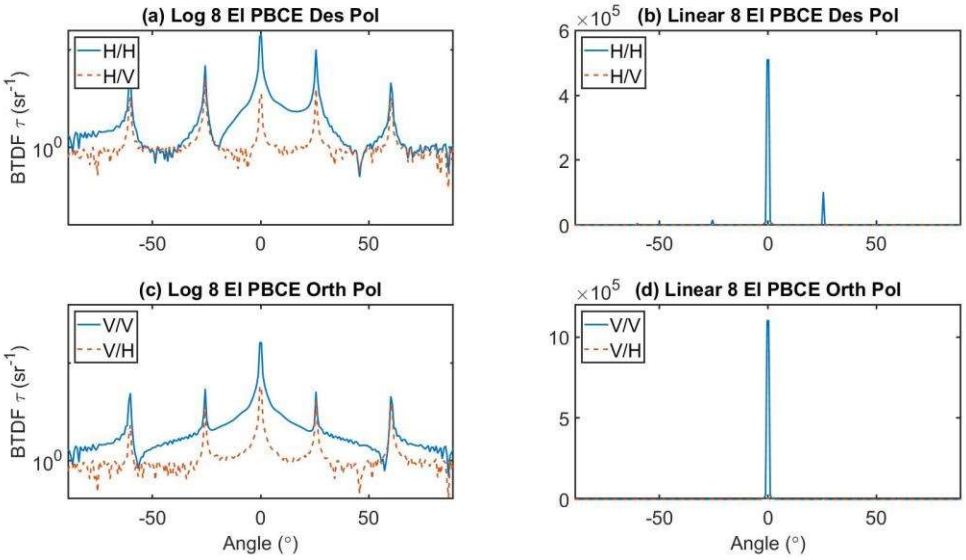

Figure 55. Model of the BG beamsteerer BTDF with near field data collected from 8-element FEM models with PBC and added spacing, the PBC extended configuration, with (a) and (c) corresponding to the data presented in log space, and (b) and (d) in linear space.

The next set of Figures correspond to the PA device. Figures 56 and 57 show the 1-element PBC model for the PA device for design and orthogonal polarizations, respectively. Figures 58 – 61 show the 8-element PBC and PML model for the PA device for design and orthogonal polarizations, respectively. Figures 62 and 63 show the 1-element PML model for the PA device for design and orthogonal polarizations, respectively. Figures 64 and 65 show the 8-element PBC-extended model with $\Delta = 1.5$ spacing for the PA device for design and orthogonal polarizations, respectively.

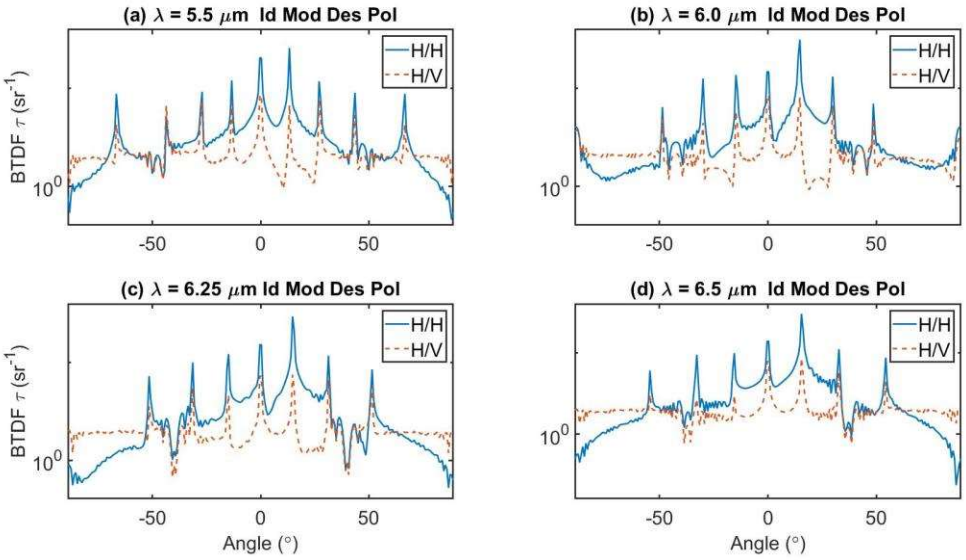

Figure 56. Model of the PA beamsteerer BTDF with near field data collected from 1-element FEM models with PBC for all four wavelengths for input design polarization, with (a), (b), (c), and (d) corresponding to λ = 5.5, 6.0, 6.25 and 6.5 μm respectively. All plots are in log space.

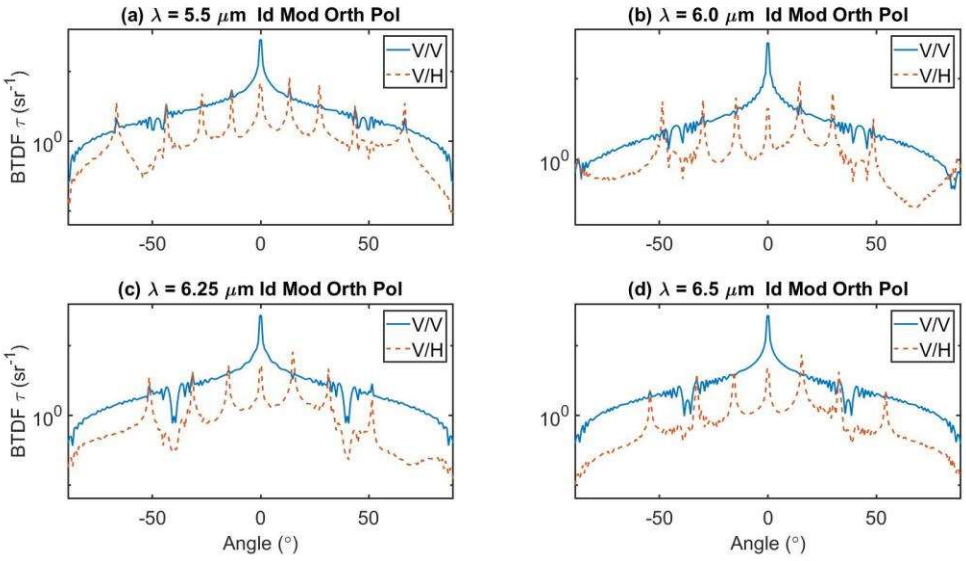

Figure 57. Model of the PA beamsteerer BTDF with near field data collected from 1-element FEM models with PBC for all four wavelengths for input orthogonal polarization, with (a), (b), (c), and (d) corresponding to λ = 5.5, 6.0, 6.25 and 6.5 μm respectively. All plots are in log space.

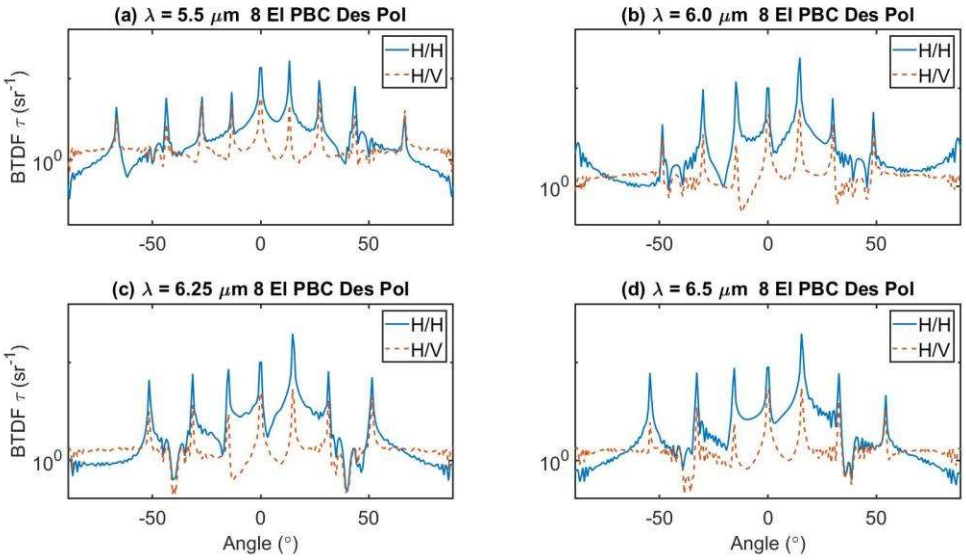

Figure 58. Model of the PA beamsteerer BTDF with near field data collected from 8-element FEM models with PBC for all four wavelengths for input design polarization, with (a), (b), (c), and (d) corresponding to λ = 5.5, 6.0, 6.25 and 6.5 μm respectively. All plots are in log space.

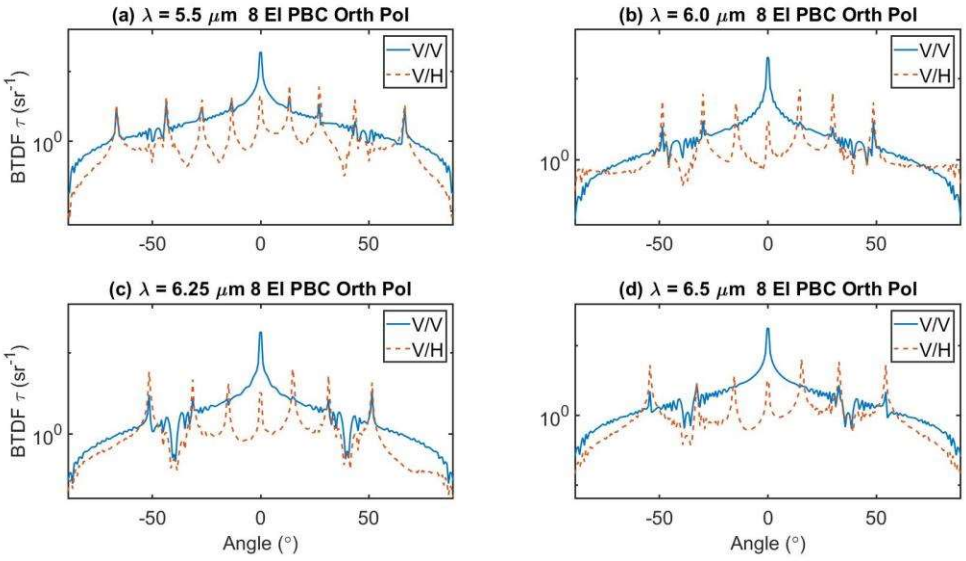

Figure 59. Model of the PA beamsteerer BTDF with near field data collected from 8-element FEM models with PBC for all four wavelengths for input orthogonal polarization, with (a), (b), (c), and (d) corresponding to λ = 5.5, 6.0, 6.25 and 6.5 μm respectively. All plots are in log space.

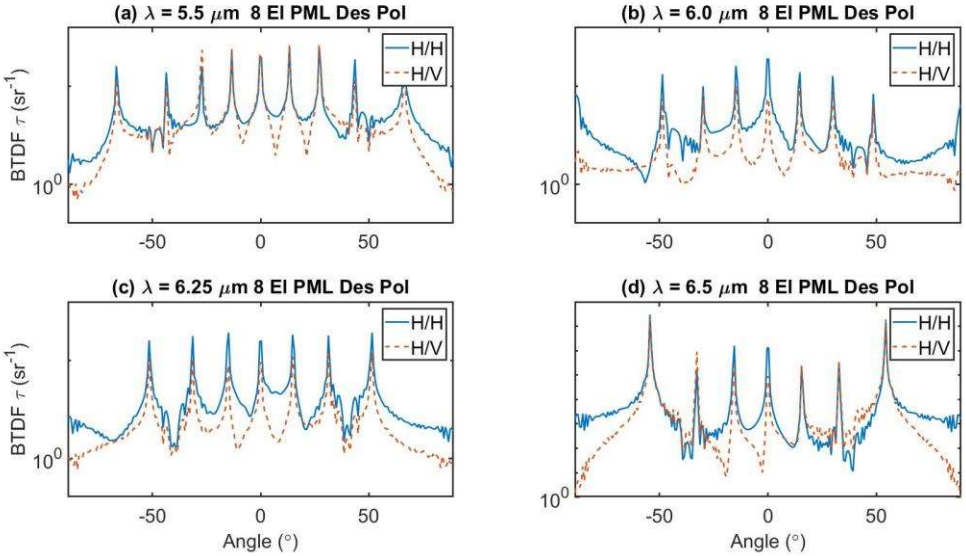

Figure 60. Model of the PA beamsteerer BTDF with near field data collected from 8-element FEM models with PML for all four wavelengths for input design polarization, with (a), (b), (c), and (d) corresponding to λ = 5.5, 6.0, 6.25 and 6.5 μm respectively. All plots are in log space.

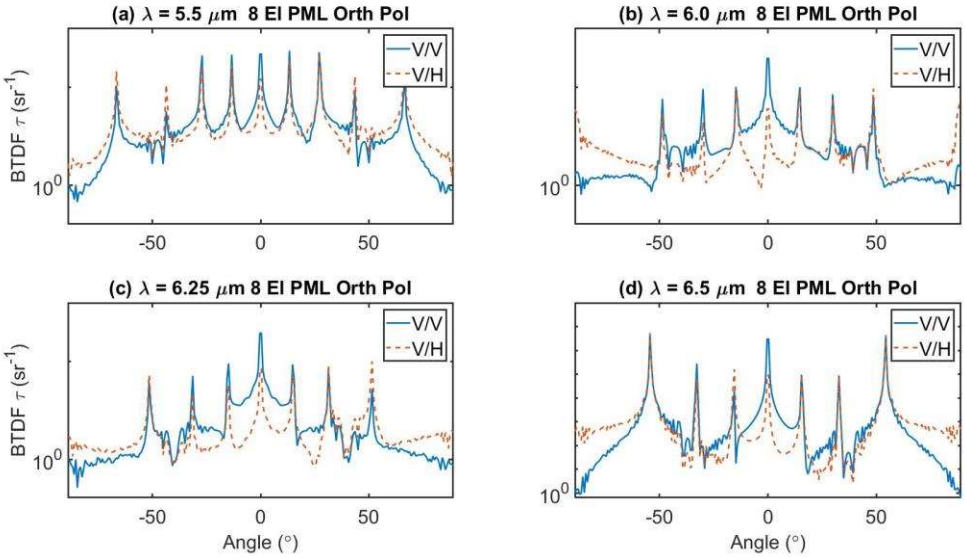

Figure 61. Model of the PA beamsteerer BTDF with near field data collected from 8-element FEM models with PML for all four wavelengths for input orthogonal polarization, with (a), (b), (c), and (d) corresponding to λ = 5.5, 6.0, 6.25 and 6.5 μm respectively. All plots are in log space.

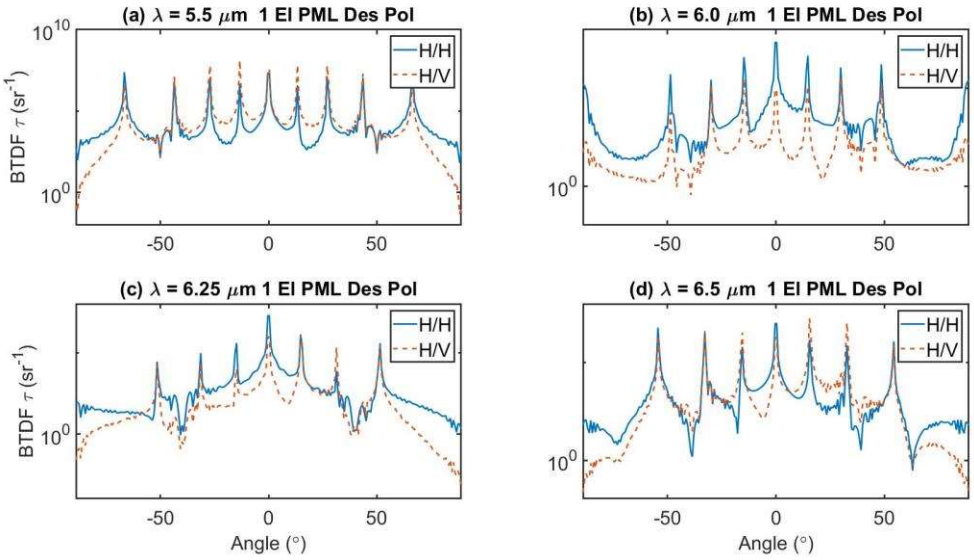

Figure 62. Model of the PA beamsteerer BTDF with near field data collected from 1-element FEM models with PML for all four wavelengths for input design polarization, with (a), (b), (c), and (d) corresponding to λ = 5.5, 6.0, 6.25 and 6.5 μm respectively. All plots are in log space.

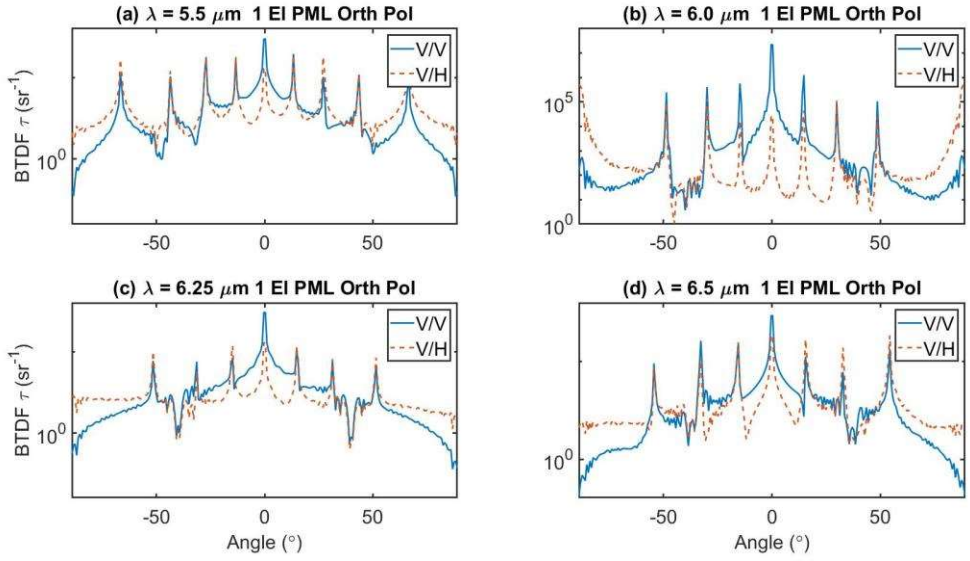

Figure 63. Model of the PA beamsteerer BTDF with near field data collected from 8-element FEM models with PML for all four wavelengths for input orthogonal polarization, with (a), (b), (c), and (d) corresponding to λ = 5.5, 6.0, 6.25 and 6.5 μm respectively. All plots are in log space.

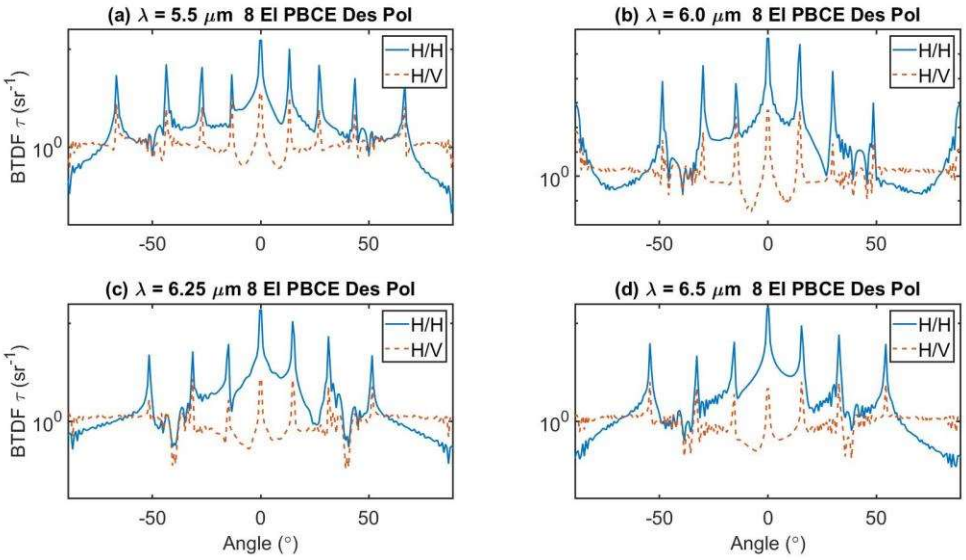

Figure 64. Model of the PA beamsteerer BTDF with near field data collected from 1-element FEM models with PML for all four wavelengths for input design polarization, with (a), (b), (c), and (d) corresponding to λ = 5.5, 6.0, 6.25 and 6.5 μm respectively. All plots are in log space.

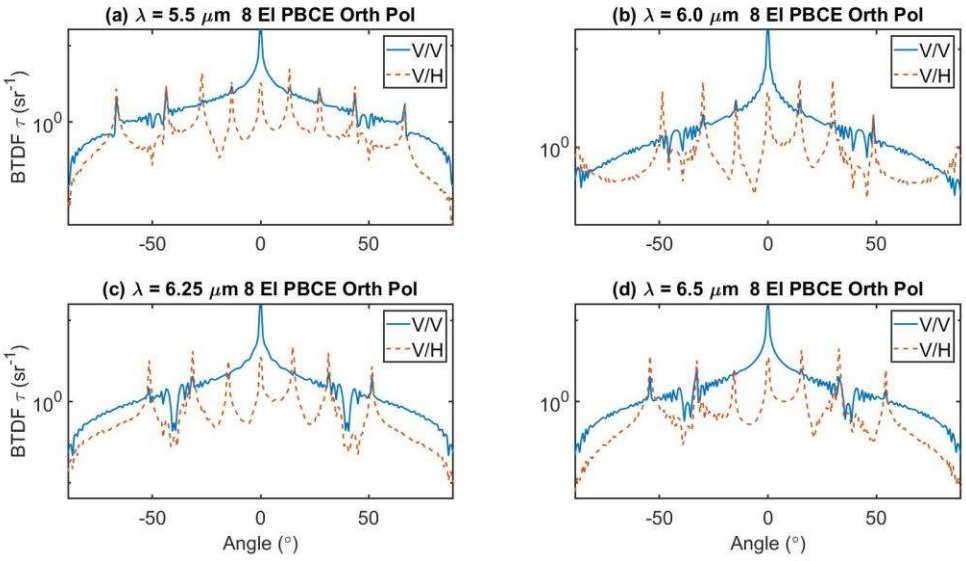

Figure 65. Model of the PA beamsteerer BTDF with near field data collected from 8-element FEM models with PML for all four wavelengths for input orthogonal polarization, with (a), (b), (c), and (d) corresponding to λ = 5.5, 6.0, 6.25 and 6.5 μm respectively. All plots are in log space.

Bibliography

1. ENIAC, https://encyclopedia2.thefreedictionary.com/ENIAC, (2019).
2. The Smallest Computer in the World Fits On a Grain of Rice, https://www.popularmechanics.com/technology/a22007431/smallest-computer-world-smaller-than-grain-rice/
3. M. Kadic, G. W. Milton, M. Van Hecke, and M. Wegener, "3D Metamaterials" Nat. Rev. Phys. **1**, 198-210, (2019).
4. R. M. Walser, "Electromagnetic metamaterials", Proc. SPIE, Complex Mediums II: Beyond Linear Isotropic Dielectr. (eds Lakhtakia, A., Weiglhofer, W. S. & Hodgkinson, I. J.) **4467,** (2001).
5. J. Valentine, S. Zhang, T. Zentgraf, E. Ulin-Avila, D. A. Genov, G. Bartal, and X. Zhang, "Three-dimensional optical metamaterial with a negative refractive index," Nature **455**, 376 (2008)
6. N. Yu, et al., "Light propagation with phase discontinuities: Generalized laws of reflection and diffraction", Science **334**, 333-337 (2011).
7. M. Khorasaninejad, et al., "Multispectral chiral imaging with a meta-lens," Nano Lett. **16**, 4595-4600 (2016).
8. M. Khorasaninejad, et al., "Metalenses at visible wavelengths: diffraction-limited focusing and subwavelength resolution imaging," Science **352**, 1190-1194 (2016)
9. W.T Chen, et al "A broadband achromatic metalens for focusing and imaging in the visible," Nat. Nanotechnol. **13**, 220-226 (2018).
10. S. Wang, et al. "A broadband achromatic metalens in the visible," Nat. Nanotechnol. **13**, 227-232 (2018).

11. E. Schonbrun, K. Seo, and K. B. Crozier, "Reconfigurable imaging systems using elliptical nanowires," NanoLett. **11**, 4299-4303 (2011).

12. W. T. Chen, et al., "Integrated plasmonic metasurfaces for spectropolarimetry," Nanotechnology **27**, 224002 (2016).

13. J. P. Balthasar Mueller, K. Leosson, and F. Capasso, "Ultracompact metasurface in-line polarimeter," Optica **3,** 42-47 (2016).

14. A. Pors, M. G. Nielsen, and S. I. Bozhevolnyi, "Plasmonic metagratings for simultaneous determination of Stokes parameters," Optica **2**, 716-723 (2015).

15. W.T. Chen, et al., "Generation of wavelength-independent subwavelength Bessel beams using metasurfaces," Light Sci. Appl. **6**, e16259 (2017).

16. D. Lin, P. Fan, E. Hasman, and M. L. Brongersma, "Dielectric gradient metasurface optical elements," Science **345**, 298-302 (2014).

17. C. Wu, et al., "Versatile polarization generation of perfect optical angular momentum," Nano Lett. **17**, 445-452 (2017).

18. Z. Zhao, et al., "Multispectral optical metasurfaces enabled by achromatic phase transition," Sci. Rep. **5**, 15781 (2015).

19. M. Pu, et al., "Catenary optics for achromatic generation of perfect optical angular momentum," Sci. Adv. **1**, e1500396 (2015).

20. L. Li, et al., "Plasmonic polarization generator in well-routed beaming," Light. Sci. Appl. **4**, e330 (2015).

21. P. C. Wu, et al., "Broadband wide-angle multifunctional polarization converter via liquid-metal-based meta-surface," Adv. Opt. Mater. **5**, 1600938 (2017).

22. W. Ye, et al., “Spin and wavelength multiplexed nonlinear metasurface holography,” Nat. Commun. **7**, 11930(2016).

23. G. Zheng, et al., “Metasurface holograms reaching 80% efficiency,” Nat. Nanotech. **10**, 308-312 (2015).

24. X. Li, et al., “Multicolor 3D meta-holography by broadband plamsonic modulation,” Sci. Adv. **2**, e16021102(2016).

25. L. Huang, et al., “Broadband hybrid holographic multiplexing with geometric metasurfaces,” Adv. Mater. **27**, 6444-6449 (2015).

26. Y. W. Huang, et al., “Aluminum plasmonic multicolor meta-hologram,” Nano Lett. **15**, 3122-3127 (2015).

27. P. C. Wu, N. Papasimakis, and D. P. Tsai, “Self-affine graphene metasurfaces for tunable broadband ab-sorption,” Phy. Rev. Appl. **6**, 044019 (2016).

28. M. C. Sherrott, et al., “Experimental demonstration of >230° phase modulation in gate-tunable graphene-gold reconfigurable mid-infrared metasurfaces,” Nano Lett. **17**, 3027-3034 (2017).

29. K. Thyagarajan, R. Sokhoyan, L. Zornberg, and H. A. Atwater, “Metasurfaces: millivolt modulation of plasmonic metasurface optical response via ionic conductance,” Adv. Mater. **29**, 1701044 (2017).

30. Y. W. Huang, et al., “Gate tunable conducting oxide metasurfaces,” Nano Lett. **16**, 5319-5325 (2016).

31. A. Arbabi, E. Arbabi, Y. Horie, S. M. Kamali, and A. Faraon, “Planar metasurface retroreflector,” Nat. Photon. **11**, 415-420 (2017).

32. R. J. Lin, et al., “Achromatic metalens array for full-colour light-field imaging,” Nat. Nanotechnol. **14**, 227-231(2019).

33. M. Born and E. Wolf, *Principles of Optics* (Pergamon, 1980).

34. D. Jackson, *Classical Electrodynamics,* 3rd ed. (Wiley, 1999).

35. C.L. Holloway, et al., “An overview of the theory and applications of metasurfaces: The two dimensional equivalents of metamaterials” IEEE Antennas Propagat. Mag. **54**, 10-35 (2012).

36. M. A. Kats, R. Blanchard, G. Patrice and F. Capasso, “Nanometre optical coatings based on strong interference effects in highly absorbing media”, Nature Mater. **12**, 20-24 (2013).

37. A. V. Kildishev, A. Boltasseva, and V. M. Shalaev, “Planar photonics with metasurfaces” Science **339**, 1232009 (2013).

38. N. Yu, et al., “Flat optics: Controlling wavefronts with optical antenna metasurfaces” IEEE J. Sel. Top. Quant. Electron. **19**, 4700423 (2013).

39. N. Yu, and F. Capasso, “Flat optics with designer metasurfaces”, Nat. Mater. **13**, 139-150 (2014).

40. F. Aieta, et al., “Aberration-Free Ultrathin Flat Lenses and Axicons at Telecom Wavelengths Based on Plasmonic Metasurfaces”, Nano Lett., **12**, 4932-4936 (2012).

41. A. Arbabi, and A. Faraon, “Fundamental limits of ultrathin metasurfaces”, arXiv preprint arXiv:1411.2537, 2014.

42. B. Adomanis, “Design and optimization of plasmonic 3-D Huygens metasurface building blocks for highly-efficient flat optics”, PhD. Dissertation, Air Force Institute of Technology, (2018).

43. B. Adomanis, D. B. Burckel, and M. A. Marciniak, "3D plasmonic design approach for efficient transmissive Huygens metasurfaces," Opt. Express **27**, 20928-20937, (2019).

44. D. B. Burckel, et al., "Fabrication of 3d metamaterial resonators using self-aligned membrane projection lithography", Adv. Mater., **22**, 3171-3175, (2010).

45. D. B. Burckel, et al., "Micrometer-scale cubic unit cell 3d metamaterial layers", Adv. Mater., **22,** 5053-5057, (2010).

46. D. B. Burckel, et al., "Micrometer-scale fabrication of complex three dimensional lattice basis structures in silicon", Opt. Mat. Express, **5** (10):2231-2239, (2015).

47. K. M. Musick, and D. B. Burckel, "Refinements in membrane projection lithography: a route to fabrication of 3D metamaterials," Proc SPIE 1093005 (2019).

48. F. O. Bartell, E. L. Dereniak, and W.L. Wolfe, "The theory and measurement of bidirectional reflectance distribution function (brdf) and bidirectional transmittance distribution function (btdf)." In Radiation scattering in optical systems, **257**, 154-161. International Society for Optics and Photonics, (1981).

49. B. Balling, "A comparative study of the bidirectional reflectance distribution function of several surfaces as a mid-wave infrared diffuse reflectance standard", M.S. Thesis, Air Force Institute of Technology, (2009).

50. J. C. Vap, "Design and characterization of optical metamaterials using tunable polarimetric scatterometry" M.S. Thesis, Air Force Institute of Technology, (2012).

51. Fiscal Year (FY) 2021 Department of Defense Multidisciplinary Research Program of the University Research Initiative https://www.grants.gov/web/grants/view-opportunity.html?oppId=324779

52. AIR FORCE OFFICE OF SCIENTIFIC RESEARCH BROAD AGENCY ANNOUNCEMENT FA9550-19-S-0003 https://www.grants.gov/web/grants/view-opportunity.html?oppId=314753

53. The finite element method, https://www.comsol.com/multiphysics/finite-element-method, (2019).

54. What is Finite Element Analysis, https://www.simscale.com/docs/content/simwiki/fea/whatisfea.html, (2019).

55. COMSOL Multiphysics, https://www.comsol.com/, (2019).

56. B. Adomanis, et al., "COMSOL Multiphysics® Software as a Metasurfaces Design Tool for Plasmonic-Based Flat Lenses", COMSOL Conference, (2016).

57. P. Genevet, et al., "Recent advances in planar optics: from plasmonic to dielectric metasurfaces", Optica **4**, 139-152 (2017).

58. C. A. Balanis, *Antenna Theory: Analysis and Design*, 3rd Edition. (Wiley-Interscience, 2005)

59. C. Pfeiffer, et al., "Efficient light bending with isotropic metamaterial Huygens' surfaces", Nano Lett., **14**, 2491-2497 (2014).

60. O. Paul, B. Reinhard, B. Krolla, R. Beigang, and M. Rahm, "Gradient index metamaterial based on slot elements," Appl. Phys. Lett., **96**(24):241110, (2010).

61. C. Pfeiffer, and A. Garbic, "Cascaded metasurfaces for complete phase and polarization control," Appl. Phys. Lett., **102**(23):231116, (2013).

62. C. Pfeiffer, and A. Garbic, "Metamaterial Huygens' surfaces: Tailoring wavefronts with reflectionless sheets," Phys. Rev. Lett., **110**:197401, (2013).

63. E. Hecht, *Optics*, 5th Ed. (Pearson, 2016).

64. S. R. Rengarajan, and Y. Rahmat-Samii, “The field equivalence principle: Illustration of the establishment of the non-intuitive null fields”, IEEE Antennas and Propagation Magazine, **42**,122-128, (2000).

65. A. E. H. Love, “The Integration of Equations of Propagation of Electric Waves,” Philos. Trans. R. Soc. London, A, **197**,1-45, (1901).

66. J. A. Stratton, *Electromagnetic Theory*, 1st Ed. (McGraw-Hill, 1941).

67. J. C. Stover, *Optical Scattering: Measurements and Analysis*, SPIE Press; Third edition (2012)

68. F. M. Cady, D. R. Bjork, J. Rifkin and J. C. Stover, “BRDF Error Analysis”, Proc. SPIE 1165, 154 (1990).

69. S. D. Butler, S.E. Nauyoks and M.A. Marciniak, “Experimental analysis of bidirectional reflectance distribution function cross section conversion term in direction cosine space,” Opt. Lett. 40(11), 2445-2448 (2015)

70. J. T. Fong, N. A. Heckert, J. J. Filliben, P. V. Marcal, R. Rainsberger, K. F. Stupic, and S. E. Russek, “MRI Birdcage RF Coil Resonance with Uncertainty and Relative Error Convergence Rates,” Proc. COMSOL, (2017)

REPORT DOCUMENTATION PAGE

Form Approved
OMB No. 0704-0188

1. REPORT DATE *(DD-MM-YYYY)*	**2. REPORT TYPE**	**3. DATES COVERED** *(From - To)*
02-02-2021	PhD Dissertation	04-01-2018 – 03-25-2021

4. TITLE AND SUBTITLE

COMPUTATIONAL ELECTROMAGNETIC MODELING
OF METASURFACE OPTICAL DEVICES WITH DEFECT STUDY

5a. CONTRACT NUMBER

5b. GRANT NUMBER

5c. PROGRAM ELEMENT NUMBER

6. AUTHOR(S)

Diaz, Carlos D., Capt

5d. PROJECT NUMBER

5e. TASK NUMBER

5f. WORK UNIT NUMBER

7. PERFORMING ORGANIZATION NAME(S) AND ADDRESS(ES) AND ADDRESS(ES)

Air Force Institute of
Technology
Graduate School of Engineering
(AFIT/EN)
2950 Hobson Way, Building 640
WPAFB OH 45433-8865

8. PERFORMING ORGANIZATION REPORT NUMBER

AFIT-ENP-DS-21-M-112

9. SPONSORING / MONITORING AGENCY NAME(S) AND ADDRESS(ES)

Augustine M. Urbas
Materials & Manufacturing Dir
Air Force Research Laboratory
WPAFB OH 45433

10. SPONSOR/MONITOR'S ACRONYM(S)

AFRL/RXAN

11. SPONSOR/MONITOR'S REPORT NUMBER(S)

12. DISTRIBUTION / AVAILABILITY STATEMENT

Distribution Statement A. Approved for Public Release; Distribution Unlimited

13. SUPPLEMENTARY NOTES

14. ABSTRACT

One of the first fabricated metasurface optical devices, the in-plane V-antenna lenses, were plagued by a fundamental transmission limit (<25%). Two distinct sets of Out-of-Plane phase elements were designed with improved transmission (~60%). These were fabricated as beamsteerers and characterized in terms of their Bidirectional Transmittance Distribution Function measured as a function of scatter angle. Experimental data from the beamsteerers was analyzed via simulations using a finite element method (FEM). The measurements showed the designed beamsteering, but also a strong zero-order diffraction not present in the simulations, which motivated this study to understand what was causing these differences. To that end, FEM models which addressed specific defects and models that adjusted the coupling of the device were developed and these well-predicted the measured data. These models provided an understanding of the near-field effects that caused this behavior, and provided strong evidence that the amplitude and phase imparted by the fabricated phase elements must be different than what was designed, either because their placement is different than what was designed or their design was slightly changed during fabrication. Future work will focus on studying the impact of coupling and leveraging the lessons learned into future OOP design-fabrication-test iterations.

15. SUBJECT TERMS

Metasurface, Plasmonic, Finite element modeling, Membrane Projection Lithography, Scatterometry

16. SECURITY CLASSIFICATION OF:			**17. LIMITATION OF ABSTRACT**	**18. NUMBER OF PAGES**	**19a. NAME OF RESPONSIBLE PERSON**
a. REPORT	**b. ABSTRACT**	**c. THIS PAGE**			Dr. Michael A. Marciniak, AFIT/ENP
U	U	U	UU	148	**19b. TELEPHONE NUMBER** *(include area code)* (937) 255-3636 x4529 michael.marciniak@afit.edu

Standard Form 298 (Rev. 8-98)
Prescribed by ANSI Std. Z39.18